E-25-686

GEORGIA INSTITUTE OF TECHNOLOGY
School of Mechanical Engineering
Atlanta, Georgia

PROPAGATION OF NOISE IN THE FAR FIELD FROM ELECTRIC TRANSFORMERS

FINAL REPORT

P. O. No. 086-554648-000
General Electric Company

W. James Hadden, Jr.
Assistant Professor

Pranab Saha
Graduate Research Assistant

August, 1979

GEORGIA INSTITUTE OF TECHNOLOGY
School of Mechanical Engineering
Atlanta, Georgia

PROPAGATION OF NOISE IN THE FAR FIELD FROM ELECTRIC TRANSFORMERS

FINAL REPORT

P. O. No. 086-554648-000
General Electric Company

W. James Hadden, Jr.
Assistant Professor

Pranab Saha
Graduate Research Assistant

August, 1979

FOREWORD

The following Ph.D. thesis, "Propagation of Sound in the Far Field from Electric Transformers," by Pranab Saha, and the computer program listing attached thereto comprise the Final Report for Georgia Tech Contract No. E25-686. Dr. Saha's thesis discusses in detail the work done at Georgia Tech on this contract.

TABLE OF CONTENTS

LIST OF TABLES

LIST OF ILLUSTRATIONS

Figure Page

LIST OF SYMBOLS

Roman Symbols

$\bar{a}_n$	surface normal acceleration, m/sec^2
A_D	diffraction integral as given by equation (3-26)
c	ambient speed of sound, m/sec
C	path of integration as given by equation (3.3)
D	diffraction coefficient
E_R	relative error as given by equation (7.9)
f	function as given by equation (3.3)
f(X)	auxiliary fresnel function
F	spatial spreading representation of diffracted energy, equation (2.15)
g(X)	auxiliary fresnel function
g_1, g_2, g	functions as given by equations (3.8) and (3.9)
G	Green's function, m^{-1}
G_f	free space Green's function, m^{-1}
h	function as given by equation (3.10)
H	transformer height, m
i	square root of -1
k	wave number, m^{-1}
k_1, k_2, k_3, k_4, k_5	parameters as given by equation (7.1)
ℓ_1, ℓ_2	distances of the centers of curvature of wavefronts as in Fig. 2-4
L	distance of the listener from the source around the diffracting edge, m

L_p	sound pressure level, dB
m	integer as given by equation (3.5)
M_j	number of terms present in Green's function
$M_\nu(\theta)$	function as given by equation (3.28)
$\bar{n}$	unit normal pointing out of the vibrating surface
p	complex amplitude of acoustic pressure, Pa
P, P_1, P_2	r.m.s. value of acoustic pressure, Pa
r	shortest distance of the listener from the diffracting edge, m
r_o	shortest distance of the source from the diffracting edge, m
$\bar{r}$	listener position vector, m
$\bar{r}_o$	source position vector, m
r, θ, z	cylindrical coordinate system
R	direct path from the source to the listener, m
R_c	distance of the listener from the center of the tank or any surface, m
R_p	pressure amplitude reflection coefficient
S_o	surface area of the vibrating structure, m^2
t	variable as given by equation (3.31a)
T	variable as given by equation (3.23a)
u	variable as given by equation (3.24a)
$\bar{v}_n$	surface normal velocity, m/sec
w	width of the surface as shown in Fig. 3-5
W	projected width of the transformer viewed by the listener, m

x,y,z	Cartesian coordinate system
X	argument of the auxiliary Fresnel function
Y	argument of the auxiliary Fresnel function, equation 3.35
z	listener height, m
z_o	source height, m
Z_1	characteristic impedance of air
Z_2	specific impedance of the ground surface

Greek Symbols

α	variable defined by equation (3.5)
β	exterior angle of wedge, rad
γ	variable defined by equations (3.37a) and (3.37b)
$\alpha_1, \beta_1, \gamma_1$	variables defined by equation (7.3)
Γ	a dimensionless quantity defined by equation (3.29a)
δ	dirac-delta function, equation (3.1)
ζ	complex ζ plane
λ	wavelength, m
μ	parameter defined by equation (7.4)
ν	wedge index defined by equation (3.29b)
ξ	distance defined by Fig. 7-4, m
ρ_o	ambient density, kg/m^3
ϕ	phase representation of the acoustic pressure field
ω	angular frequency, rad/sec
θ	angle between the side of the wedge closer to the listener with the plane passing through the listener and the diffracting edge, rad

θ_o	angle between the side of the wedge closer to the listener with the plane passing through the source and the diffracting edge, rad
x_1, x_2	location of the wavefronts as in Fig. 2-4

Subscripts

a	actual source
D	double-edge diffraction
dir	direct wave
diffr	diffracted wave
ff	far field
i	image source
inc	incident wave
j, ℓ	components of summation indices
NEMA	National Electrical Manufacturers Association standard
ref	constant reference value
L	listener
S	source

Mathematical Symbols

<	less than
>	greater than
Σ	summation
+	$\theta + \theta_o$
-	$\theta - \theta_o$
| |	absolute value
< >	root mean square

SUMMARY

A theory is described for predicting the far-field sound radiation patterns of rectangularly shaped electric transformers for given surface vibrations. The acoustic pressure outside the transformer is expressed in terms of an integral over vibrational normal velocity along the surface with a kernel. This kernel is an approximation to the Green's function for a point source just outside the surface of a rigid body with the same shape as the transformer. The Green's function is found to be expressible using concepts and techniques related to the geometrical theory of diffraction. The resulting Green's function takes into account direct waves, reflected waves, and diffracted waves which are derived from uniformly valid asymptotic expressions for diffraction of point source generated waves by a semi-infinite right-angled rigid wedge. The agreement of the theoretically calculated sound pressure level in the far field with those measured values gives a substantial verification of the applicability of the geometrical theory of diffraction to the experimental example of a 1.3 m x 0.76 m x 1.52 m water-filled steel tank excited at 265 Hz by two underwater speakers within the tank. The numerical results are also compared with the results of other analytical and experimental

investigations. Finally, some recommendations are given as possible extensions of the present work for better prediction of transformer noise.

CHAPTER I

INTRODUCTION

Community exposure to acoustic noise generated from transformers [1,2] operating on substations (Fig. 1-1) or power plants is a complex and long standing problem. The noise which in general increases with the size of the transformer structure is characterized by a continuous low frequency hum of 120 Hz and its multiples. Transformer noise originates mainly due to the vibration of magnetic core and core laminations caused by magnetostriction [3]. Electromagnetic forces arising due to alternating flux in the magnetic core give rise to magnetostriction of the core material. This in turn produces a rhythmic change in length of the core plate with the alternating polarities of the flux wave and hence vibration of the core material and the core laminations and joints. The core vibration is transmitted to the tank surface through the oil in which the core is immersed and by direct transmission at points where the core is attached to the tank. The tank surface radiates this vibrational energy outside the transformer as sound energy and hence as noise. As a transformer tank is only partially filled with oil, the top of the tank is not in contact with oil and hence the sound radiated from the top is negligible

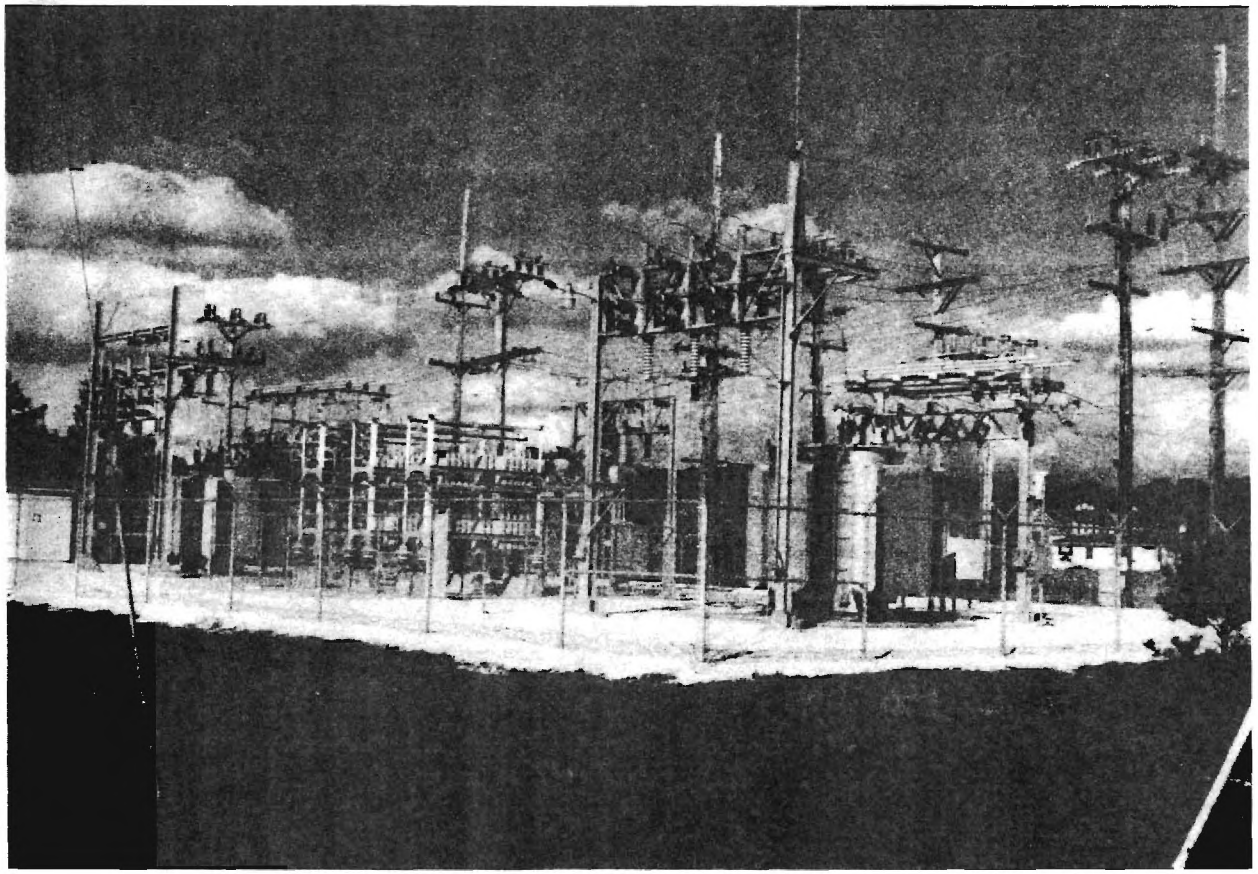

Figure 1-1. Photograph of a Typical Transformer Substation

compared to the other surfaces.

Different types of noise abatement options, starting from noise reduction at the source to the reduction of noise at the listener position, are available in the literature (e.g., references [4-9]). Noise reduction at the source may be obtained with the proper design of the system in order to minimize the vibrational amplitude of the magnetic core [4]. Other methods of noise reduction may be accomplished by constructing barriers [5], or, partial or total sound attenuating enclosures (Fig. 1-2) [8,9] around the transformer. Further progress in controlling the noise level radiated from a transformer without excessive economic penalties requires an increasingly sophisticated understanding of not only the generation of noise and various engineering control methods, but also the propagation of noise from the transformer site to the surrounding areas.

In the ideal case, the manufacturer and the purchaser of a transformer installation would like to certify prior to installation either some statistical limits, or, preferably some upper limits of sound levels at some given far-field location (e.g., a property line). This is not a trivial task mainly because of different transformer designs and of appreciable variation of noise generation characteristics even among transformers of seemingly identical design. Manufacturers do routinely test transformers for noise generation characteristics according to the National Electrical

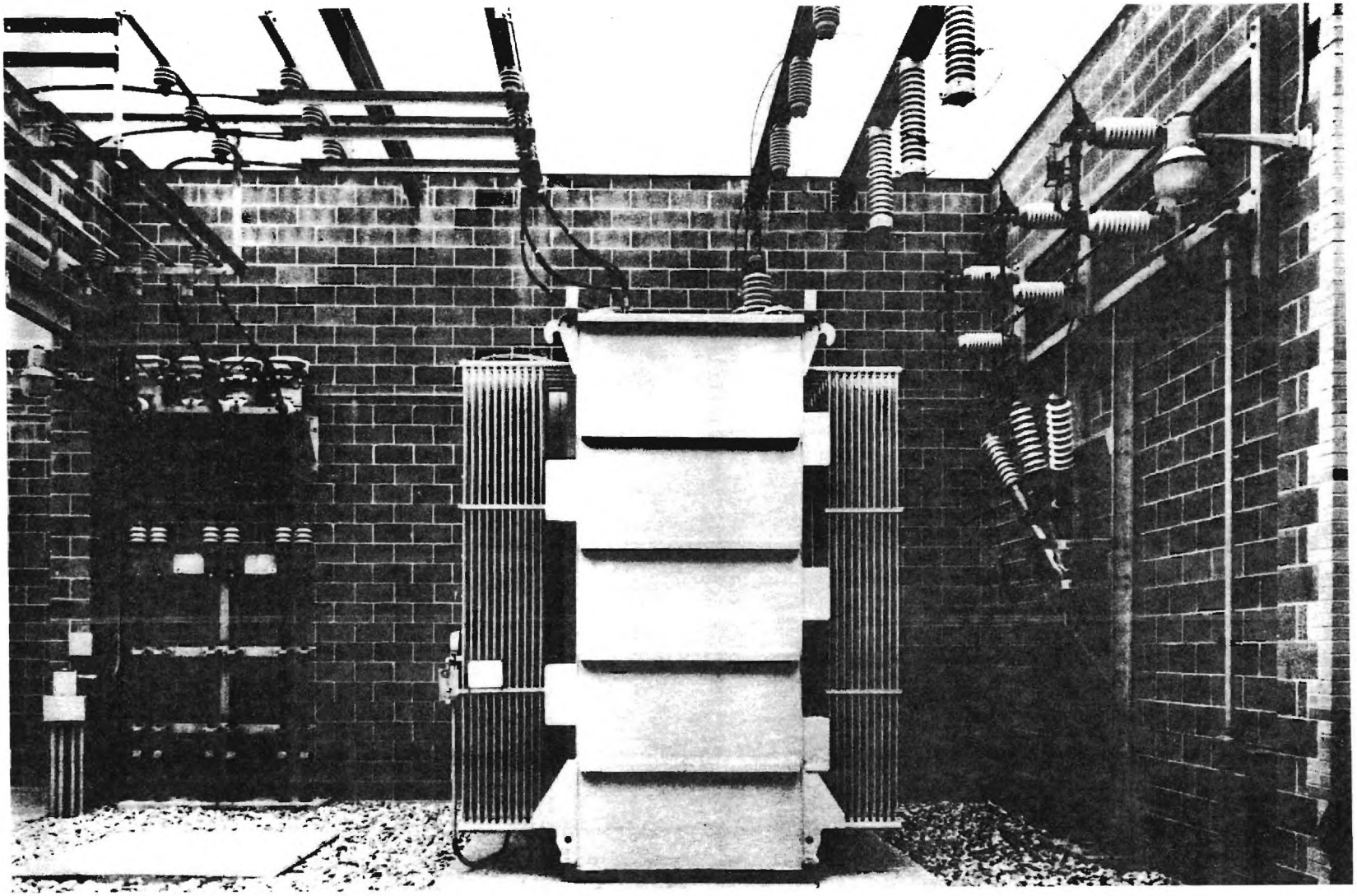

Figure 1-2. Photograph of a Partial Enclosure Around a Typical Transformer for Transformer Noise Abatement

Manufacturers Association (NEMA) Standard [10]. This is a near field test at one foot away from the transformer surface and there is no generally accepted method for extrapolating far-field directional noise predictions from the NEMA test data.

One of the techniques which is frequently used by many power industries to estimate the far-field sound level at the property boundary or near a potential complaint's location is based on Schulz and Ringlee's [11] scale model of the NEMA test data given by

$$L_p)_{ff} = L_p)_{NEMA} - 4.4 - 20 \log [R_c/(WH)^{1/2}]. \quad (1.1)$$

Here $L_p)_{NEMA}$ is the sound level measured in the NEMA test, $L_p)_{ff}$ is the sound level at a large distance R_c from the geometric center of the tank, W is the projected width of the transformer viewed by the listener and H is the transformer height.

Another method (also based on the measured test data at NEMA locations) that has recently been developed by Vér, Andersen and Myles [12] to predict the sound radiation of a transformer at a distance R_c from the transformer tank is based on the equation

$$L_p)_{ff} = L_p)_{NEMA} - 20 \log_{10} (R_c/\sqrt{S_o}) - 8. \quad (1.2)$$

Here S_o represents the surface area of the four sides of the transformer tank.

It is to be noted that both equations (1.1) and (1.2) give the standard 6 dB drop in level (valid in the far field in the absence of reflection and absorption) for every doubling of distance R_c. This would seem about as well as one might do for an estimate in the absence of any detailed information on the near field, on the transformer geometry, or, on site characteristics (presence of barriers, trees, humps, buildings, etc.). Although equation (1.2) agrees within one or 2 dB with equation (1.1) [13], none of these equations obviously can be wholly right as they do not give any directional variation and in that they use only one number $[(L_p)_{NEMA}]$ to characterize the near field and only one number $(S)^{1/2}$ or $(WH)^{1/2}$ to characterize the tank geometry.

The directional asymmetry of transformer far-field noise radiation has been demonstrated by experimental results taken at two apparently similar substation sites and reported by R. A. Bell [14] of Commonwealth Edison. The data also indicates substantial departures from the 6 dB per doubling of distance law even at distances as large as 152 m (500 ft). This data raises some questions and is difficult to interpret but does nevertheless demonstrate that the propagation of noise from a transformer is poorly modeled as propagation from an omnidirectional coherent source.

A detailed prediction of sound radiation in the far field may be obtained from a knowledge of surface vibration of the transformer tank. Possible methods to predict the sound radiation from a typical vibrating surface (Fig. 1-3) (e.g., an electric transformer), widely cited in the literature [15-20], are based on the Helmholtz-Kirchhoff integral representation

$$p(\bar{r}) = \frac{1}{4\pi} \iint_{S_o} \left[p(\bar{r}_o) \frac{\partial G_f}{\partial n} (\bar{r},\bar{r}_o) - G_f(\bar{r},\bar{r}_o) \frac{\partial p(\bar{r}_o)}{\partial n} \right] dS_o. \quad (1.3)$$

Equation (1.3) expresses the pressure $p(\bar{r})$ at any point Q outside the vibrating surface in terms of the pressure $p(\bar{r}_o)$ and its outward normal gradient $\frac{\partial p(\bar{r}_o)}{\partial n}$ on the vibrating surface S_o where $\bar{n}$ is the unit normal pointing out of the vibrating surface. The factor $G_f(\bar{r},\bar{r}_o)$ is the free space Green's function,

$$G_f(\bar{r},\bar{r}_o) = \frac{e^{ik|\bar{r} - \bar{r}_o|}}{|\bar{r} - \bar{r}_o|}, \quad (1.4)$$

which describes the disturbance at $\bar{r}$ due to a unit source P at $\bar{r}_o$.

This formulation allows one to obtain the acoustic pressure outside the vibrating surface provided the surface vibration distribution is known. However, it has been shown

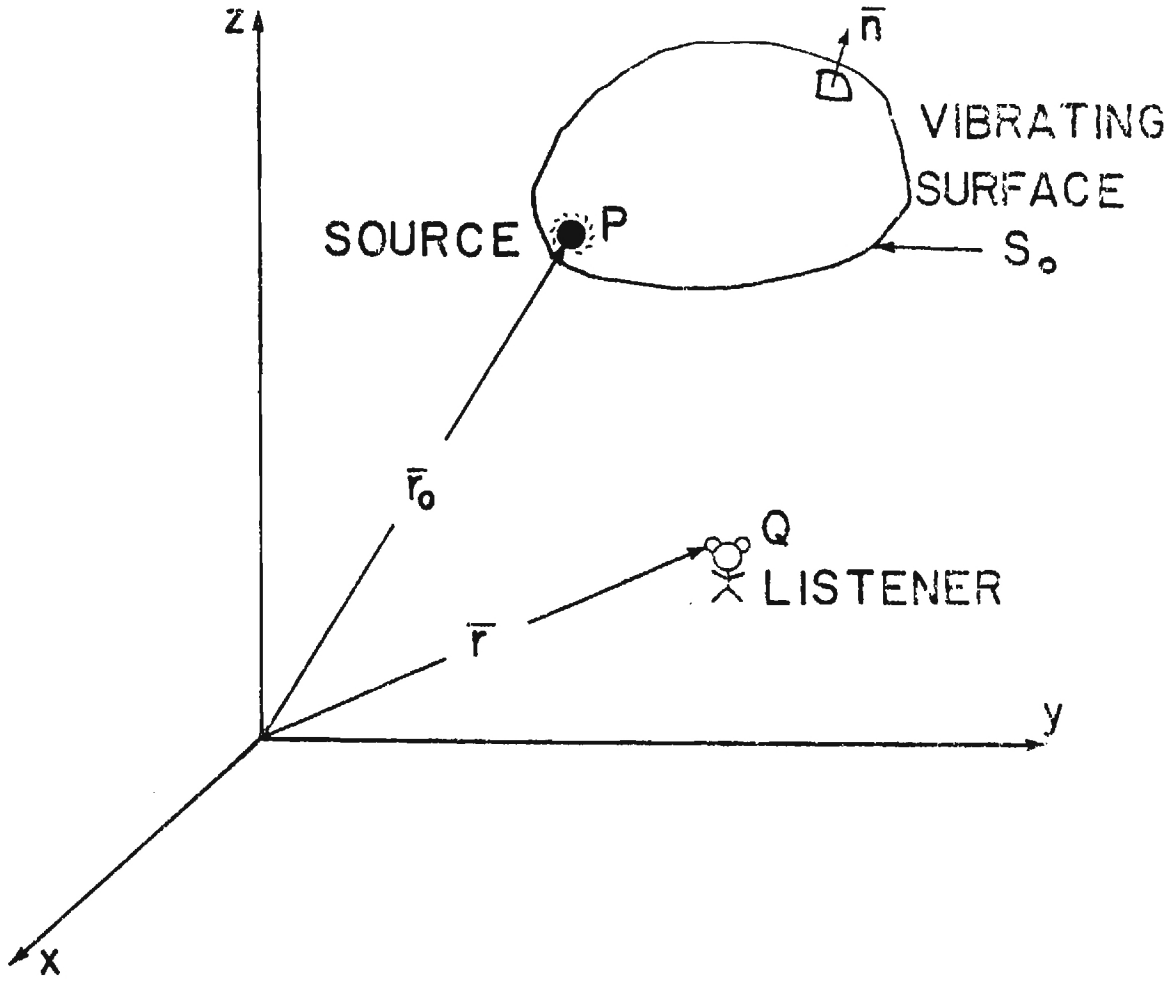

Figure 1-3. Definition of Symbols Used in the Discussion of Sound Radiation from an Ambient Vibrating Surface S_o. Here x,y,z Represent the Cartesian System and $\bar{n}$ is the unit Normal Pointing Out of S_o

in the literature [20-23] that the use of equation (1.3) as a basis to obtain an integral equation for this surface distribution presents some analytical difficulties when the vibrational frequencies correspond to certain interior resonance frequencies of the vibrating surface. An attempt to alleviate this difficulty has been proposed by Schenck [19]. He proposed to supplement the integral formulation (equation (1.3)) by an overdetermined system of linear equations (based on the surface and the interior Helmholtz integral formulation) where one specifies the surface acceleration to compute the surface pressure. The difficulty with this problem is to determine the optimum number of the interior points and their locations to generate the extra relations which are needed in this method. More recently, Jones [23] has suggested a procedure to eliminate this difficulty over a specified frequency range.

The use of finite element methods for the numerical solution of the integral equation formulation is restricted to the limitation of the element mesh size. The number of elements required to approximate the vibrating surface depends heavily on the frequency range of interest. At higher frequencies the size of the elements must be small compared to an acoustic wavelength. The number of finite elements thus needed to solve the simultaneous algebraic equations that result from the finite element approximations to the integral equation become prohibitively large even for seemingly

uncomplicated radiation problems. This presents practical limitations on the applicability of the method mainly because of the large computing time needed to solve the simultaneous algebric equations and the memory capacity of the digital computer.

The intent of this dissertation is to develop an adequate approximation to the Green's function which appears in the integral equation for the pressure outside the surface (see Chapter II) and to apply this analysis to the prediction of the far-field radiation pattern for a typical transformer on a flat ground plane. The Green's function is approximated using techniques related to Keller's geometrical theory of diffraction [24,25] under the condition that the gradient of the Green's function vanishes on the transformer surface and with the assumption that the ground is a rigid plane. Thus, if the surface normal velocity or the surface normal acceleration is known *a priori*, one just computes an algebric summation to find the acoustic pressure outside the transformer and thence the sound pressure level. In this approach, one neither solves any system of linear equations, nor envisions any severe limitations regarding the capacity of digital computer.

In Chapter II, a method based on the Helmholtz-Kirchhoff integral solution is described in brief for the computation of sound radiation from electric transformers resting on ground. Outlines of various theoretical and

mathematical considerations on which the analysis is based are described here. A short description of the geometrical theory of diffraction is also given here.

Chapter III gives a detailed derivation of the contour integral solution for the diffraction of a point source by a wedge of arbitrary angle. This is further carried out to the extent of deriving approximate expressions for the Green's function for single-edge diffraction of a point source by a right-angled rigid wedge. Immediately following this, an outline for the development of the double-edge diffraction is presented.

A detailed description of the development of a computer oriented numerical scheme for predicting transformer noise levels in the far field from given surface acceleration data is provided in Chapter IV. Chapter V discusses the experimental application of the numerical method for the sound prediction. A summary of the nature of different experiments performed and other available experimental applications are described here. The experimental results are compared with the developed and other available theoretical analysis in Chapter VI.

Chapter VII discusses on the transformer noise prediction schemes and the justification of the applicability of the present method. Several prediction schemes, their limitations and various critical analyses that have been made to obtain the present method are discussed in detail. The

effect of finite impedance of ground and double-edge diffraction which are discussed in this chapter enables one to obtain some quantitative insight of sound radiation from a rectangularly box-like vibrating structure.

CHAPTER II

METHOD OF SOLUTION

Mathematical Formulation

The fundamental physical basis of acoustic wave propagation which are based on the equations of fluid mechanics include a mass conservation equation, a momentum equation and a conservation of energy equation. For an ideal fluid, these may be expressed in the familiar form as

$$\frac{\partial \rho'}{\partial t} + \rho_o \nabla \cdot \bar{v}' = 0 \tag{2.1}$$

$$\rho_o \frac{\partial \bar{v}'}{\partial t} = -\nabla p' \tag{2.2}$$

and

$$\frac{\partial p'}{\partial t} = c^2 \frac{\partial \rho'}{\partial t} \tag{2.3}$$

Here p', ρ' and $\bar{v}'$ represent the acoustic contributions to the overall pressure, density and velocity fields respectively, ρ_o is the ambient density of the fluid, c is the speed of sound in air and t represents the time dependence.

With some modest manipulation of the above equations and with the assumption that the acoustic pressure varies harmonically with time, the acoustic wave equation can be

written in the well-known form of the scalar Helmholtz equation

$$\nabla^2 p + k^2 p = 0 \ . \tag{2.4}$$

Here the time dependent factor, $\exp(-i\omega t)$, is omitted and will be suppressed throughout the dissertation. The term ω is the angular frequency and i represents the square root of -1. The term p in equation (2.4) is the complex amplitude of acoustic pressure and k, the wave number ω/c, is defined as the ratio of the angular frequency ω to the speed of sound c.

The pressure field due to any vibrating surface, e.g., an electric transformer (Fig. 1-3), must satisfy the scalar Helmholtz equation subject to appropriate boundary conditions on the vibrating surface and at infinity. The surface boundary condition which expresses the equilibrium relationship of the vibrating structure given by

$$\frac{\partial p}{\partial n} = ik\rho_o c v_n \tag{2.5}$$

is actually another form of Euler equation. Equation (2.5) relates the outward normal gradient of pressure $\frac{\partial p}{\partial n}$ with the outward normal velocity component v_n. The boundary condition at infinity, known as the Sommerfeld radiation condition [26], is given by

$$\lim_{r\to\infty} r\left(\frac{\partial p}{\partial r} - ikp\right) = 0 \qquad (2.6)$$

where r is the distance from the origin.

The classical integral representation of the above boundary-value problem, discussed in detail by Baker and Copson [26], is known as the Helmholtz-Kirchhoff integral. This expresses the complex amplitude of the acoustic pressure outside any vibrating surface (Fig. 1-3) as

$$p(\bar{r}) = \frac{1}{4\pi} \iint_{S_o} \left[p(\bar{r}_o) \frac{\partial G_f(\bar{r},\bar{r}_o)}{\partial n} - ik\rho_o c v_n(\bar{r}_o) G_f(\bar{r},\bar{r}_o) \right] dS_o \qquad (2.7)$$

where S_o is the surface area of the vibrating surface, $p(\bar{r}_o)$ is the surface pressure and $G_f(\bar{r},\bar{r}_o)$ is the Green's function which describes the disturbance at $\bar{r}$ due to a unit source at $\bar{r}_o$. Equation (2.7) is an integral representation of the pressure which satisfies equations (2.4) through (2.6) and is valid for any $\bar{r}$ strictly outside S_o.

Theoretical Considerations

Transformers which operate at sub-stations close to residential areas and are large enough to constitute a noise nuisance can be considered as smooth rigid rectangular box-like structures. As a good first idealization, the ground on which the transformer rests is considered as a rigid (perfectly reflecting) plane of infinite extent (Fig. 2-1). Since the assumption of a rigid ground in acoustics is

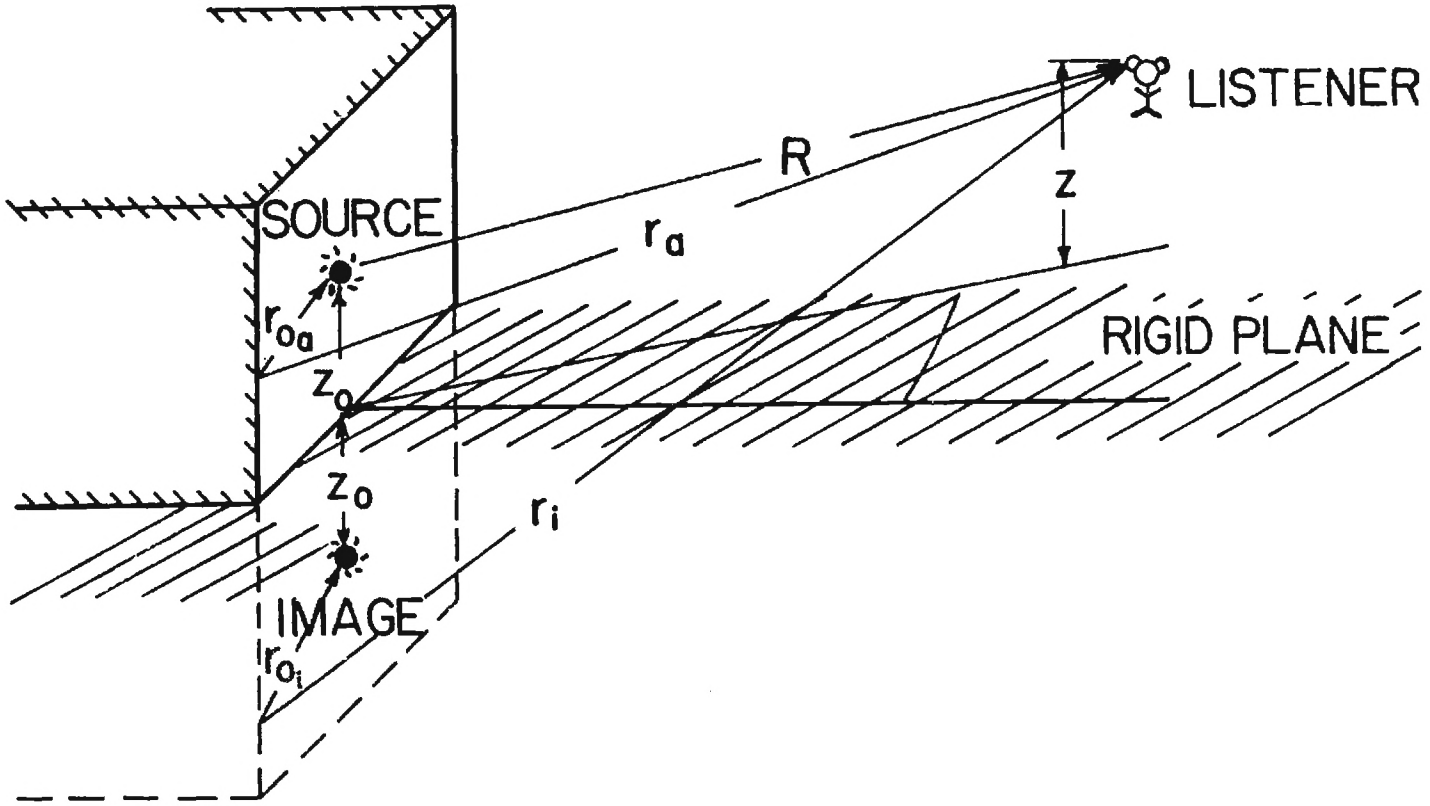

Figure 2-1. Sketch Illustrating the Idealization of the Ground as a Perfectly Rigid Plane

analogous to the use of a perfectly reflecting surface in optics, it is appropriate to employ the method of images to deal with reflections from the ground. The concept applied to the method of images is that the original problem of source plus wall is replaced by one where there are only two sources (original source and image source) but no wall. The consideration of the image source to be a mirror image of the original source in all respects requires that the normal component of fluid velocity at the ground vanishes identically. This property is the same as the boundary condition that would be imposed by the presence of the wall in the original boundary-value problem with original source and wall.

The effect of reflections from the ground may be included by considering separate Green's functions $G(\bar{r},\bar{r}_o)$ for the original source as well as for the image source embedded on the surface of the mirror image of the transformer, or, by employing Green's function which adds for each source point above the ground a similar contribution from a fictitious source the same distance below the ground plane [27]. Using such Green's functions in equation (2.7) with the additional condition that the gradients of the Green's functions vanish on the box surface [28], equation (2.7) can be eventually written as

$$p(\bar{r}) = \frac{\rho_o}{4\pi}\left[\iint_{S_{o_a}} G(\bar{r}_a,\bar{r}_{o_a})a_n(\bar{r}_{o_a})dS_a + \iint_{S_{o_i}} G(\bar{r}_i,\bar{r}_{o_i})a_n(\bar{r}_{o_i})dS_i\right] \tag{2.8}$$

or, more conveniently,

$$p(\bar{r}) = \frac{\rho_o}{4\pi} \iint_{S_o} G(\bar{r},\bar{r}_o) a_n(\bar{r}_o) dS_o. \qquad (2.9)$$

Here the surface S_{o_a} and S_{o_i} in equation (2.8) is taken as the surfaces of the actual and the image transformer, respectively. The terms $\bar{r}_a$, $\bar{r}_{o_a}$, $\bar{r}_i$, $\bar{r}_{o_i}$, which are needed in computing the distances from the original source and the image source to the listener, are defined in Fig. 2-1. The factor a_n, the normal surface acceleration, is given by

$$a_n = -i\omega v_n \qquad (2.10)$$

and S_o in equation (2.9) may be considered as the surface of the vibrating surfaces of the box and its mirror image. Unless otherwise mentioned, this definition of S_o will be carried on for the rest of the dissertation. The Green's function in equation (2.9) which will be used throughout the dissertation will be fabricated within the spirits of Keller's geometrical theory of diffraction and will contain informations like reflection from the ground as well as diffraction around the sides of the tank surface. Thus the overall field of a vibrating transformer, resting on the ground, is considered as the linear superposition of radiation fields from point sources continuously distributed over a rigid

surface, suspended in unbounded space, with twice the height of the transformer. It is to be noted here that the assumption of a perfectly rigid ground may often lead to a conservative estimate of the sound pressure level because of the overestimate of the pressure field at points of constructive interference between direct and ground-reflected waves.

Geometrical Theory of Diffraction

The theory of geometrical acoustics is based on the assumption that acoustic wave travels along certain curves called rays. This theory fails to explain the experimental observation that acoustic energy incident on an opaque obstacle enters the region where there are no rays, i.e., the shadow. Since wave cannot travel through the obstacle (as there are no refracted rays in this case), this energy must come from waves travelling around the obstacle into the shadow region. Such phenomena of energy transference which give rise to discrepancies between the experimental observation and the theory of geometrical acoustics are known as diffraction effects.

Diffracted rays are produced whenever an acoustic wave hits an edge, a corner or a vertex of a boundary surface, or is tangent to such a surface. Diffraction is caused by the mutual interference of the secondary waves emitted by those parts of the original wavefront which are not obstructed by the diffraction surface. The theory of diffraction

describes the wave propagation of an obstacle from the illuminated region to the shadow region without passing through the obstacle.

Geometrical theory of diffraction, like geometrical acoustics, assumes that acoustic energy propagates along rays. The diffracted wavefronts can be defined by Huygens wavelet construction and by an eikonal or phase function which is constant on the wavefront and satisfies the usual eikonal equation. The direction of travel of these rays are governed by several laws of diffraction analogous to the laws of reflection and the laws of refraction. If the incident ray and each of the diffracted rays are in the same medium, they make equal angles but lie on opposite sides of the plane normal to the boundary surface at the point of diffraction (Fig. 2-2). An incident ray striking the edge of a wedge obliquely, produces a cone of diffracted rays, as shown in Fig. 2-2. The vertex of this cone is the point of incidence on the edge. If the ray is normally incident on the edge of the wedge, a plane of diffracted rays is produced (Fig. 2-3). For the incident and the diffracted rays in different media, the ratio of sines of the angles between each of them and the normal plane is reciprocal to the ratio of the indices of refraction of each of the medium.

An acoustic pressure field $p(\bar{r})$ associated with each ray in the geometrical theory of diffraction [29,30] is given by

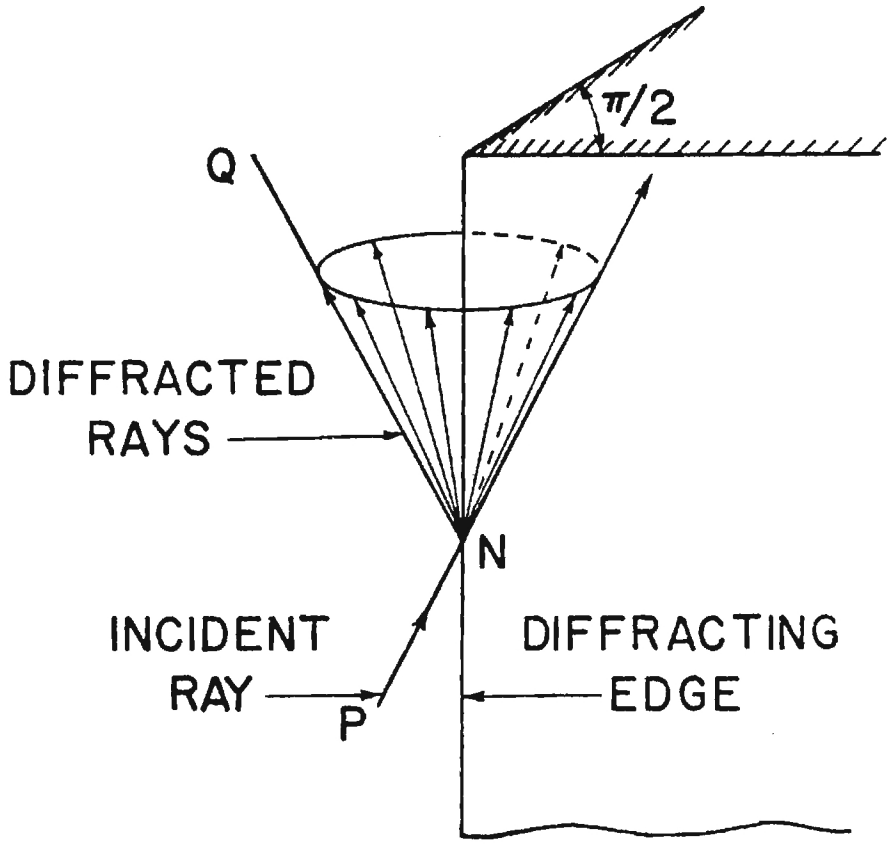

Figure 2-2. A Cone of Diffracted Rays Produced by an Incident Ray Hitting the Edge of a Right-Angled Wedge Obliquely

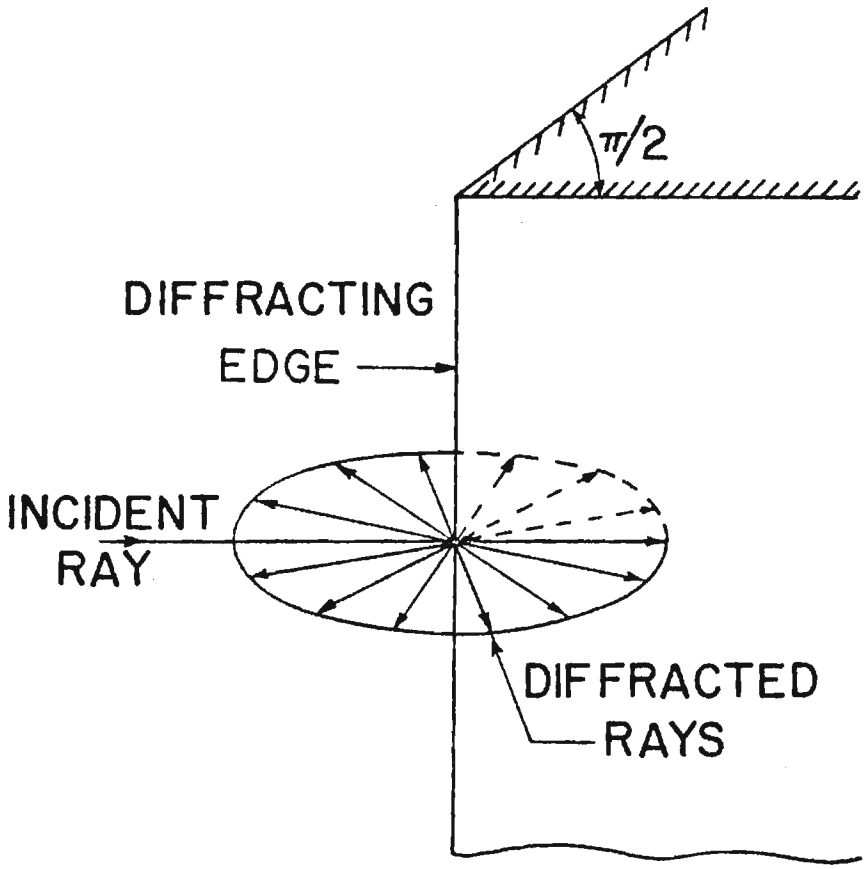

Figure 2-3. A Plane of Diffracted Rays Produced by an Incident Ray Hitting the Edge of a Right-Angled Wedge Normally

$$p(\bar{r}) = P(\bar{r})e^{ik\phi(\bar{r})} \tag{2.11}$$

Here $P(\bar{r})$ is the pressure amplitude at a distance r along the ray and $\phi(\bar{r})$ is the phase of the pressure field at r. An expression for the variation of the pressure wave amplitude $P(\bar{r})$ along the ray paths can be developed from the conservation of energy flux in a narrow tube of rays. Figure 2-4 shows such a tube of rays where the rays are passing from x_1 to x_2. The two wavefronts x_1 and x_2 at the two ends of the ray tube are normal to the rays and at a distance r apart. The centers of curvature of these two wavefronts are at distances ℓ_1 and ℓ_2 from the wavefront x_1 and ℓ_1+r and ℓ_2+r from the wavefront x_2. If $P_1(\bar{r})$ is the pressure amplitude at x_1, the intensity of the pressure field at x_1 is proportional to P_1^2 and the energy flux is given by $P_1^2 ds_1$ where ds_1 is the cross-sectional area of the wavefront x_1. If the pressure amplitude at x_2 is $P_2(\bar{r})$ and the corresponding cross-sectional area is ds_2, the energy flux is given by $P_2^2 ds_2$. The conservation of energy flux along the ray tube then gives

$$P_1^2 ds_1 = P_2^2 ds_2 \tag{2.12}$$

where

$$ds_1 = \ell_1 d\theta_1 \ell_2 d\theta_2 \tag{2.13}$$

$$ds_2 = (\ell_1+r)d\theta_1(\ell_2+r)d\theta_2. \tag{2.14}$$

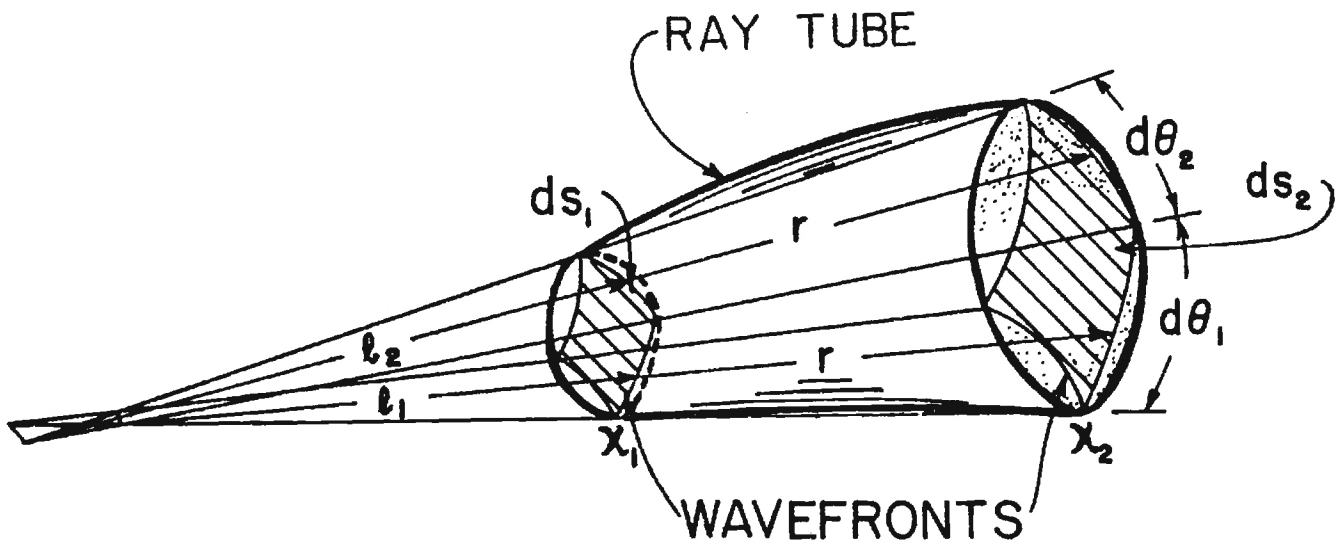

Figure 2-4. Sketch of a Tube of Rays and Two Small Portions of Wavefronts Normal to Them

From equations (2.13) and (2.14), the ratio of the areas of the wavefront sections is

$$\frac{ds_2}{ds_1} = \frac{\ell_1 \ell_2}{(\ell_1+r)(\ell_2+r)}. \tag{2.15}$$

If the tube of rays is shrunk up to the limit of $\frac{ds_2}{ds_1}$ where it contains only one ray, the above equations (equations (2.12) through (2.15)) relate the amplitudes P_1 and P_2. Substituting equation (2.15) in equation (2.12), one obtains

$$P_2 = P_1 \left[\frac{\ell_1 \ell_2}{(\ell_1+r)(\ell_2+r)} \right]^{1/2}. \tag{2.16}$$

Thus, the pressure amplitude P_2 of the wavefront at x_2 can be computed provided the amplitude P_1 of the wavefront at x_1 is known.

The phase of the field on a ray is assumed to be proportional to the acoustical length of the ray from some known reference point [29] for which the phase is known. This yields

$$\phi_2 = \phi_1 + r \tag{2.17}$$

where ϕ_1 is the phase at x_1 from where r is measured and ϕ_2 is the phase at x_2. From equations (2.11), (2.16) and (2.17), one obtains the acoustic pressure field on a ray

given by

$$p(\bar{r}) = P_1 \left[\frac{\ell_1 \ell_2}{(\ell_1+r)(\ell_2+r)} \right]^{1/2} e^{ik(\phi_1+r)} . \qquad (2.18)$$

The acoustic pressure field at any point Q due to a ray diffracted at N (Fig. 2-2) is obtained by multiplying the incident pressure field at N by a diffraction coefficient D(N). This is given by

$$P_{diffr}(Q) = P_{inc}(N) D(N) F e^{ikr} \qquad (2.19)$$

where $P_{inc}(N)$ is the energy associated with the ray incident on the edge at N. The diffraction coefficient D(N) depends on the angles of incidence and diffraction, the wavelength λ and the geometrical and physical properties of the medium in the immediate vicinity of the point of diffraction. The diffraction coefficient describes the distribution of the acoustic energy among the diffracted rays. The spatial spreading of energy after diffraction is given by F which depends on the types of diffracting surfaces. The term e^{ikr} represents the spatial phase shift of the diffracted rays. According to this theory, diffraction is completely a local phenomenon and the diffracted rays, away from the points of diffraction, behave just like ordinary rays. Once the diffraction coefficient is known, these rays may be treated according to the theory of classical geometrical acoustics.

CHAPTER III

DERIVATION OF WEDGE DIFFRACTION EXPRESSION

Derivation of Contour Integral Solution for Wedge Diffraction

The impetus for the present chapter comes from the problem of deriving the wedge diffraction expression where a wave is diffracted by a rigid wedge due to the presence of a unit strength point source near the wedge. An exact solution for a particular class of two-dimensional wave diffraction problem was originally given by Sommerfeld [31], although the problem for the case of a point source and a rigid wedge of arbitrary angle was first solved by MacDonald [32] and later a brief derivation was given by Bromwich [33]. Recently, a complete derivation of the contour integral solution for diffraction of a point source generated wave by a rigid wedge has been given by Pierce [34].

A cylindrical coordinate system (r,θ,z) where $x=r\cos\theta$, $y=r\sin\theta$ (Fig. 3-1) with the z-axis lying along the edge of the wedge is chosen to describe the geometrical configuration of the wedge diffraction problem. The two faces of the wedge are taken as the $\theta=0$ and $\theta=\beta$ planes where β is the exterior angle (with $\beta>\pi$) of the wedge. It is to be noted that $\beta=3\pi/2$ represents a right-angled wedge. A single harmonic point source is located at a point (r_o,θ_o,z_o) such that the

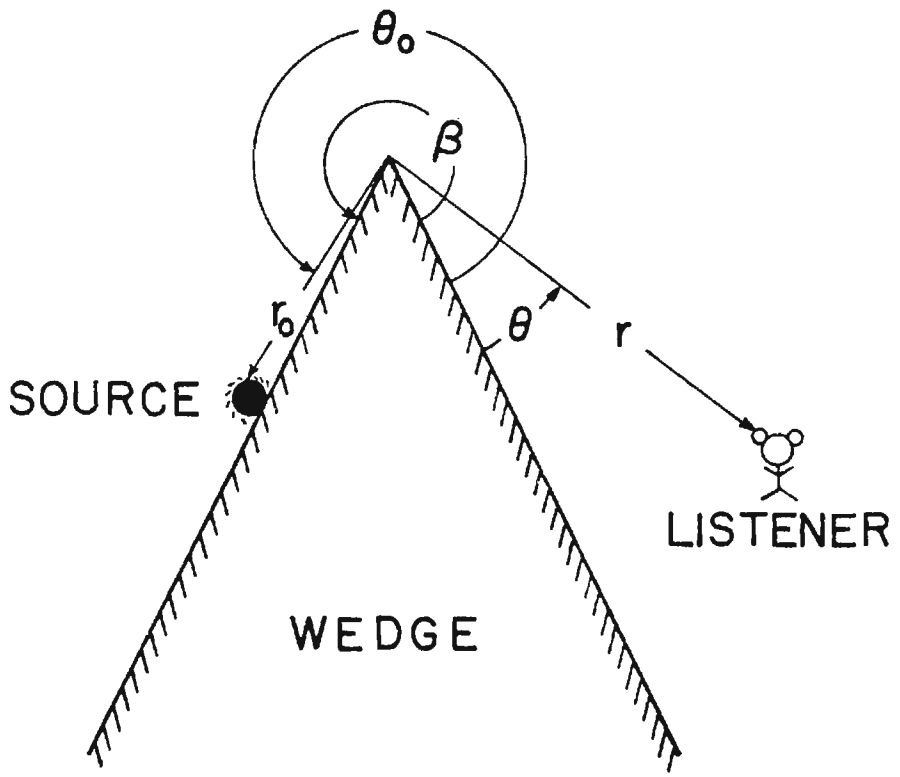

Figure 3-1. Definition of Symbols for Diffraction of Sound Waves from a Point Source by a Rigid Wedge of Exterior Angle β

acoustic pressure field in the immediate vicinity of the source is given by e^{ikR}/R where the time dependence factor, $e^{-i\omega t}$, is understood but omitted for simplicity. Here R, the direct distance from the source to the listener, is considered to be less then the distance from the source to the wedge.

The governing equation for the wedge diffraction problem due to a single harmonic point source is essentially the scalar Helmholtz equation with the customary source term $-4\pi\delta(\bar{r}-\bar{r}_o)$ on the right hand side. This is given by

$$(\nabla^2+k^2)G = -4\pi\ \delta(\bar{r}-\bar{r}_o) \tag{3.1}$$

where G represents the Green's function at the listener. The function $\delta(\bar{r}-\bar{r}_o)$ is known as the Dirac delta function. The above equation can be written in cylindrical coordinate system as

$$\left(\frac{\partial^2}{\partial r^2} + \frac{1}{r}\frac{\partial}{\partial r} + \frac{1}{r^2}\frac{\partial^2}{\partial \theta^2} + k^2\right)G = -4\pi\delta(\bar{r}-\bar{r}_o). \tag{3.2}$$

The diffracted wave contribution to the Green's function must satsify equation (3.2) subject to appropriate boundary conditions at the faces of the rigid wedge, i.e., $\frac{\partial G}{\partial \theta} = 0$ at $\theta=0$ and $\theta=\beta$, respectively, and the Sommerfeld radiation condition at infinity. In order to derive a solution of the above boundary-value problem, a solution can be assumed in terms of a contour integral in the complex ζ plane as

$$G(\bar{r},\bar{r}_o) = \frac{1}{2\pi i}\int_C \frac{e^{ikR(\zeta)}}{R(\zeta)} f(\theta,\zeta)d\zeta \qquad (3.3)$$

with an appropriately chosen contour C and a function $f(\theta,\zeta)$. Here $\frac{e^{ikR(\zeta)}}{R(\zeta)}$ represents the free space Green's function were the wedge not present. The function $R(\zeta)$ is given by

$$R(\zeta) = [r^2+r_o^2 - 2rr_o\cos\zeta + (z-z_o)^2]^{1/2} \qquad (3.4)$$

and is chosen such that it is real and positive along the real ζ axis. One requires to consider that $R(\zeta)$ be analytic everywhere except at branch cuts (Fig. 3-2). Branch cuts are lines going vertically upward or downward from branch points above and below the real ζ axis, respectively. These branch points, obtained by letting $R(\zeta) = 0$ in equation (3.4), are at

$$\zeta = 2m\pi \pm i\alpha \qquad (3.5)$$

where $m=0, \pm1, \pm2, \ldots.$

and $\cosh\alpha = (r^2+r_o^2 + (z-z_o)^2)/(2rr_o).$

The function $R(\zeta)$ has the period 2π in ζ. As regards the choice of the contour C, let it suffice here to say that one wishes to choose the contour such that the integral of equation

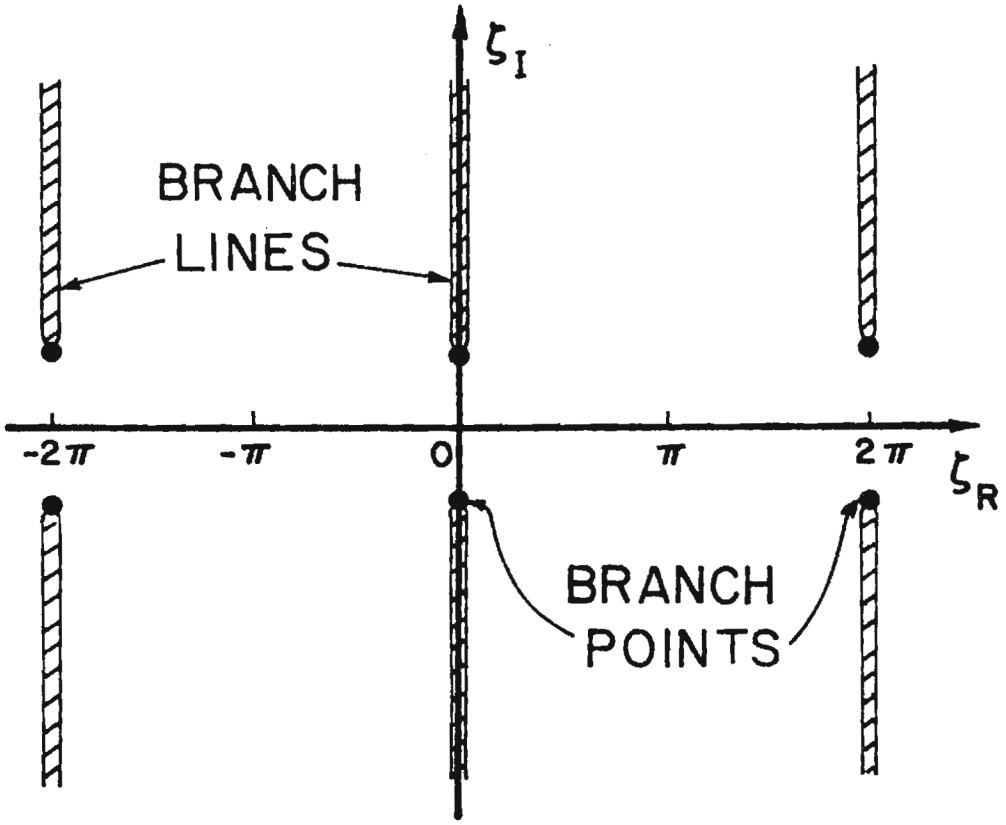

Figure 3-2. Branch Points and Branch Cuts in the Complex ζ Plane

(3.3) converges, i.e., $\frac{e^{ikR(\zeta)}}{R(\zeta)} \to 0$ sufficiently fast at the ends of the contour C.

Up to this point, nothing has been said about the function $f(\theta,\zeta)$. It will be assumed that except at the existing poles $f(\theta,\zeta)$ is a continuous and analytic function of ζ. Using the expression of $G(\bar{r},\bar{r}_o)$ in equation (3.3), $(\nabla^2+k^2)G$ can be written as

$$(\nabla^2+k^2)G = \frac{1}{2\pi i}\int_C \left[\frac{e^{ikR}}{R}\frac{1}{r^2}\frac{\partial^2}{\partial\theta^2}f(\theta,\zeta) - \frac{f(\theta,\zeta)}{r^2}\frac{\partial^2}{\partial\zeta^2}\frac{e^{ikR}}{R}\right]d\zeta.$$

After integrating by parts twice, $(\nabla^2+k^2)G$ can be written as:

$$(\nabla^2+k^2)G = \frac{1}{2\pi i}\int_C \frac{e^{ikR(\zeta)}}{R(\zeta)}\frac{1}{r^2}\left(\frac{\partial^2}{\partial\theta^2} - \frac{\partial^2}{\partial\zeta^2}\right)f(\theta,\zeta)d\zeta. \quad (3.6)$$

For points which are not at the source, the above expression, according to equation (3.1) (with $-4\pi\delta(\bar{r}-\bar{r}_o)$ equal to zero), is zero provided that

$$\left[\frac{\partial^2}{\partial\theta^2} - \frac{\partial^2}{\partial\zeta^2}\right]f(\theta,\zeta) = 0. \quad (3.7)$$

This has the general solution

$$f(\theta,\zeta) = g_1(\zeta+\theta) + g_2(\zeta-\theta) \quad (3.8)$$

where g_1, g_2 are arbitrary functions.

The boundary conditions at the wedge surface can now be imposed on $f(\theta,\zeta)$ of equation (3.8). Thus $\frac{\partial f}{\partial \theta} = 0$ at $\theta=0$ is satisfied if $g_1(\zeta) = g_2(\zeta) = g(\zeta)$. This suggests that $g(\zeta)$ is an odd function of its argument ζ. The other boundary condition, $\frac{\partial f}{\partial \theta} = 0$ at $\theta=\beta$, is satisfied if $g(\zeta+2\beta) = g(\zeta)$, i.e., $g(\zeta)$ is periodic in ζ with a period of 2β. Apart from this, $g(\zeta)$ is arbitrary. The Green's function can then be expressed as

$$G = \frac{1}{2\pi i} \int_C \frac{e^{ikR(\zeta)}}{R(\zeta)} [g(\zeta+\theta)+g(\zeta-\theta)]d\zeta \qquad (3.9)$$

which satisfies the wave equation and the boundary conditions on the wedge surfaces.

Since Green's function satisfies the reciprocity principle, it must also satisfy the wave equation at the source where r approaches r_o, θ approaches θ_o and z approaches z_o. This does not change the value of the function $R(\zeta)$ but requires the θ_o dependency of the arbitrary function $f(\theta,\zeta)$ and hence of the function $g(\zeta+\theta) + g(\zeta-\theta)$. This can be obtained with the application of the method of images for a point source in front of a rigid plane. The expression for the θ_o dependency is given by

$$g(\zeta) = h(\zeta+\theta_o) + h(\zeta-\theta_o)$$

and equation (3.9) then becomes

$$G = \frac{1}{2\pi i} \int_C \frac{e^{ikR}}{R} [h(\zeta+\theta+\theta_o)+h(\zeta+\theta-\theta_o) + h(\zeta-\theta+\theta_o)+h(\zeta-\theta-\theta_o)]d\zeta \quad (3.10)$$

or,

$$G = \frac{1}{2\pi i} \int_C \frac{e^{ikR(\zeta)}}{R(\zeta)} \Sigma h(\zeta,\theta) d\zeta \quad (3.11)$$

where $(\Sigma h(\zeta,\theta))$ is an abbreviation for the sum of the four $h(\zeta,\theta)$ terms in equation (3.10).

Near the source location where $\alpha \to o$ in equation (3.5) the Green's function expression (i.e., equation (3.11)) exhibits proper singular behavior. The $h(\zeta,\theta)$ functions in equation (3.11) have poles whenever they repeat themselves at intervals of 2β. Thus, the function $\Sigma h(\zeta)$ has residues of appropriate values at the poles such that the contour integration around each pole would give a term (in the evaluation of equation (3.10) equal to $\frac{e^{ikR(\zeta)}}{R(\zeta)}$ (i.e., residue of $h(\zeta)$ at each such pole is unity) when geometry indicates the presence of incident or reflected waves. Since $g(\zeta,\theta)$ in equation (3.9) is an odd function in ζ, $h(\zeta)$ is an odd function of ζ and so $\Sigma h(\zeta,\theta)$ is even in θ for fixed values of ζ and θ_o. Also, since $g(\zeta)$ is periodic in ζ with a period 2β, $h(\zeta)$ is periodic in ζ with period 2β. Moreover, if one replaced θ by $2\beta-\theta$ in $\Sigma h(\zeta,\theta)$, uses the periodicity property of $h(\zeta)$, and then uses the fact that each term in $h(\zeta)$ is odd

in its argument, one finds the value of $\Sigma h(\zeta,\theta)$ to remain unchanged. Thus, $\Sigma h(\zeta,\theta)$ must be even about $\theta=\beta$. A suitable choice for the function $h(\zeta)$ is given by

$$h(\zeta) = \frac{\pi/(2\beta)}{\tan(\frac{\pi}{2\beta}\zeta)} \tag{3.12}$$

which satisfies all the above criteria and repeats itself at intervals of 2β. Thus, with

$$\nu = \pi/\beta \tag{3.13}$$

where ν is a wedge index the terms $h(\zeta+\theta\pm\theta_o) + h(\zeta-\theta\mp\theta_o)$ in equation (3.10) can be expressed as

$$h(\zeta+\theta\pm\theta_o) + h(\zeta-\theta\mp\theta_o) = \frac{\nu\sin(\nu\zeta)}{\cos\nu(\theta\pm\theta_o)-\cos(\nu\zeta)}. \tag{3.14}$$

Accordingly, the term $\Sigma h(\zeta,\theta)$ in equation (3.11) can be rewritten as

$$\Sigma h(\zeta,\theta) = Q(\zeta,\theta+\theta_o) + Q(\zeta,\theta-\theta_o) \tag{3.15}$$

where $Q(\zeta,\theta\pm\theta_o) = -\nu\sin(\nu\zeta)/[\cos(\nu\zeta)-\cos(\nu[\theta\pm\theta_o])]$. Finally, equation (3.10) can be written as

$$G = \frac{1}{2\pi i}\int_C \frac{e^{ikR(\zeta)}}{R(\zeta)}\,[Q(\zeta,\theta+\theta_o) + Q(\zeta,\theta-\theta_o)]\,d\zeta\,. \tag{3.16}$$

Equation (3.10) also satisfies the Sommerfeld radiation condition at infinity by virture of the free space Green's function $e^{ikR(\zeta)}/R(\zeta)$ which satisfies this condition for any value of ζ.

In order to obtain suitable expressions for the integral in equation (3.16), at large distances from the diffracting edges compared to a wavelength (i.e., large $R(\zeta)$), the path of integration (i.e., the contour C) can be chosen as shown in Fig. 3-3,i.e., the contour crosses the real axis at $\zeta = 0$ and $\zeta = \pi$, provided proper care has been taken for the poles lying between 0 and π. This can be done by considering another contour C_{111} which encircles all such poles in the counterclockwise sense. Since $\frac{e^{ikR(\zeta)}}{R(\zeta)} \to 0$ as $\zeta_I \to \infty$ for ζ_R between 0 and π, the deformed contour can be split into three segments, C_1, C_{1P} and C_{111} (Fig. 3-3). The path C_1 goes from $\zeta = -\pi/2 - i\infty$ to $\zeta = \frac{\pi}{2} + i\infty$ where as the path C_{11} goes from $\zeta = \frac{\pi}{2} + i\infty$ to $\zeta = \frac{3\pi}{2} - i\infty$. The integration along the contour C_{111} around each pole are evaluated by Cauchy's residue theorem. The contributions to these integrals come only from the residue terms and the branch line integrations. Each residue term corresponds either to an incident wave or a specularly reflected wave while the branch line integrals along the paths C_1 and C_{11} represent the diffracted waves. Thus, equation (3.16) can be expressed as

$$G = G_{dir} + G_{refl,0} + G_{refl,\beta} + G_{diffr}. \qquad (3.17)$$

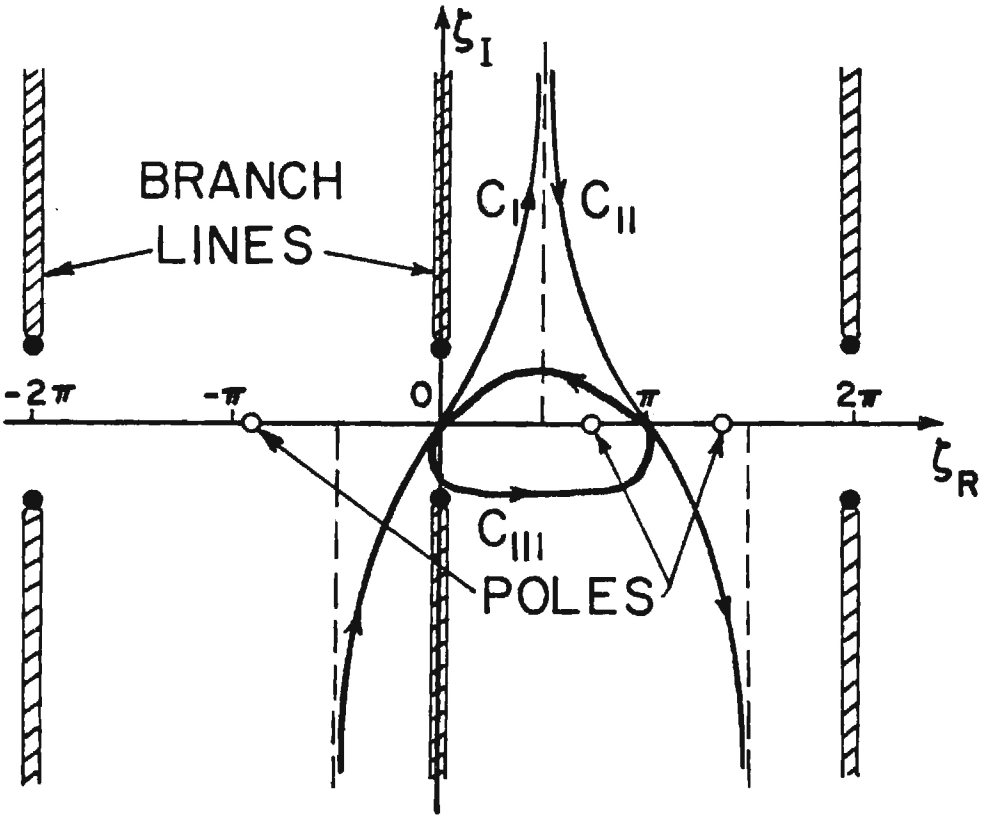

Figure 3-3. Deformed Integration Contour in the Complex ζ Plane for Evaluation of the Acoustic Field of the Wedge Diffraction Problem

The terms are interpreted as a direct wave (G_{dir}), a wave ($G_{refl,0}$) reflected from the $\theta = 0$ side of the wedge, a wave ($G_{refl,\beta}$) reflected from the $\theta = \beta$ side and a diffracted wave (G_{diffr}) (Fig. 3-4). The criterion for the existence of the direct wave is that the listener be able to see the source, i.e., the line joining the source and the listener should not penetrate the wedge and $|\theta-\theta_o|<\pi$. Similarly, the reflected waves $G_{refl,0}$ and $G_{refl,\beta}$ are present if specularly reflected rays for which the angle of incidence equals the angle of reflection can be constructed from the source to the $\theta = 0$ and $\theta = \beta$ face and thence to the listener. Criterion for the existence of the $G_{refl,0}$ reflected wave is that $\theta+\theta_o<\pi$ and that for $G_{refl,\beta}$ reflected wave is that $\theta+\theta_o>2\beta-\pi$. If any of these criterion are not satisfied, the contributions from the corresponding term in equation (3.17) will be zero.

After the solution has been constructed according to the geometrical acoustic principles, all that is left is the nonzero diffracted wave G_{diffr}. Even though the diffracted wave may be sometimes negligible compared to some of the other waves in equation (3.17) depending on the source-listener configuration, this is the sole field in the shadow zone where all the other terms are zero. Since the overall solution has to be continuous in θ and the direct and reflected waves (G_{dir}, $G_{refl,0}$, $G_{refl,\beta}$) are discontinuous, the diffracted wave G_{diffr} is also expected to be discontinuous in order to compensate the discontinuities in the geometrical acoustic terms.

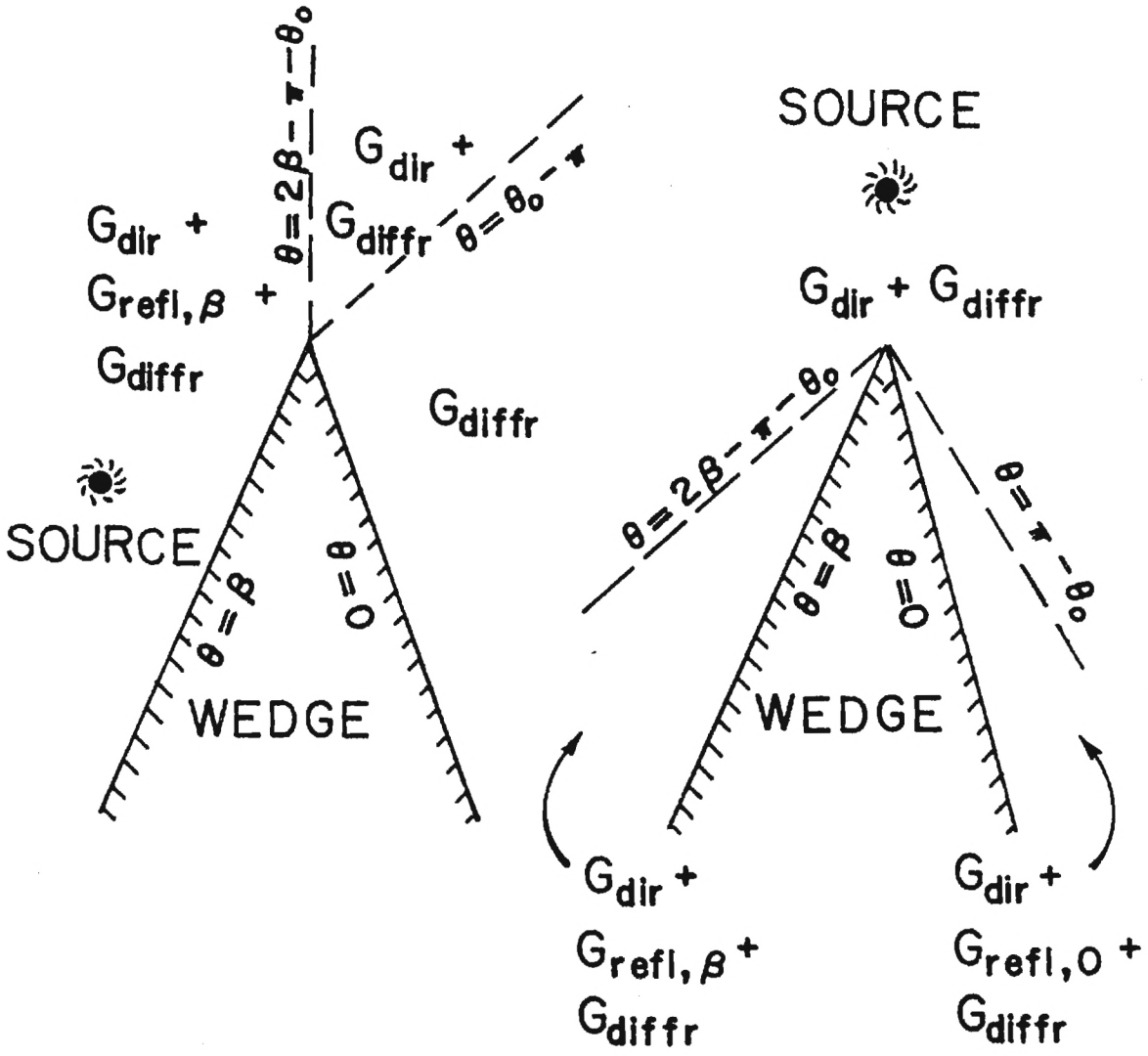

Figure 3-4. Sketch of Regions Separating Various Types of Waves for Two Different Source Locations. The Dashed Lines Indicate Boundaries Between the Various Regions.

Asymptotic Solution for the Diffracted Waves

Single-Edge Diffraction

For a listener in the acoustic shadow zone, the major contribution at large distances r from the edge comes from the diffracted waves, i.e., C_1 and C_{11} portions of the contour integral in equation (3.16). The direct wave or a specularly reflected wave which is the C_{111} portion of the contour integration does not exist in the shadow zone. Appropriate expressions for the uniform asymptotic limit of the diffracted wave G_{diffr} (where both the source and the listener are far away from the edge of the wedge) can be derived (as outlined by Pierce [35]) in terms of uniform asymptotic expressions with an extension of the well-known saddle point approximation [36] to the contour integration of equation (3.16). Since both the functions $Q(\zeta,\theta+\theta_o)$ and $Q(\zeta,\theta-\theta_o)$ in equation (3.16) are odd functions in ζ and since the steepest descent path through $\zeta = 0$ may be taken as symmetric with respect to inversions through the origin, i.e., even about $\zeta = 0$, the integral along the contour C_1 vanishes identically. Therefore, the contributions of all the diffracted rays come from the C_{11} portion of the contour integral in equation (3.16).

Singular expressions are obtained near the boundaries (separating illuminated and shadow regions) when $Q(\zeta,\theta\pm\theta_o)$ is simply replaced by $Q(\pi,\theta\pm\theta_o)$ in the integrand of equation (3.16). In order to avoid this, equation (3.16) will be approximated by the power series expansion of $R(\zeta)$ and

$Q(\zeta,\theta\pm\theta_o)$. The denominator of $Q(\zeta,\theta\pm\theta_o)$ is expressed in terms of a power series in $\zeta-\pi$ up to its first order term. The numerator may be approximated by simply changing ζ by π. Thus the expression for $Q(\zeta,\theta\pm\theta_o)$ near the saddle point $\zeta = \pi$ is given by

$$Q(\zeta,\theta\pm\theta_o)\Big|_{\zeta=\pi} = \frac{-1}{M_\nu(\theta\pm\theta_o)-(\zeta-\pi)} \tag{3.18}$$

where $$M_\nu(\theta\pm\theta_o) = \frac{\cos(\nu\pi)-\cos(\nu[\theta\pm\theta_o])}{\nu\sin(\nu\pi)} \; . \tag{3.19}$$

The exponent ikR in equation (3.16) is expanded up to the second order term in a power series in $\zeta-\pi$. Consequently, one obtains

$$ikR = ik\left(L - \frac{rr_o}{2L}(\zeta-\pi)^2\right) \tag{3.20}$$

where $$L = [(r+r_o)^2 + (z-z_o)^2]^{1/2} . \tag{3.21}$$

Here z and z_o represent the height of the source and the listener, respectively. It is to be noted that the first order term in $\zeta-\pi$ vanishes identically as $\zeta = \pi$ is the saddle point of $\exp(ikR)$. The amplitude factor R^{-1} is approximated by replacing ζ by π in the expression of R in equation (3.4) resulting $R \simeq L$. Finally, the expression for the approximation

to the diffracted wave is given by

$$G_{diffr} = \frac{1}{2\pi i} \frac{e^{ikL}}{L} \int_{C_{11}} e^{\frac{-rr_o}{L}} e^{\frac{ik}{2}(\zeta-\pi)^2} [Q(\zeta-\pi,\theta+\theta_o) +$$

$$Q(\zeta-\pi,\theta-\theta_o)]d(\zeta-\pi) . \qquad (3.22)$$

As regards to the actual integration, one now integrates equation (3.22) along the line of the steepest descent of the approximate integrand going obliquely downwards making an angle of 45° with the real part of ζ-axis and passing through the saddle point at $\zeta = \pi$. Changing the integration variable from $\zeta-\pi$ to T where

$$(\zeta-\pi) = Te^{-i\pi/4} \qquad (3.23a)$$

and incorporating new integration limits, one obtains

$$G_{diffr} = \frac{1}{2\pi} \frac{e^{ikL}}{L} \int_{-\infty}^{\infty} e^{\frac{-rr_o}{L}\frac{kT^2}{2}} e^{-i\pi/4} [Q(\zeta-\pi,\theta+\theta_o)$$

$$+ Q(\zeta-\pi,\theta-\theta_o)]dT . \qquad (3.23b)$$

Now, by replacing

$$\frac{rr_o}{L}\frac{kT^2}{2} = u^2 \qquad (3.24a)$$

one may write

$$G_{diffr} = \frac{\sqrt{2}}{2\pi} \frac{e^{i\pi/4}}{\sqrt{2}} \frac{e^{ikL}}{L} \left[\int_{-\infty}^{\infty} \left\{ \frac{e^{-u^2}}{\sqrt{\frac{\pi}{2}}\sqrt{\frac{2rr_o}{\lambda L}}\, M_\nu(\theta+\theta_o) - ue^{-i\pi/4}} \right.\right.$$

$$\left.\left. + \frac{e^{-u^2}}{\sqrt{\frac{\pi}{2}}\sqrt{\frac{2rr_o}{\lambda L}}\, M_\nu(\theta-\theta_o) - ue^{-i\pi/4}} \right\} du \right] \qquad (3.24b)$$

where λ is the wavelength given by

$$\lambda = \frac{2\pi}{k} .$$

Finally, the approximate expression for the diffracted wave contribution to the Green's function is given by

$$G_{diffr} = \left(\frac{e^{ikL}}{L}\right)\left(\frac{e^{i\pi/4}}{\sqrt{2}}\right)\left[A_D(X_+) + A_D(X_-)\right] \qquad (3.25)$$

where $A_D(X_{\pm})$ is the diffraction integral given by

$$A_D(X_{\pm}) = \frac{\sqrt{2}}{2\pi} \int_{-\infty}^{\infty} \frac{e^{-u^2}\, du}{\sqrt{\frac{\pi}{2}}\; X_{\pm} - ue^{-i\pi/4}} . \qquad (3.26)$$

The arguments X_+ and X_- are

$$X_+ = X(\theta+\theta_o) \tag{3.27a}$$

$$X_- = X(\theta-\theta_o) \tag{3.27b}$$

and

$$X(\theta\pm\theta_o) = \Gamma M_\nu(\theta\pm\theta_o) \tag{3.28}$$

where

$$\Gamma = \sqrt{\frac{2rr_o}{\lambda L}} \tag{3.29}$$

and ν is as defined in equation (3.13).

The diffraction integral $A_D(X)$ can be expressed in terms of auxiliary Fresnel functions f(X) and g(X) [37] as

$$A_D(X) = \text{sign}(X)[f(X)-ig(X)] \tag{3.30}$$

The diffraction integral has the property that it is odd in X and discontinuous at X = 0. The Fresnel functions f(X) and g(X) are related to the Fresnel integrals

$$C(X) = \int_o^X \cos([\pi/2]t^2)dt \tag{3.31a}$$

and

$$S(X) = \int_0^X \sin([\pi/2]t^2)dt \qquad (3.31b)$$

by

$$f(X) = [\tfrac{1}{2}-S]\cos([\pi/2]X^2) - [\tfrac{1}{2}-C]\sin([\tfrac{\pi}{2}]X^2) \qquad (3.32a)$$

and

$$g(X) = [\tfrac{1}{2}-C]\cos([\pi/2]X^2) - [\tfrac{1}{2}-S]\sin([\tfrac{\pi}{2}]X^2). \qquad (3.32b)$$

On the basis of relations given in the NBS Handbook of Mathematical Functions [37], one can conclude that for small X

$$f(X) = \tfrac{1}{2} - (\tfrac{\pi}{4})X^2 + (\tfrac{\pi}{3})X^3 - \ldots. \qquad (3.33a)$$

$$g(X) = (\tfrac{1}{2}) - X + (\tfrac{\pi}{4})X^2 - \ldots. \qquad (3.33b)$$

and for large X

$$f(X) = \frac{1}{\pi X} - \frac{3}{\pi^3 X^5} + \ldots. \qquad (3.34a)$$

$$g(X) = \frac{1}{\pi^2 X^3} - \frac{15}{\pi^4 X^7} + \ldots. \qquad (3.34b)$$

The single-edge diffracted wave contribution to the Green's Function for a point source on a rectangular box is given by equation (3.25) with $\beta = 3\pi/2$ in equations (3.27a)

through (3.29b). One such term is to be included in the Green's function for each arrangement of source and listener locations such that a diffracted ray path can be drawn in accordance with the laws of the geometrical theory of diffraction from the source point to a diffracting edge and thence to the listener location.

Double-Edge Diffraction

An approximate expression for the double-edge diffraction contribution to the Green's function can be derived from the superposition of two single-edge diffraction problems as proposed by Pierce [35] and Hadden [38]. Figure 3-5 shows the configuration of the source (r_S,θ_S,z_S), the listener (r_L,θ_L,z_L) and the three planar segments of the double-edge wedge with both the edges parallel to the z-axis. The source and the listener are assumed to be closest to the left and right side of the wedge, respectively. The parameters which are involved in the discussion of sound diffraction by a double-edge wedge of exterior angles β_S and β_L are defined in Fig. 3-5.

The conceptual device applied to the decomposition of the double-edge diffraction problem into two single-edge diffraction problems may be viewed as follows. Each wave is originated at a "fictitious" source located in the extension plane of the top of the double-edge wedge and propagated over the top surface before being diffracted by the listener-side edge. The pressure on the top of the wedge is attributed to

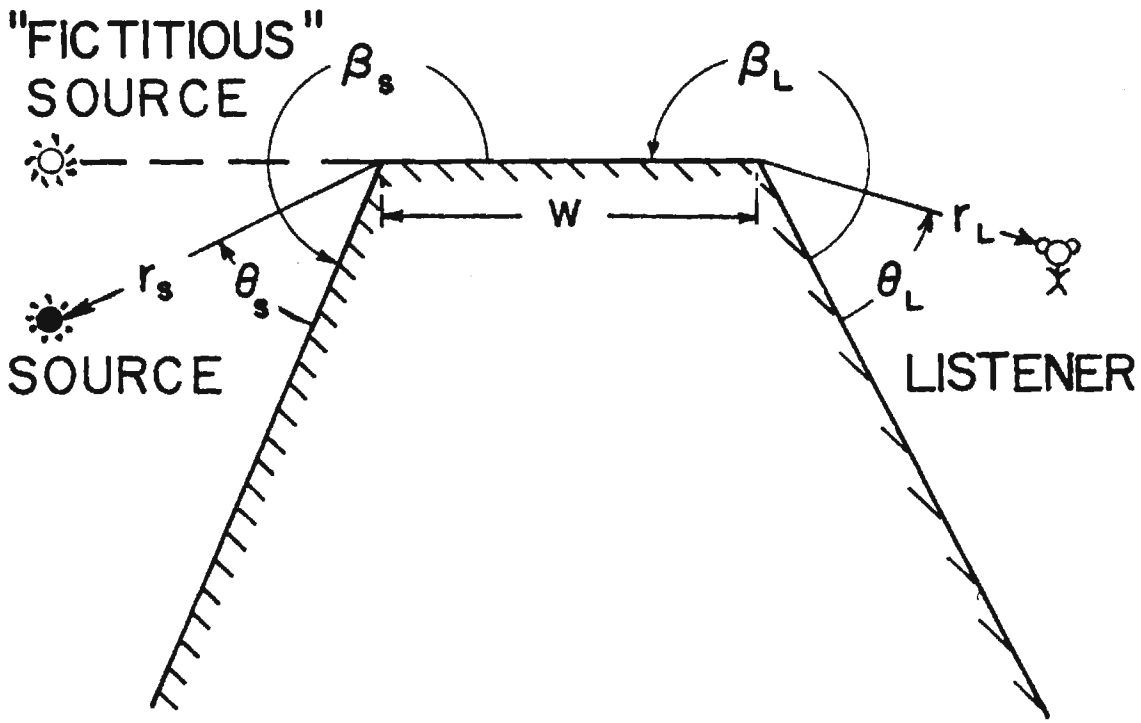

Figure 3-5. Definition of Symbols for Sound Diffraction by a Double-Edge Wedge

single-edge diffracted waves due to the edge closest to the source. In order to match these two single-edge diffraction effects, the points of diffraction on the edge nearest the listener are first determined such that the diffracted rays from the actual source to the listener pass through those points. Next, the pressure diffracted by the edge on the source side is equated to the pressure propagating over the top surface of the wedge due to the corresponding "fictitious" source. The "fictitious" source location needed for deriving the double-edge diffraction expression may be chosen on the basis of matching the spreading characteristics according to the geometrical theory of diffraction on the top of the wedge. Finally, the approximate expression to the Green's function for the doubly diffracted waves is given by [35]

$$G_{diffr}\Big|_D = i\,\frac{e^{ikL}}{L}\,[f(Y_>)-ig(Y_>)][f(BY_<)-ig(BY_<)] \qquad (3.35)$$

where $Y_>$ and $Y_<$, the argument of the auxiliary Fresnel functions, are the greater and smaller, respectively, of the quantities Y_S and Y_L which are defined as

$$Y_S = \gamma_S\, M_{\nu_S}\,(\beta_S-\theta_S) \qquad (3.36a)$$

and

$$Y_L = \gamma_L\, M_{\nu_L}\,(\beta_L-\theta_L)\,. \qquad (3.36b)$$

The parameters γ_S and γ_L are then

$$\gamma_S = [2r_S(w+r_L)/\lambda L]^{1/2} \tag{3.37a}$$

$$\gamma_L = [2r_L(w+r_S)/\lambda L]^{1/2} \tag{3.37b}$$

with

$$L = [(r_S=r_L+w)^2 + (z_S-z_L)^2]^{1/2}. \tag{3.38}$$

The function M_{ν_S} and M_{ν_L} is as defined in equation (3.19) with

$$\nu_S = \pi/\beta_S \text{ and } \nu_L = \pi/\beta_L. \tag{3.39}$$

The parameter B in equation (3.35) is given by

$$B = \left[\frac{w(w+r_S+r_L)}{(w+r_S)(w+r_L)}\right]^{1/2} \tag{3.40}$$

may be considered as characterizing the wedge width. The double-edge diffracted wave contribution to the Green's function for a point source on a rectangular box is given by equation (3.35) with $\beta_S = \frac{3\pi}{2}$ and $\beta_L = \frac{3\pi}{2}$ in equation (3.36a) through (3.40).

CHAPTER IV

PROPOSED SCHEME FOR NUMERICAL PREDICTION OF FAR FIELD RADIATION

In the present chapter, a computer oriented prediction scheme is developed for predicting transformer noise radiation from surface acceleration data.* For computational purposes, the four vertical sides of the rectangular box-like structure which approximates the transformer tank resting on the ground are divided into several elements. The most stringent limitation on such an approach, for frequencies of concern with electric transformers, is that the mesh spacing must be sufficiently small such that acoustic field variables, e.g., surface acceleration, in each of these elements, may be considered to be essentially constant (i.e., say mesh spacing less than half the structural wavelength in the tank walls). This is necessary to assure that the integral on the right hand side of equation (2.9) may be accurately replaced by the algebric summation

$$\sum_{j=1}^{N} a_{n_j}(\bar{r}_o)\, dS_{o_j} \left(\sum_{\ell=1}^{M_j} G_{j\ell}(\bar{r}, \bar{r}_o) \right)$$

*With some minor changes, this numerical computation technique can be used to determine the radiated sound field generated by any polygonal vibrating surface.

such that

$$p(\bar{r}) = \frac{\rho_o}{4\pi} \sum_{j=1}^{N} a_{n_j}(\bar{r}_o)\, dS_{o_j} \left(\sum_{\ell=1}^{M_j} G_{j\ell}(\bar{r},\bar{r}_o) \right). \qquad (4.1)$$

Here N is the total number of elements and M_j is the number of terms present in the Green's function expression for each element. Since the acceleration amplitudes on the top surface of a typical transformer are negligible compared to those on the other surfaces, the effect of the top surface is neglected in the computation.

Insofar as the sound reaching the listener from a typical source point is concerned, it is considered as a combination of direct sound and diffracted sound. As it is to be noted that the singly diffracted rays are quantitatively most important compared to any higher order ray, the proposed scheme for numerical prediction of sound radiation is based on sound diffracted by one edge of a semi-infinite right-angled rigid wedge. If the sound must bend around more than one edge in order to reach the listener, the contribution from the corresponding diffracted paths will be considered negligible. However, the approximation to the Green's function $G_{j\ell}(\bar{r},\bar{r}_o)$ in equation (4.1) could be readily extended to account for diffraction by two (or more) edges, but at the cost of considerably more computational bookkeeping and computing time.

The medium outside the transformer is divided into eight regions. A schematic diagram of this arrangement is shown in Fig. 4-1. Here a vertical edge of the tank appears to be a corner when the tank is viewed from the top. When the source is facing the listener and for listeners on or near the ground where the listener height is less than the height of the highest horizontal edge, the single-edge diffracted waves of interest are those which come from both the vertical and the horizontal edges. For example, consider the case where the source is on side 1 and the listener is in region I in Fig. 4-1. If the listener cannot see the source (e.g., source on side 2 and listener in region 1 in Fig. 4-1) the singly diffracted waves that are of interest come from the vertical edges only. The two typical wedge-source-listener configurations which are relevant to the construction of the Green's function are shown in Figs. 4-2 and 4-3. The dashed lines in these figures represent the path followed by the diffracted rays coming from the source to the listener, whereas the solid line in Fig. 4-2 is the path followed by the direct ray.

For computational simplification, the diffracted wave contribution to the Green's function for the semi-infinite right-angled rigid wedge, given by equation (3.25) with $\beta = \frac{3}{2}$, is expressed as

$$G_{diffr}(\bar{r},\bar{r}_o) = -2\,(e^{ikL}/L)(e^{i\pi/4}/\sqrt{2})\{f(|X|) - ig(|X|)\} \qquad (4.2)$$

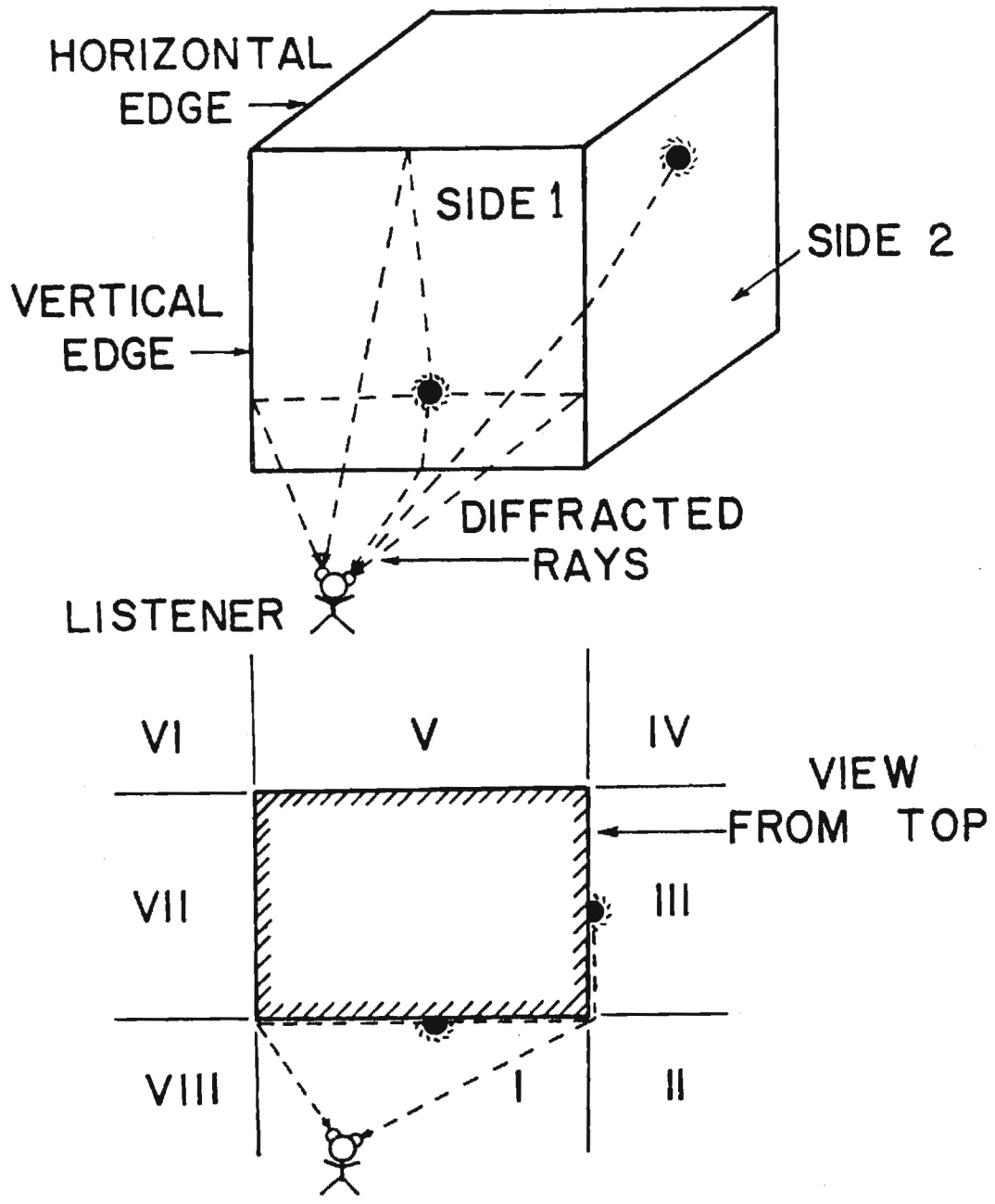

Figure 4-1. Schematic Diagram of the Diffracted Rays and the Divided Regions Outside the Right-Angled Box

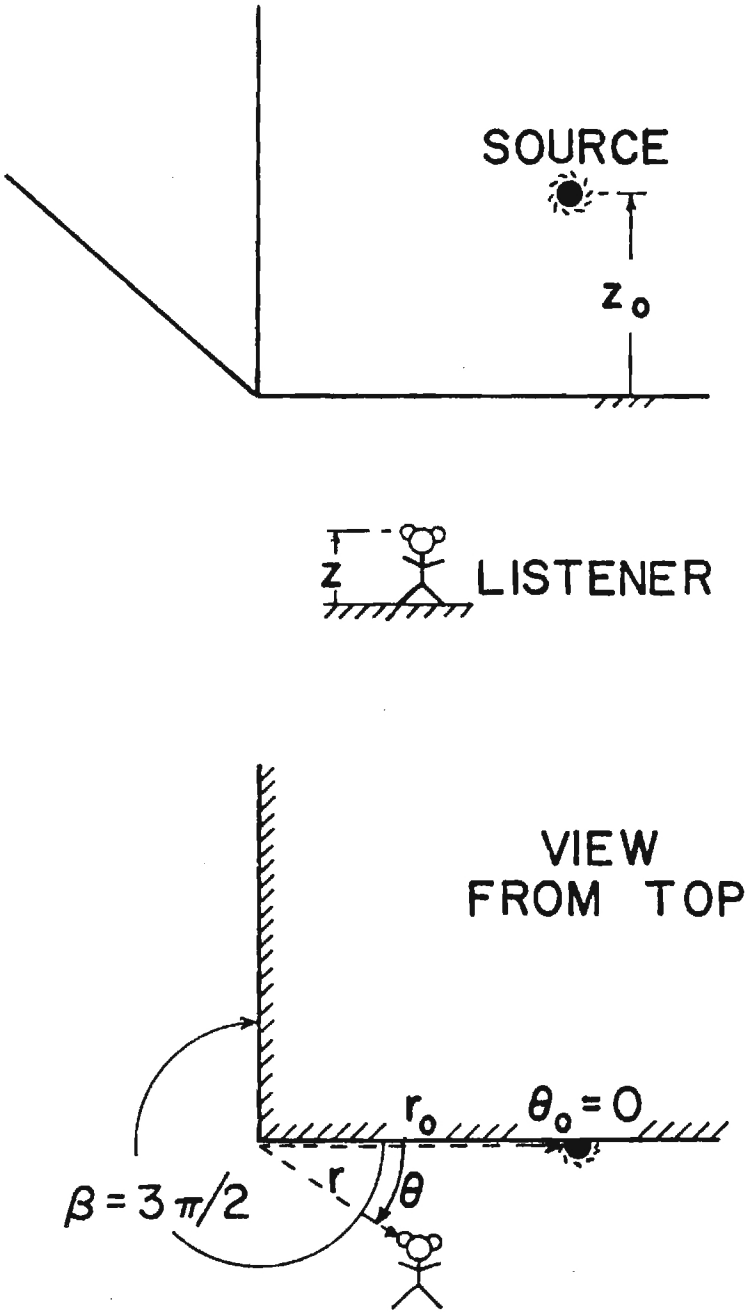

Figure 4-2. Definition of Symbols Used in the Discussion of Sound Diffraction of a Right-Angled Wedge when the Source Faces the Listener

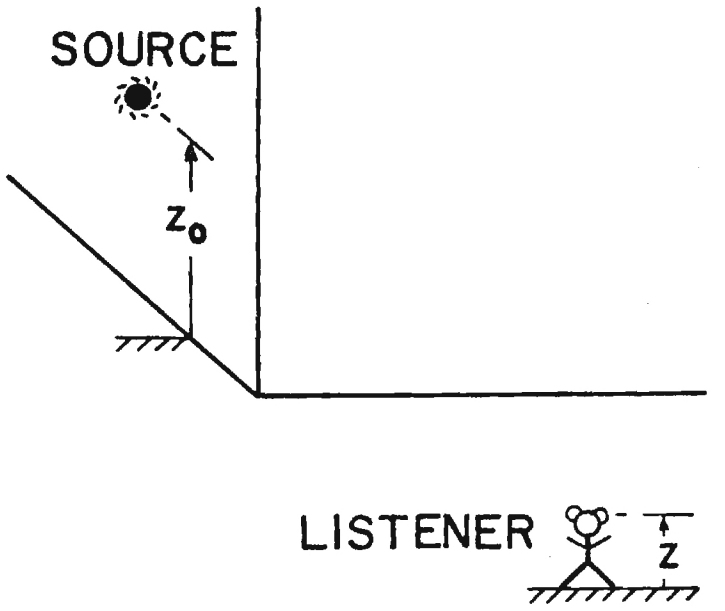

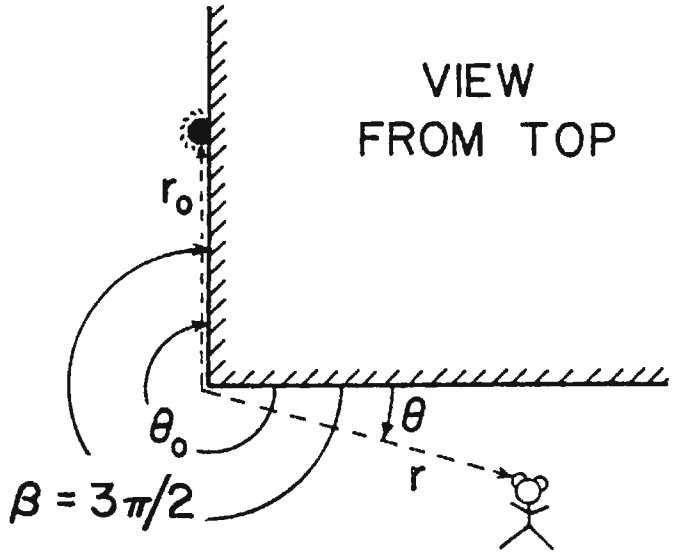

Figure 4-3. Definition of Symbols Used in the Discussion of Sound Diffraction by a Right-Angled Wedge when the Listener cannot see the Source

when the source is facing the listener, i.e., $\theta_o = 0$ in Fig. 4-2. Here $X(\theta)$ is given by

$$X(\theta) = -\sqrt{3}\left(\frac{2rr_o}{\lambda L}\right)^{1/2} (1/2 + \cos\tfrac{2}{3}\theta). \qquad (4.3)$$

Similarly,

$$G_{diffr}(\bar{r},\bar{r}_o) = 2\,(e^{ikL}/L)(e^{i\pi/4}/\sqrt{2})\{f(|X|) - ig\,(|X|)\} \qquad (4.4)$$

when the listener does not see the source, i.e., $\theta_o = \frac{3\pi}{2}$ in Fig. 4-3. The expression for $X(\theta)$ in this case is given by

$$X(\theta) = \sqrt{3}\left(\frac{2rr_o}{\lambda L}\right)^{1/2} (-1/2 + \cos\tfrac{2}{3}\theta). \qquad (4.5)$$

The auxiliary Fresnel functions f(X) and g(X) present in the diffracted wave terms of the Green's function are calculated from equations (7.3.32) and (7.3.33) of the Handbook of Mathematical Functions [34]. If in equation (4.3) or (4.5) $X(\theta)>2$, the contribution of the diffracted wave terms for the corresponding $X(\theta)$ in the Green's function expression is negligible compared to that of any other wave for a given source and listener configuration.

In order to ensure that the appropriate diffraction terms have been included in the Green's function expressions,

one needs to check that the point of diffraction for each of these rays lies on the box-edge and not on the extension of the edge (Fig. 4-4). In other words, one needs to be sure that

$$r_o \leq W - x_o \tag{4.6}$$

where

$$r_o = \frac{z_o L}{r_\ell + z_o} . \tag{4.7}$$

The parameters L, r_o, r_ℓ , x_o, z_o and W are defined in Fig. 4-4.

The direct wave contribution to the Green's function is expressed as

$$G_{dir} = 2\ e^{ikR}/R \tag{4.8}$$

where R is the direct distance from the source to the listener. Such terms are to be used when no box edge obstructs the path from source to listener. It is to be noted that the above direct wave term also includes the contribution from another wave which is reflected from the same face and is in phase with the direct wave.

The value of the Green's function needed to find the acoustic pressure outside the transformer can now be computed from equations (4.1) through (4.8). Therefore, the far-field acoustic pressure and hence the sound pressure level can be obtained by substituting the values of the surface normal

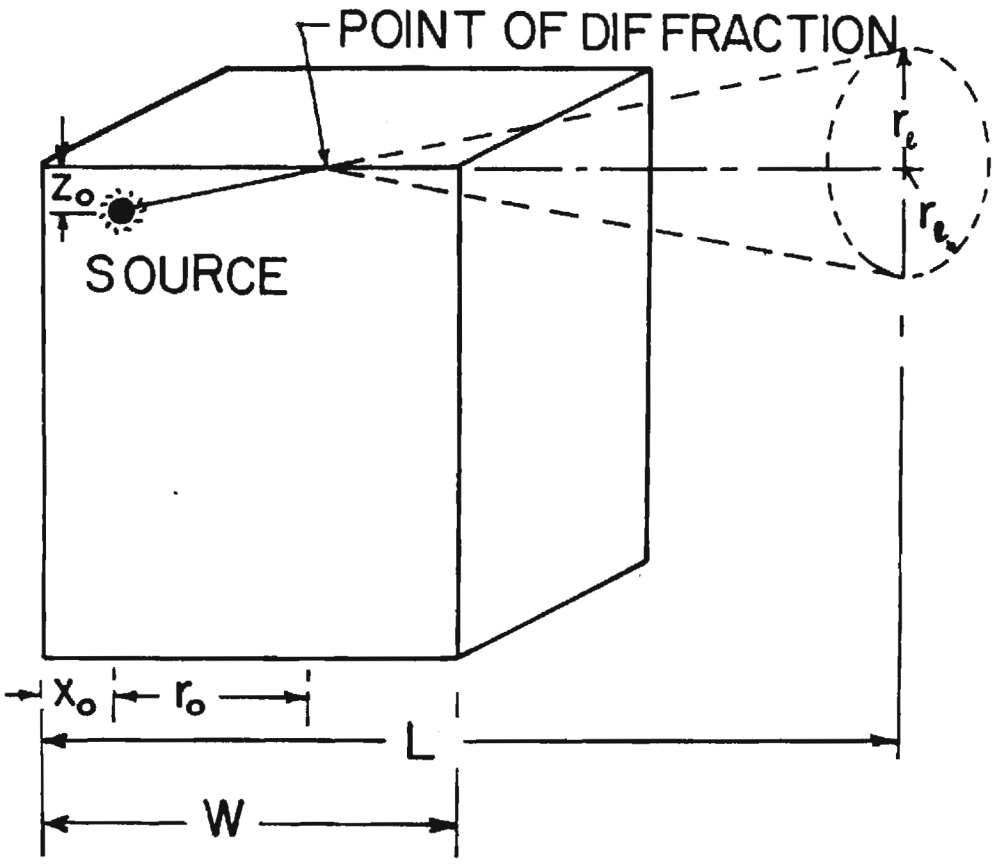

Figure 4-4. Schematic Diagram for the Acceptibility of the Diffraction Terms

acceleration and the corresponding surface areas along with the computed values of the Green's function in equation (4.1). The sound pressure level is given by

$$L_p = 10 \log_{10} \frac{\langle p^2(\bar{r}) \rangle}{(p_{ref}^2)}. \qquad (4.9)$$

Here $\langle p^2(\bar{r}) \rangle$ is the mean squared pressure and p_{ref} represents a reference pressure which for airborne sound is usually taken as 2×10^{-5} Pa.

CHAPTER V

EXPERIMENTAL APPLICATIONS

The significance and the applicability of any theory is perhaps best demonstrated by comparing the theoretical analysis with the experimental results. With this in mind, several applications of the developed technique to experimental data are discussed here. At first, the theoretically calculated far-field radiation patterns, based on equation (4.1), for a simulated electric transformer (Fig. 5-1) are compared with the measured sound pressure levels. The second application concerns the prediction of sound radiation patterns from surface acceleration measurements made on a medium sized production-line transformer. The third application is a comparison with analytical and experimental results obtained for rectangular pistons on a rectangular baffle used by Hutchins and Kouyoumjian [39]. Finally, the proposed prediction scheme is applied to compare the diffraction effects with the available numerical and experimental results from Furue, Terai and Matsu'ura [40].

Both indoor and outdoor experiments were conducted on electric transformers at General Electric's medium size transformer plant site at Rome, Georgia. The outdoor experiment was conducted on a simulation of a medium sized, rectangular transformer on an isolated open field site (Fig. 5-2).

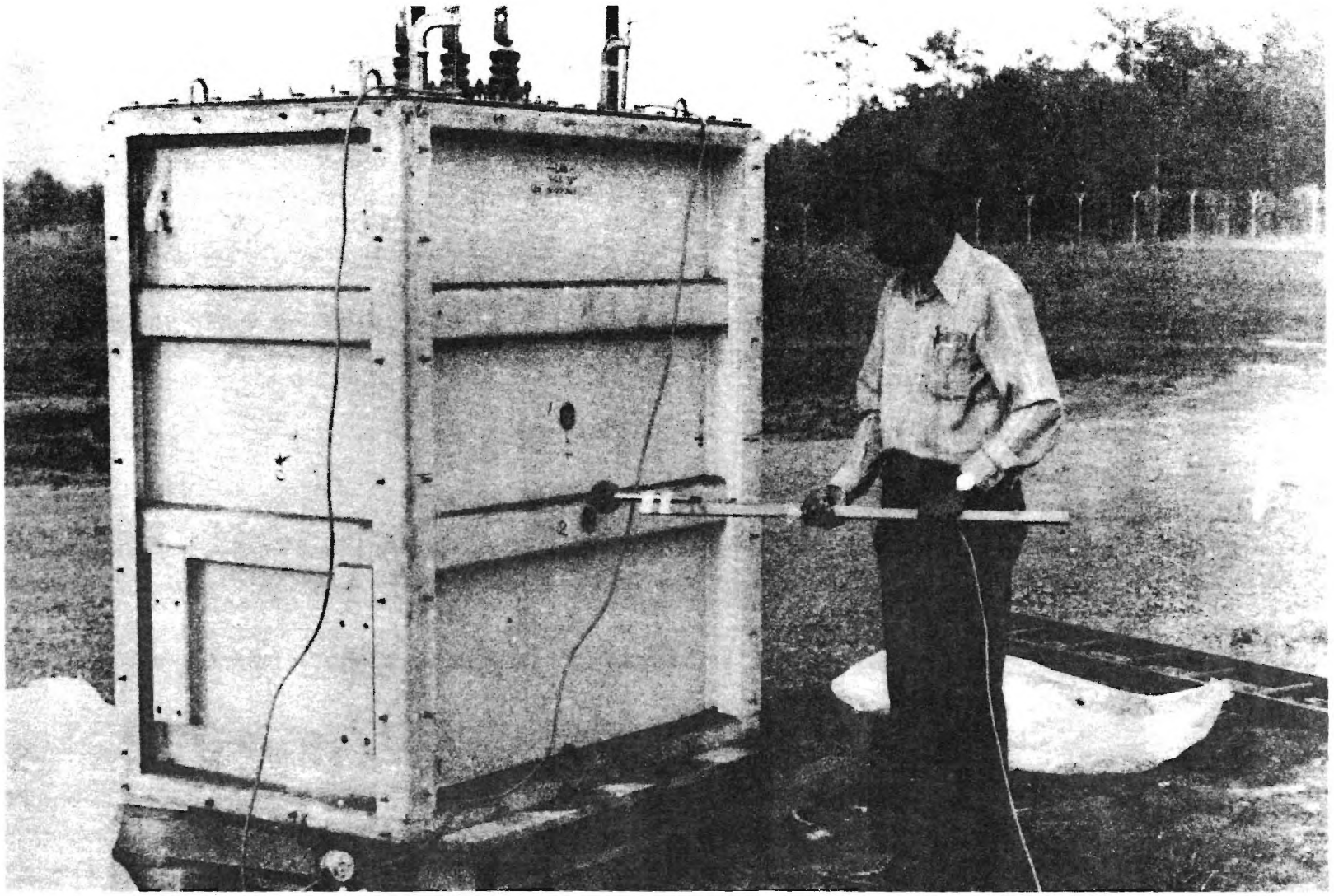

Figure 5-1. Photograph of a Simulated Transformer Used in Experimental Test of Prediction Method

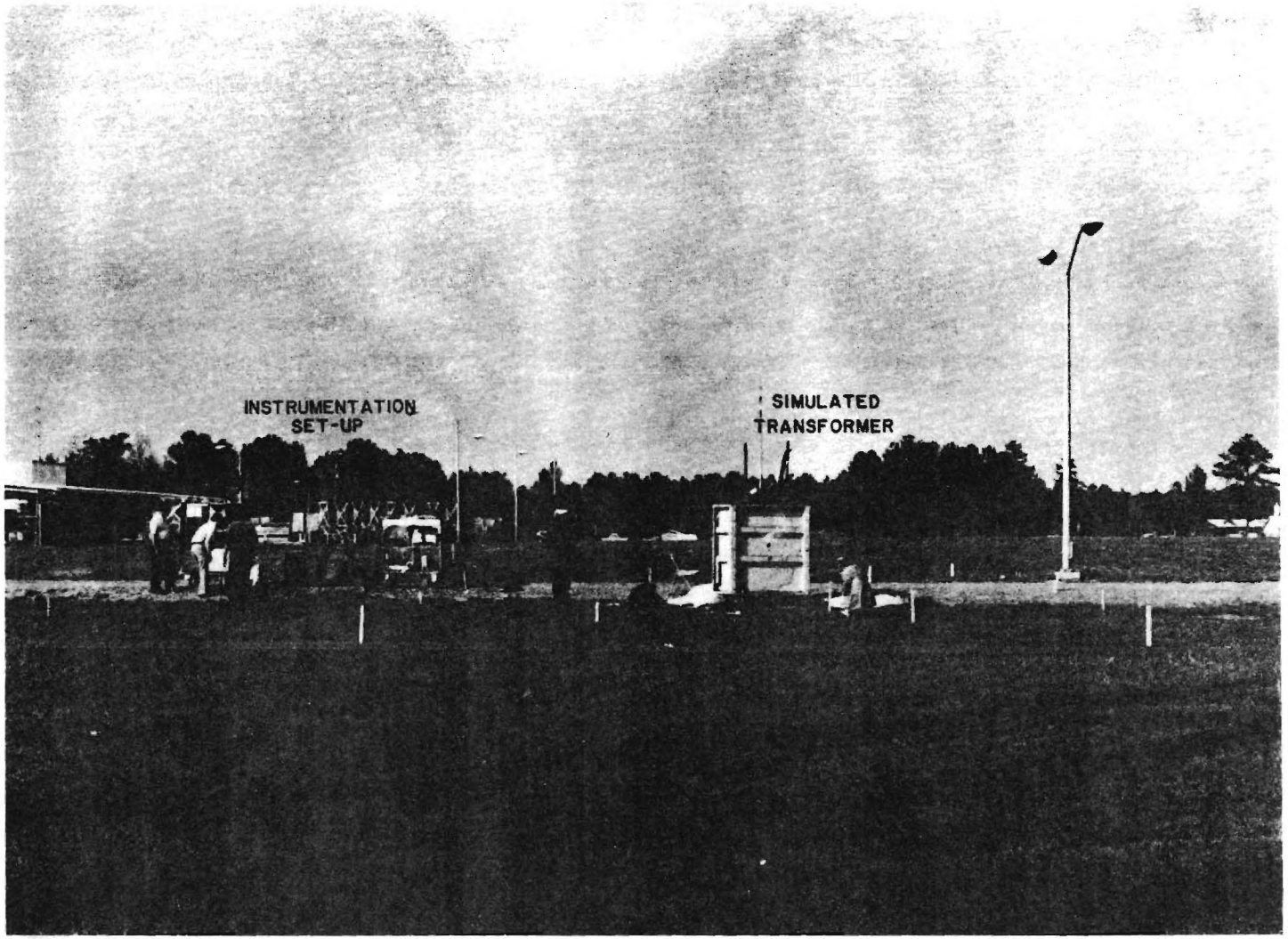

Figure 5-2. Photograph of Outdoor Experimental Field Site

The transformer (Fig. 5-1) was rested on a pallet, which in turn was on the grass covered hard Georgia clay. The simulated transformer consists of a 1.3 m x 0.76 m x 1.52 m transformer tank which is used for outdoor test purposes by the manufacturer. The tank was almost filled with water. Two underwater speakers, both at about equal distances apart from the center of the tank, were immersed in water inside the tank at approximately one half height of the transformer. These speakers were excited at a pure tone frequency of 265 Hz with a General Radio function wave generator. All these were done to simulate the path of noise propagation for the test case with the transmission path of the magnetic core vibration from the iron circuit to the transformer tank wall. Both near field and far field measurements were made for this experiment. The near field data consisted of surface acceleration measurements, whereas the far field data included the sound pressure level measurements for several radial distances and angular locations. A generalized schematic of the experimental arrangement is shown in Fig. 5-3.

The side of the tank containing the main drain valve is termed as the front side of the transformer. The other sides are referred to as right of front, back and left of front sides. On each of the front and the back sides of the transformer, 56 points with 8 rows and 7 columns were uniformly distributed and on each of the other two sides, 40 points in 8 rows and 5 columns were marked at almost uniform spacing. One of the

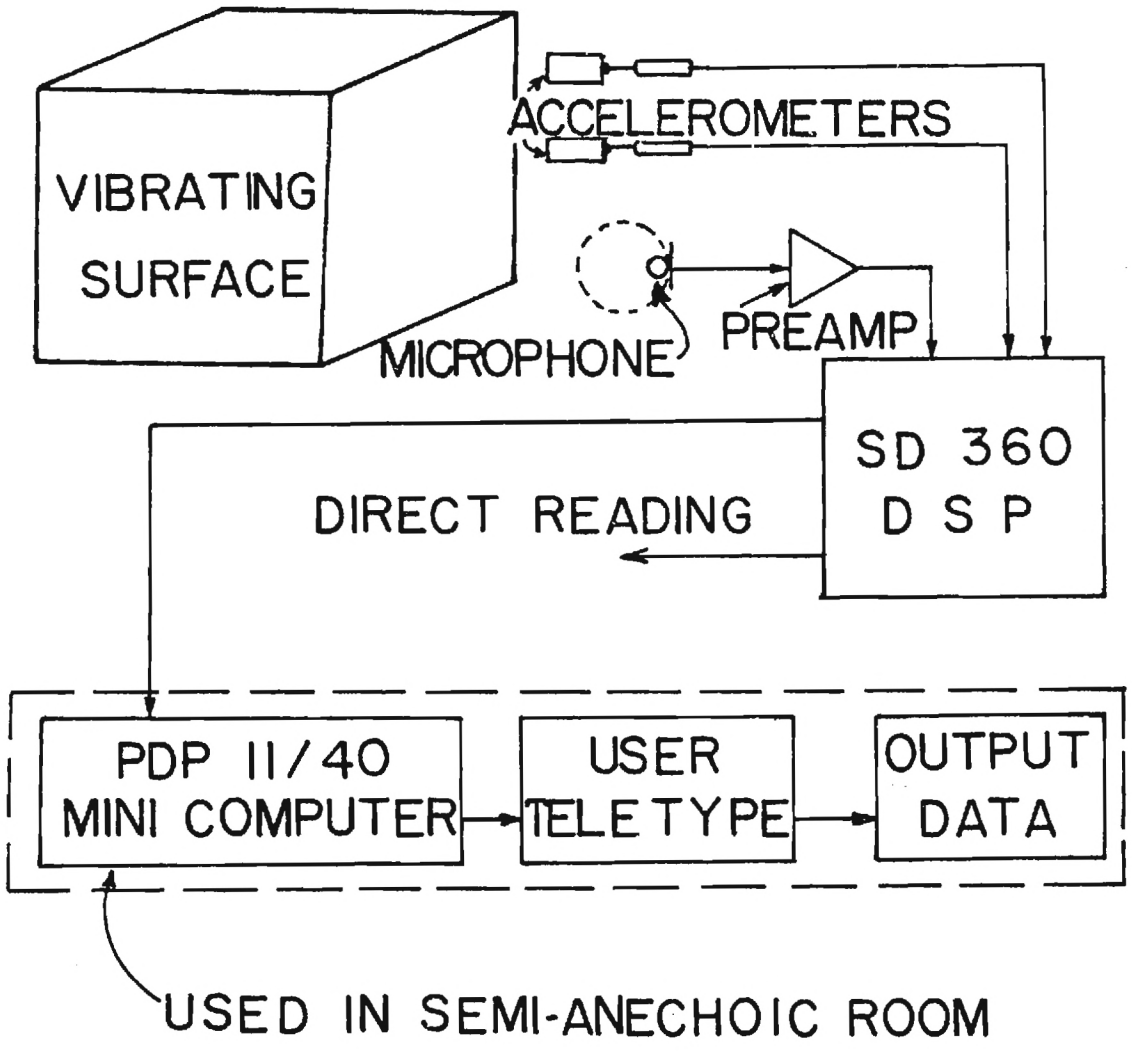

Figure 5-3. Schematic Diagram of Experimental Arrangement

points located near the center of the front side was used as the reference point (Fig. 5-4). The rms amplitude of normal acceleration and the acceleration phase relative to this reference point were measured with two accelerometers on all the points of each of the four vertical sides of the transformer. Both accelerometers were in turn connected to a Spectral Dynamics Corporation digital signal processor (Model SD360) which gives the rms amplitude of normal acceleration in decibels and the phase in degrees (Fig. 5-3).

Far field sound radiation measurements were made with a one inch diameter General Radio ceramic microphone at radial distances of 6.1 m, 12.2 m and 24.4 m and at 22.5° angular spacing (in the counterclockwise sense) from the center of the tank and at 0.91 m above the ground. The zero degree (0°) microphone position was facing the side of the tank containing the main drain valve. The ceramic microphone was used with a General Radio preamplifier so as to minimize the possible error in the sound pressure level measurement due to the length of the cable between the microphone and the signal processing instrumentation set-up.

The second application consists of a similar near field experiment which was conducted for a production-line transformer. This transformer had been used only for experimental purposes. This was a 19.5 MVA transformer with 2.95 m x 1.52 m x 3.89 m in dimensions. The experiment was conducted inside a 15.24 m x 13.72 m x 10.06 m semi-anechoic room at

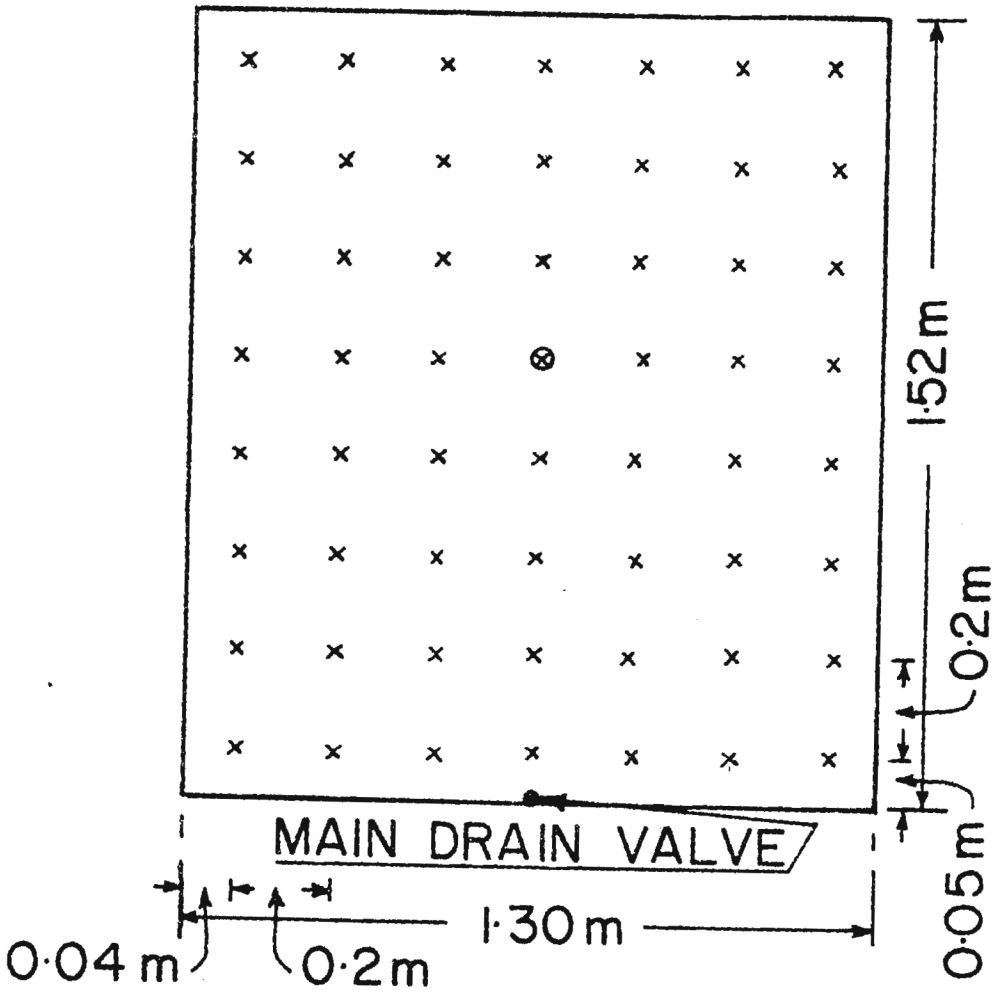

Figure 5-4. Sketch of Acceleration Measurement Points on a Typical Vibrating Surface
⊗ Reference Point

the transformer manufacturing plant. On the front side of the tank 63 points with 9 rows and 7 columns and on the back side 77 points with 11 rows and 7 columns were located at almost equal intervals. On the other two sides, 55 points with 11 rows and 5 columns were marked at fairly uniform spacing. The transformer was allowed to run at full load before the surface acceleration measurements were made for various frequency components. These included 120 Hz fundamental and its multiples up to 720 Hz. The choice of the harmonics were not arbitrary. As indicated by the spectra recorded on the digital signal processor, the acceleration amplitudes at these frequencies were at least 10 dB above the background levels. Due to the space limitation in the semi-anechoic room, far-field sound pressure levels could not be measured for the production-line transformer.

The far-field prediction scheme described above along with the double-edge diffraction contribution was next applied to compare its numerically computed results with another set of analytical and experimental results independently obtained by Hutchins and Kouyoumjian [39]. Although Hutchins and Kouyoumjian have used geometrical theory of diffraction in the prediction of the far-field radiation pattern of a baffled array mounted on a rectangular rigid box, they do not discuss about Fresnel integrals or Fresnel functions. Instead, a more restricted form of the edge diffraction coefficient has been used to compute the diffracted rays. This diffraction

coefficient obtained from the laws of diffraction has a singularity in the neighborhood of the boundary of the shadow where the ray fields vary rapidly with the angular coordinates. In order to obtain a nonsingular expression of the diffraction coefficient at this region, the restricted form of the edge diffraction coefficient has been multiplied by a semi-convergent transition-region correction factor. The correction factor was obtained earlier by Pauli [41] based on a restricted form of uniform asymptotic solution where the asymptotic series converges only on a part of the path of integration. The correction factor thus obtained though manages to be regular in the boundary of the region separating the illuminated region from the shadow, fails to be regular near other boundaries between the various regions. The experimental results were obtained from a baffle structure consisted of a heavy aluminum block [39,19] (0.62 m x 0.14 m x 0.15 m in size) with an array of 1-by-12 rectangular pistons (0.05 m x 0.05 m transducer elements) flush mounted on one of the major faces of the baffle (Fig. 5-5). The array which was operating in a receiving mode was excited at a pure-tone frequency of 2500 Hz. All the pistons were uniformly vibrating in phase to produce a maximum pressure at points facing the center of the array of piston. Sound pressure level measurements were made in the air all around the baffle at a radial distance of 5.50 m away from the center of the array of piston where $\theta = 0°$ corresponds to the point facing the piston.

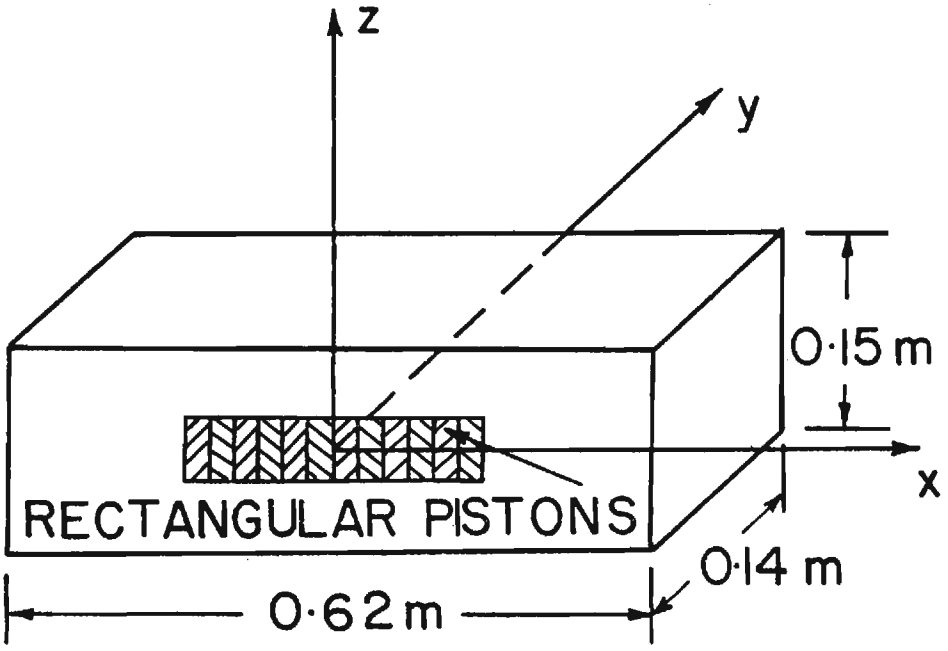

Figure 5-5. Sketch of a Linear Array of Rectangular Pistons Flush Mounted on One of the Faces of the Baffle

The present technique with some modification was finally compared with another set of numerical and experimental results obtained by Furue et al. [40]. Approximate estimate of the diffraction effects has been obtained by Furue et al. by the application of the surface integral equation methods over three-dimensional thin noise barriers. The noise barriers were considered as degenerated closed surface one of whose faces was thought to be acoustically illuminated and the other was considered dark. The effect of velocity potential on the shadow surfaces was therefore neglected in the diffraction effects computation. The experiment was performed on a box-like structure (Fig. 5-6) which simulated a thin rigid noise barrier type enclosure. The box was 0.3 m in width, 0.2 m in depth and 0.15 m in height with an open top. A point noise source (loudspeaker with circular pipe) which was excited at a pure-tone frequency of 2500 Hz was located at the center of the box. Receiving points were taken all around the box at a radial distance of 0.8 m away from the source and at an angular spacing of 5° along the xz and yz plane. The computation of the diffraction effects according to the present prediction scheme includes the contributions from the waves directly coming from the source, the waves reflected from the inner surfaces of the thin box and the waves diffracted from the different edges of the box. The diffracted waves include contributions from both the single-edge and the double-edge diffraction terms in the shadow zone.

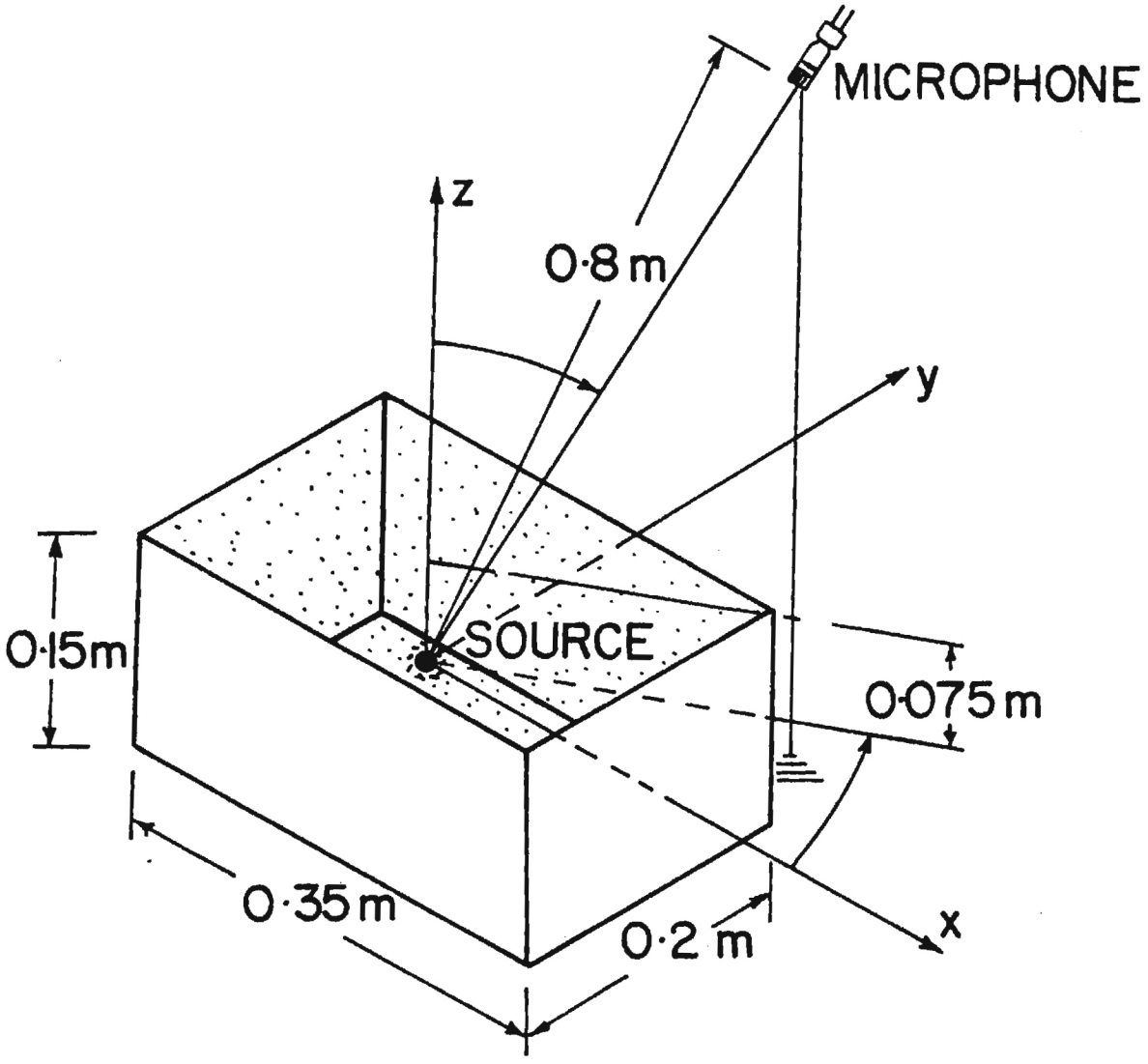

Figure 5-6. Sketch of Source-Listener-Thin Box Like Noise Barrier Configuration

CHAPTER VI

COMPARISON OF THEORETICAL AND EXPERIMENTAL RESULTS

The theoretically calculated patterns of the far-field sound radiation, based on equation (3.25), for the simulated transformer are compared with the measured far-field sound pressure levels. The plots of these comparisons around the tank at radial distances of 6.1 m, 12.2 m and 24.4 m from the center of the tank and at 0.91 m above the ground are shown in Figs. 6-1 through 6-3. Considering the fact that the outdoor experiments were performed under less than ideal circumstances (wind, atmospheric turbulence, irregular ground of finite acoustic impedance, low signal-to-noise ratio due to irregular background noise), the agreement between the theoretically calculated values and the measured sound pressure levels are considered to be a substantial verification of the theory. Reason for the noticeable discrepancy between the theoretical analyses and the experimental results at 225°, 247.5° and 270° is believed to be partially because of the presence of few obstacles (the instrumentation set-up) in that region (Fig. 5-2).

The results of theoretical calculations based on the surface acceleration measurements of the 19.5 MVA electric transformer are shown in Figs. 6-4 through 6-9. These figures describe the entire far-field radiation patterns around the

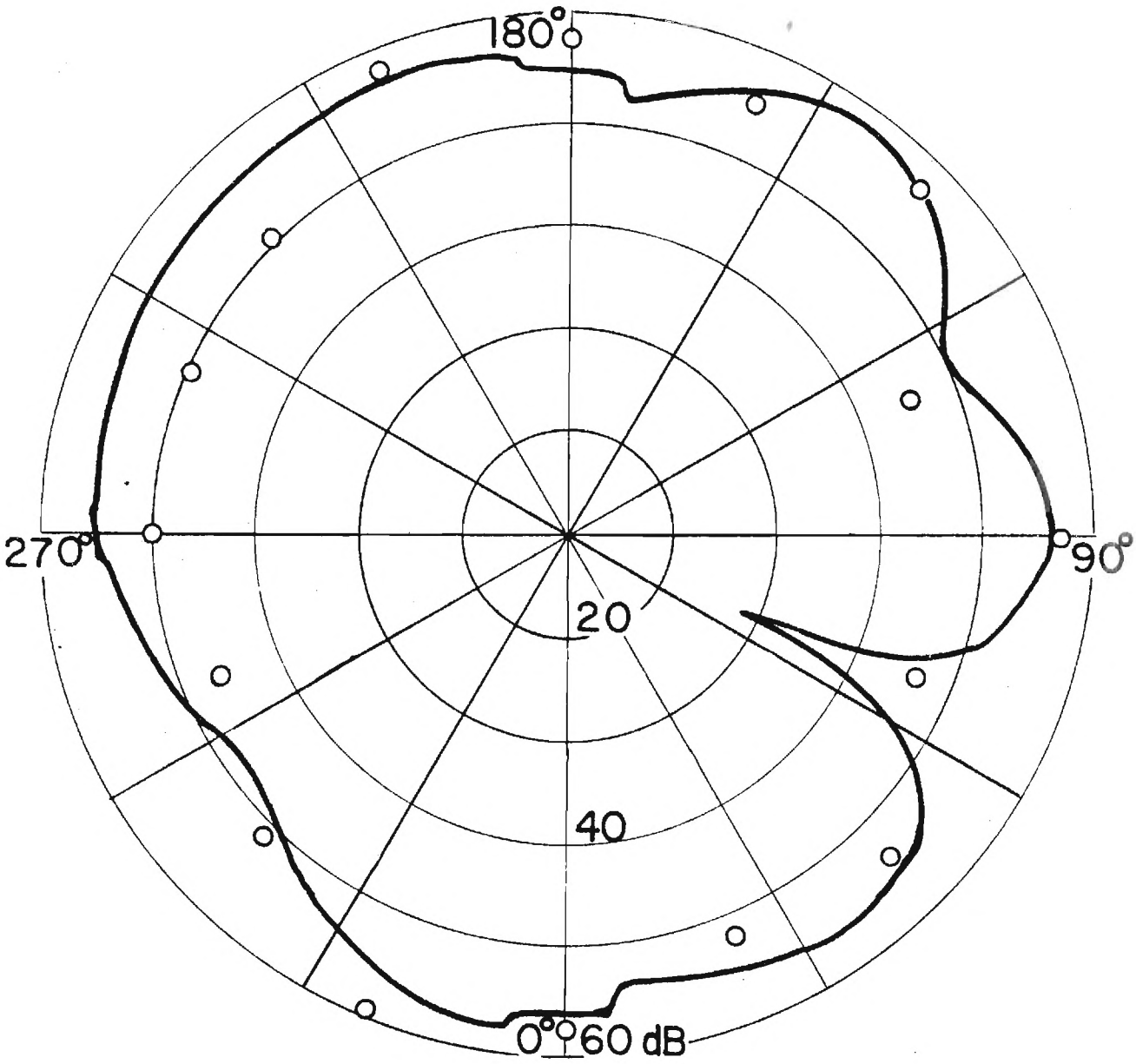

Figure 6-1. Sound Radiation Pattern for a Simulated Transformer. Frequency 265 Hz; 6.1 m from the Center of the Transformer and 0.91 m above the Ground.

——Theoretically Computed Results
o Experimental Results

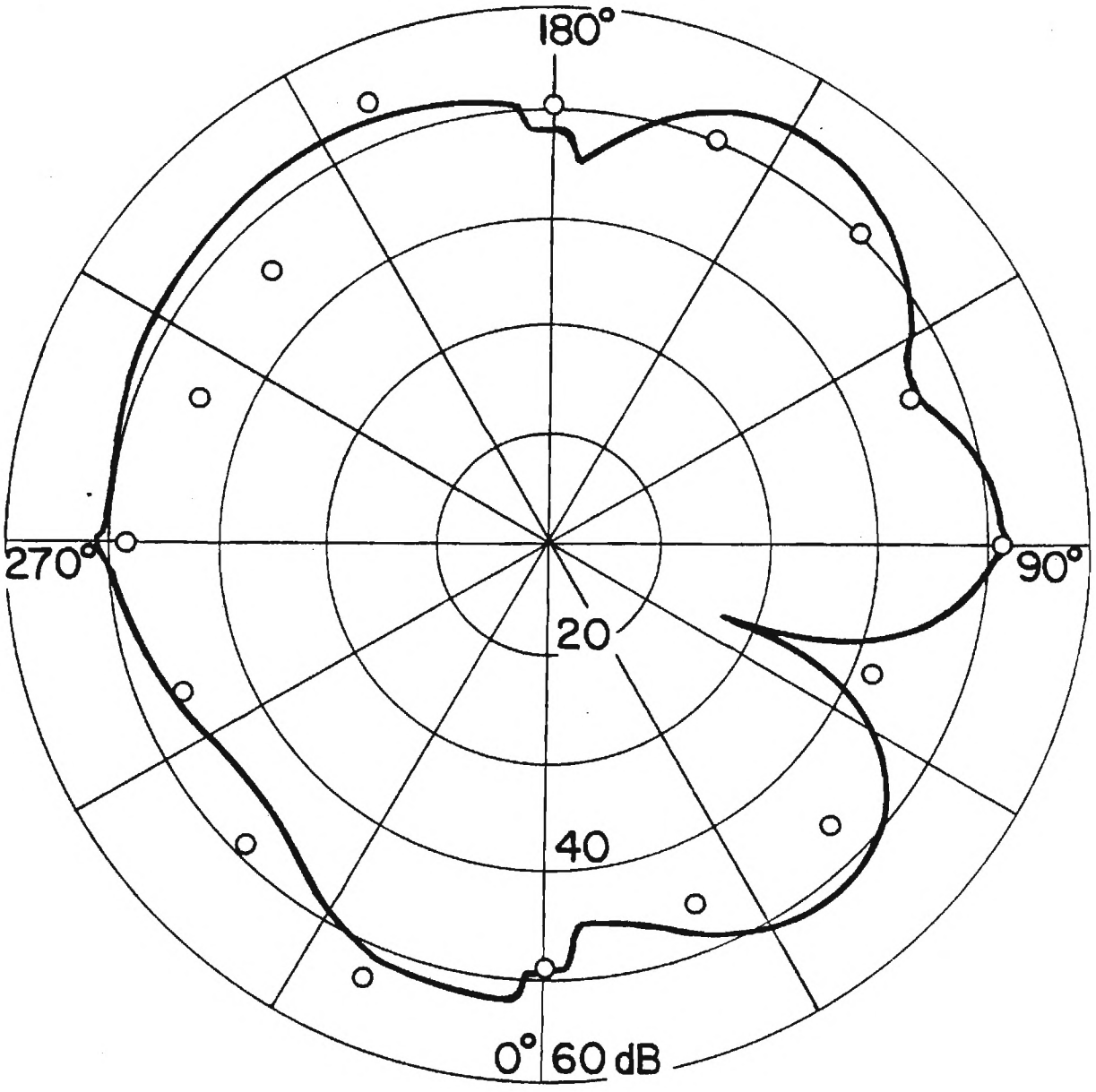

Figure 6-2. Sound Radiation Pattern for a Simulated Transformer. Frequency 265 Hz; 12.2 m from the Center of the Transformer and 0.91 m above the Ground.

——Theoretically Computed Results
o Experimental Results

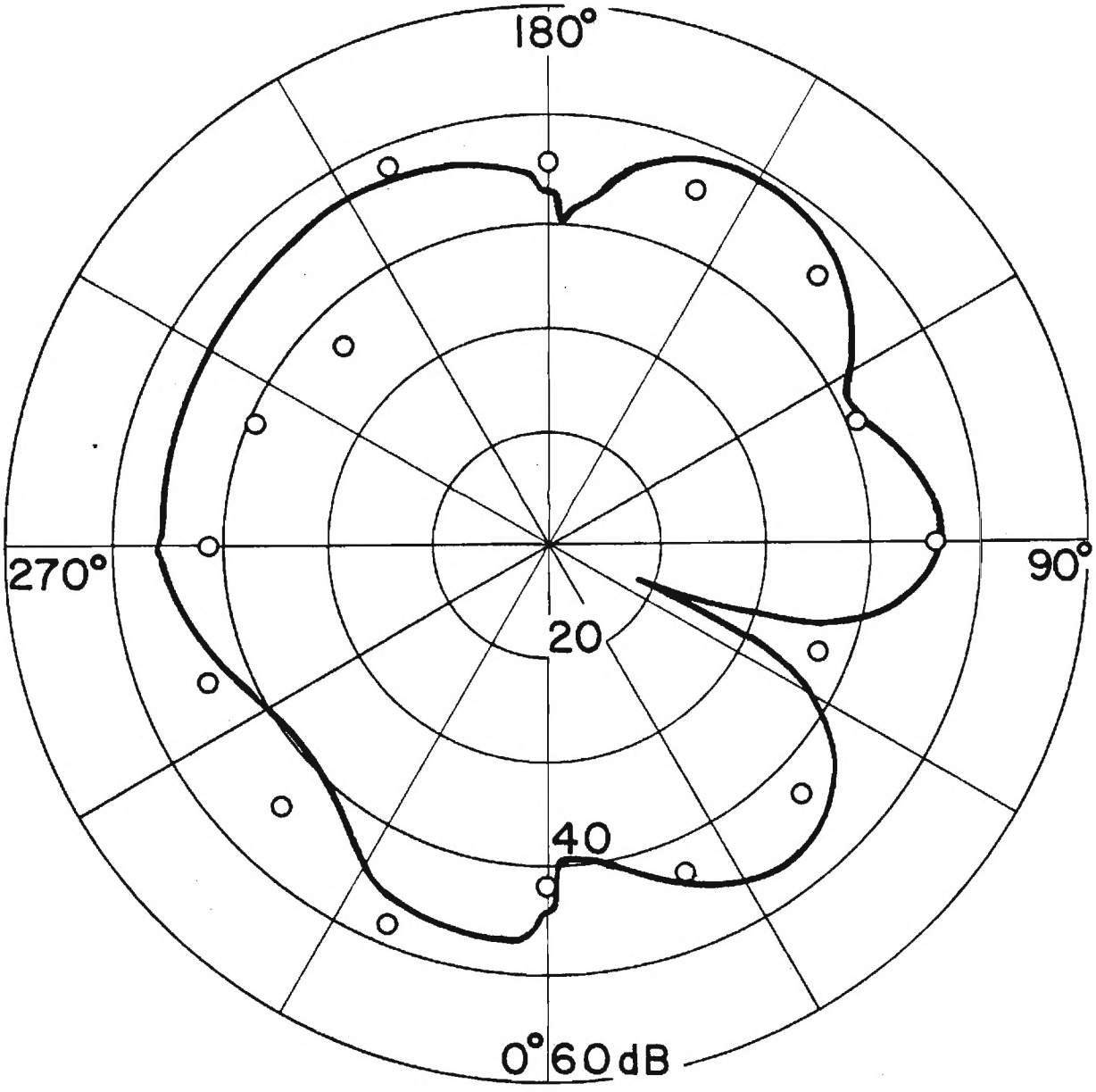

Figure 6-3. Sound Radiation Pattern for a Simulated Transformer. Frequency 265 Hz; 24.4 m from the Center of the Transformer and 0.91 m above the Ground

——Theoretically Computed Results
o Experimental Results

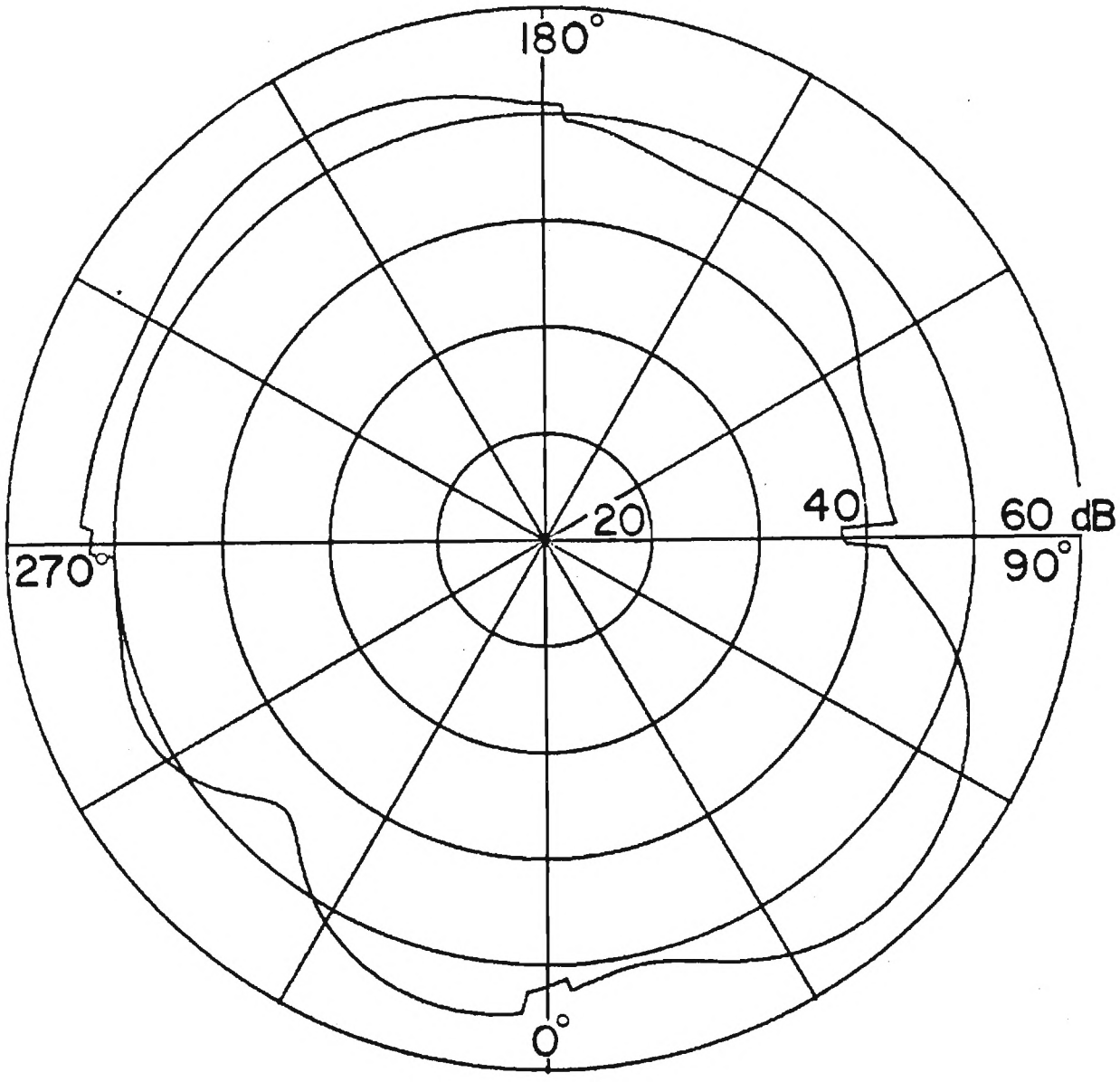

Figure 6-4. Theoretically Computed Sound Radiation Pattern for a 19.5 MVA Electric Transformer. Frequency 120 Hz; 28.8 m (10λ) from the center of the Transfer and 0.91 m above the Ground

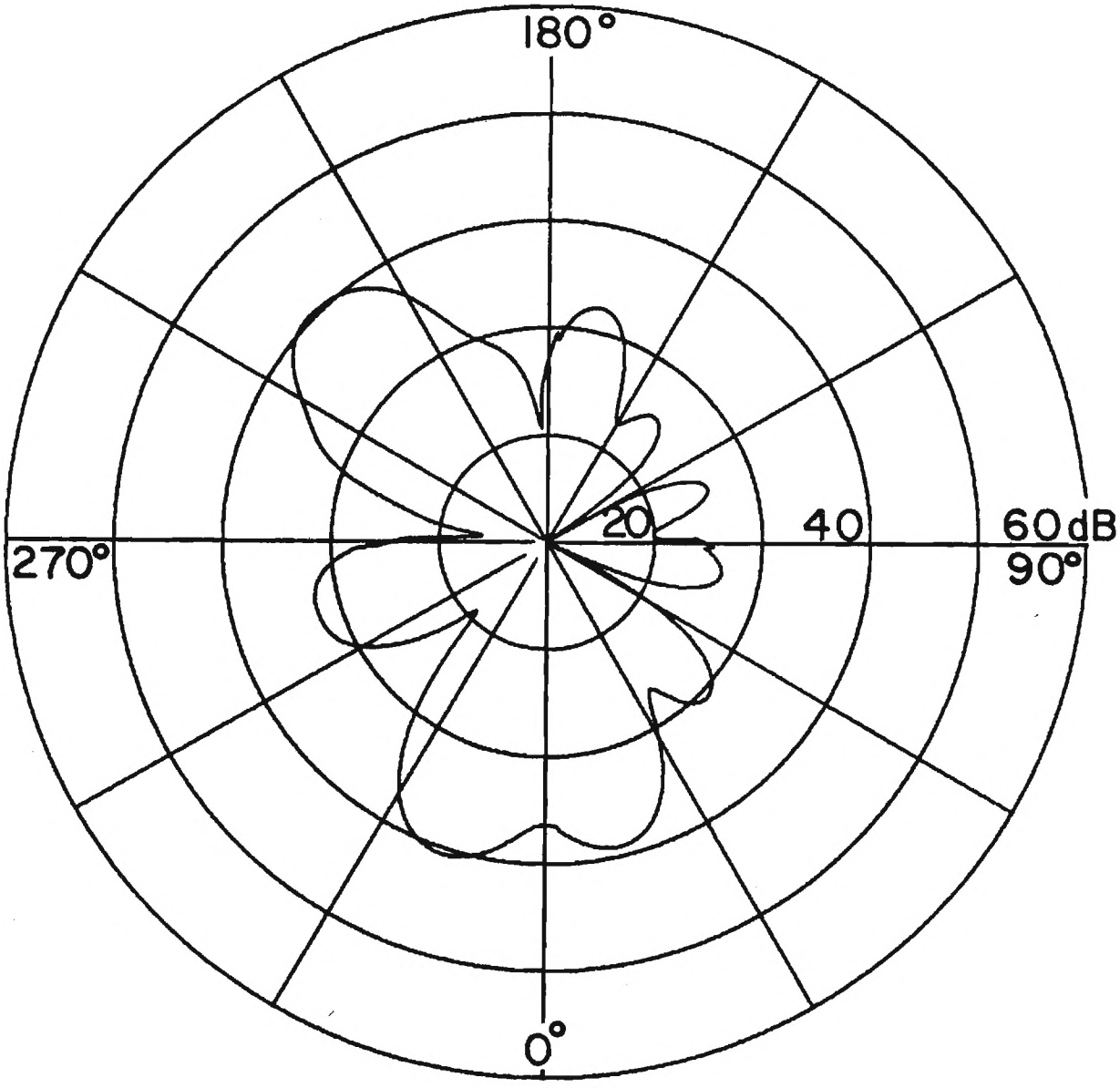

Figure 6-5. Theoretically Computed Sound Radiation Pattern for a 19.5 MVA Electric Transformer. Frequency 240 Hz; 28.8 m (20λ) from the Center of the Transformer and 0.91 m above the Ground.

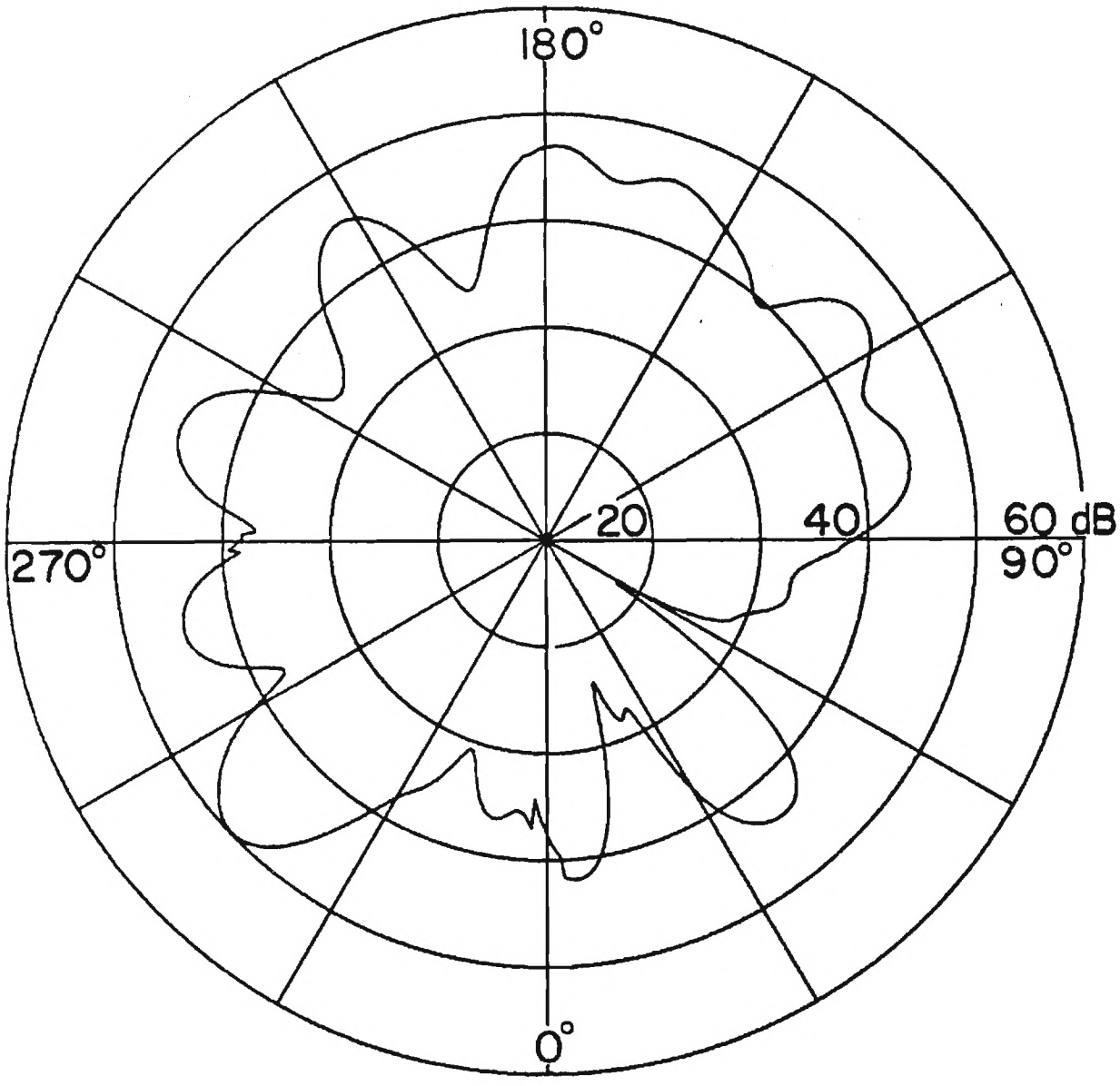

Figure 6.6. Theoretically Computed Sound Radiation Pattern for a 19.5 MVA Electric Transformer. Frequency 360 Hz; 28.8 m (30λ) from the Center of the Transformer and 0.91 m above the Ground.

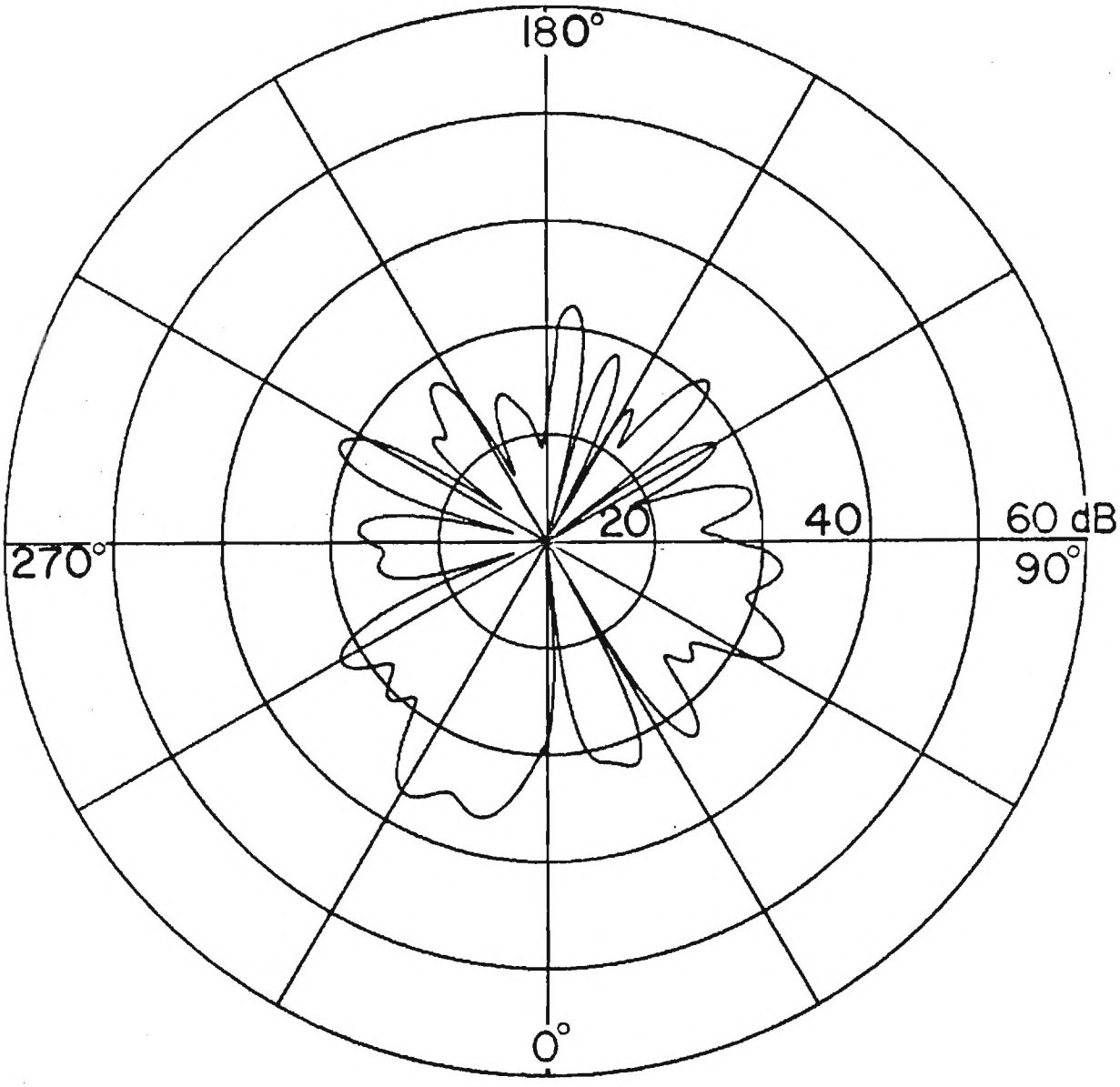

Figure 6-7. Theoretically Computed Sound Radiation Pattern for a 19.5 MVA Electric Transformer. Frequency 480 Hz; 28.8 m (40λ) from the Center of the Transformer and 0.91 m above the Ground

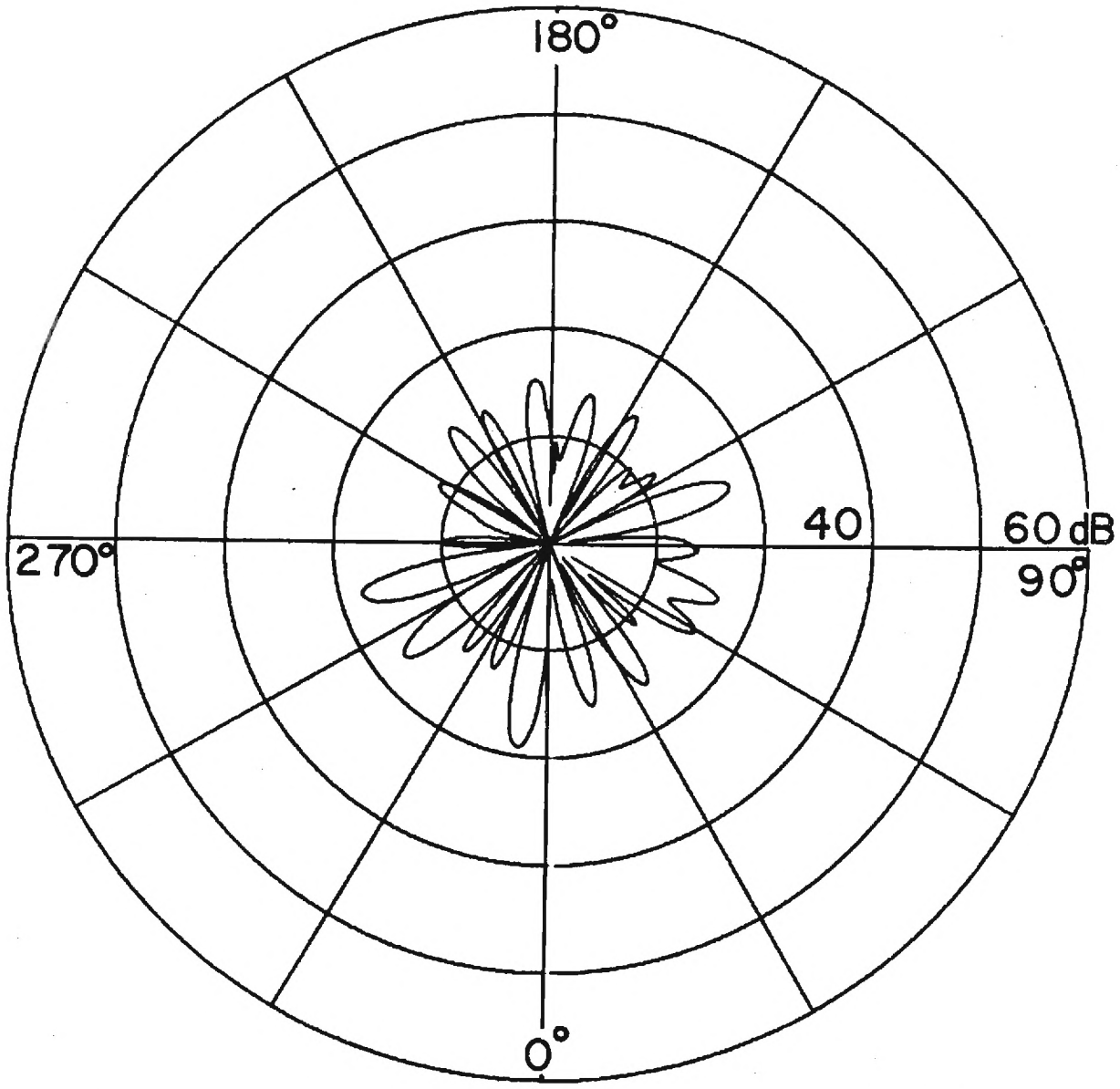

Figure 6-8. Theoretically Computed Sound Radiation Pattern for a 19.5 MVA Electric Transformer. Frequency 600 Hz; 28.8 m (50λ) from the Center of the Transformer and 0.91 m above the Ground.

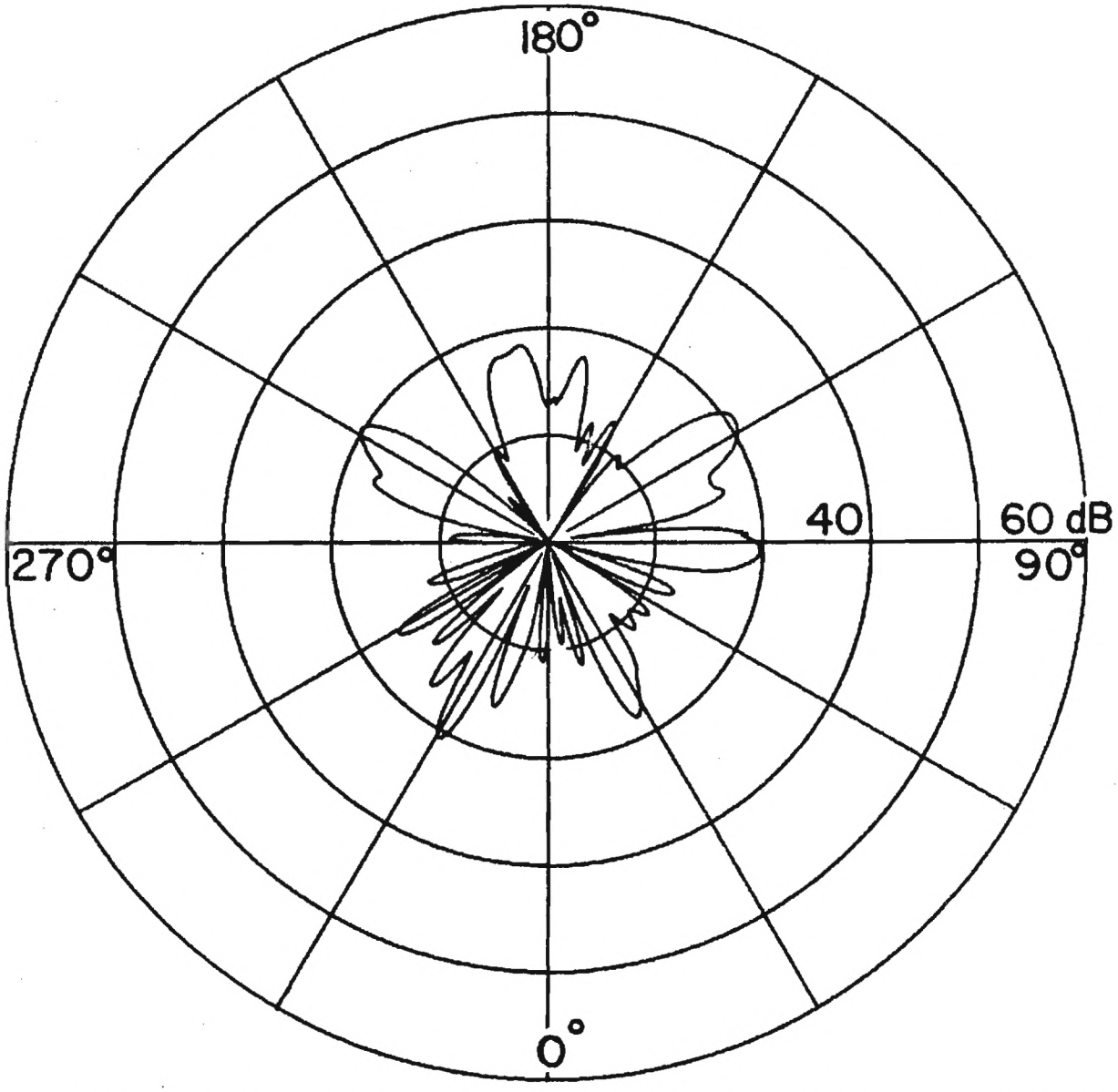

Figure 6-9. Theoretically Computed Sound Radiation Pattern for a 19.5 MVA Electric Transformer. Frequency 720 Hz; 28.8 m (60λ) from the Center of the Transformer and 0.91 m above the Ground.

transformer of frequencies ranging from 120 Hz and its multiples up to 720 Hz. These radiation patterns are in general smooth and uniform at low frequencies (120 Hz), but display the expected increase of directional variations in the sound pressure level with increasing frequency.

It is to be noted that the effects of neglecting the higher order diffraction terms in the theoretical computation are noticeable at low frequency analyses in terms of finite discontinuity at the shadow boundary. These discontinuities are just the same as the omission of single-edge diffraction terms at the shadow boundary for directly transmitted waves would lead to a discontinuity as the listener passed from the illuminated region into the shadow. Also, the idealization of the ground surface by a rigid plane has given a conservative estimate of the sound levels shown in Figs. 6-1 through 6-9.

Computations of the sound pressure level distribution for the rectangular pistons in a rectangular baffle result in good agreement with Hutchins-Kouyoumjians experimental and analytical values [39]. The only exception of this agreement is at a region directly behind the baffle. The inclusion of double-edge diffracted wave contribution leads to the distribution presented in Fig. 6-10. This is virtually identical to the analytical results presented by Hutchins and Kouyoumjian. This agreement also reconfirms the validity and the wide applicability of the present theory.

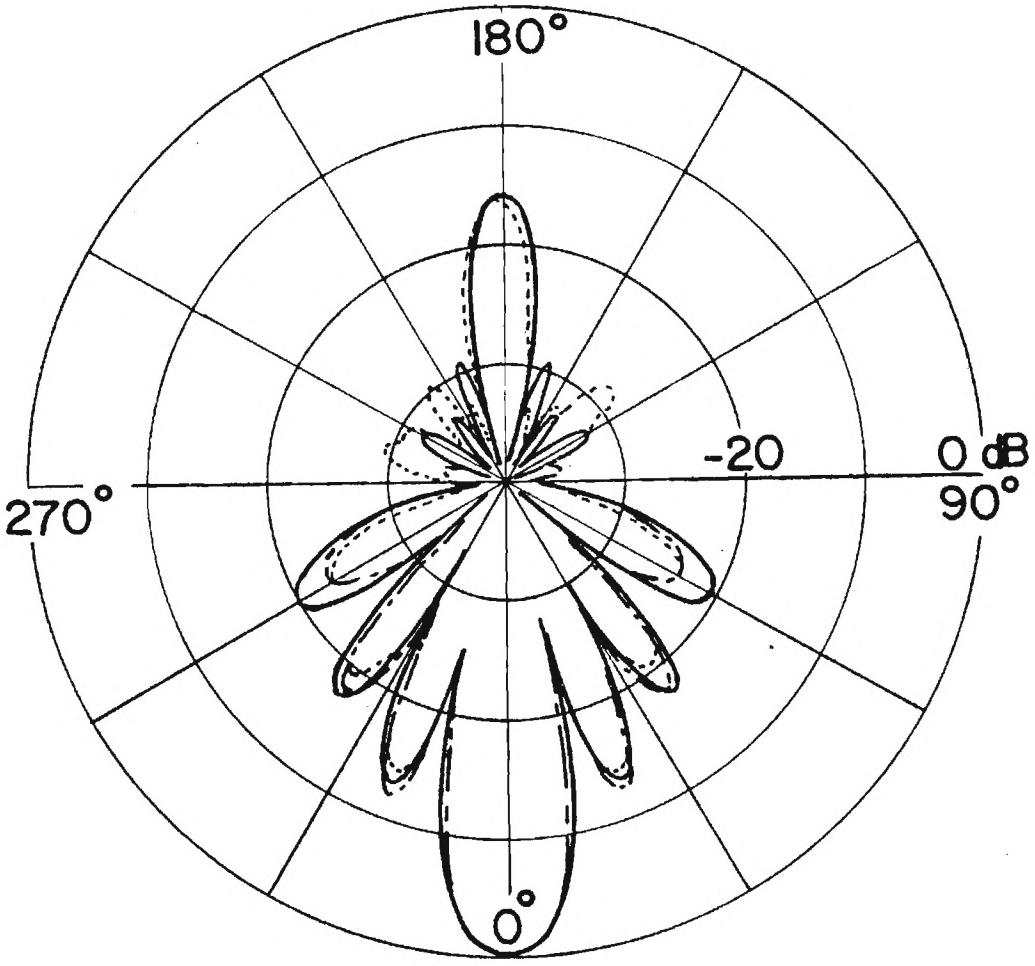

Figure 6-10. Sound Radiation Pattern of a Linear Array of Pistons Flush Mounted on a Rigid Baffle. Frequency 2500 Hz; 5.5 m from the Center of the Array of Pistons.

——Application of the Present Prediction Scheme
—.—Application of Hutchins-Kouyoumjian Prediction Scheme [39]
---Experimental Result of Hutchins and Kouyoumjian [39]

Figures 6-11 and 6-12 show the comparison of the diffraction effects between the present theory and the experiments conducted by Furue et al. [40] on a box-like barrier. The agreement is reasonably well for all the microphone locations. Slight variations between the calculated and the measured values at the wide angles are believed to arise from the complete omission of the sound transmission through the box-like barrier (none of the barriers are perfectly rigid in the actual case) in the theoretical analysis. It is to be noted that the application of Furue et al.'s theoretical analysis agreed very poorly with the experimental results at large angles, i.e., in the shadow region. The reason for this discrepancy is explained as the effect of neglecting the velocity potential at the shadow surfaces.

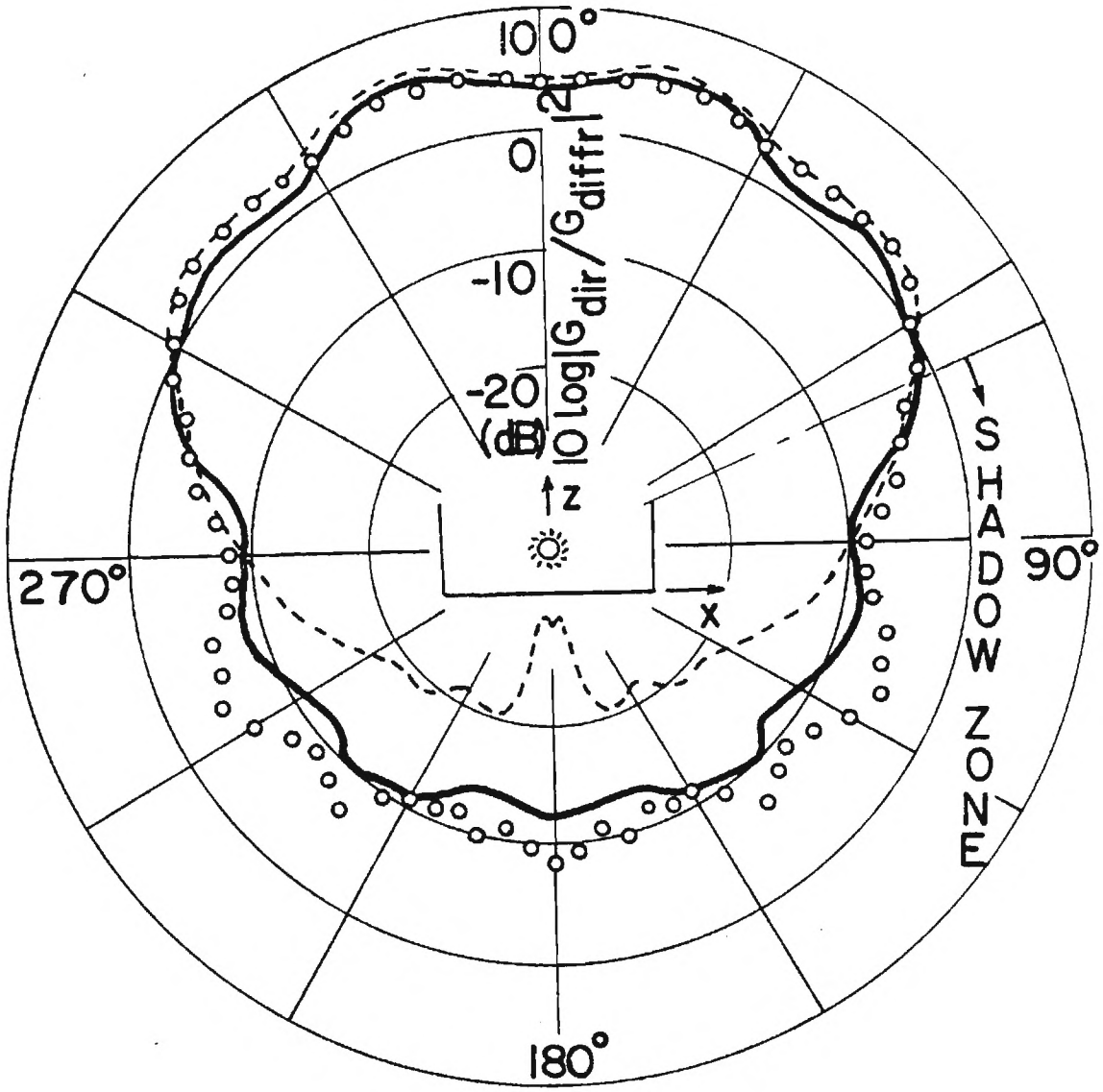

Figure 6-11. Diffraction Effects by a Box-Like Barrier in the x-z Plane. Frequency 2500 Hz; 0.08 m from the Center of the Barrier.

——Application of Present Prediction Scheme
---Application of Furue et al. Prediction Scheme [40]
o Experimental Result of Furue et al. [40]

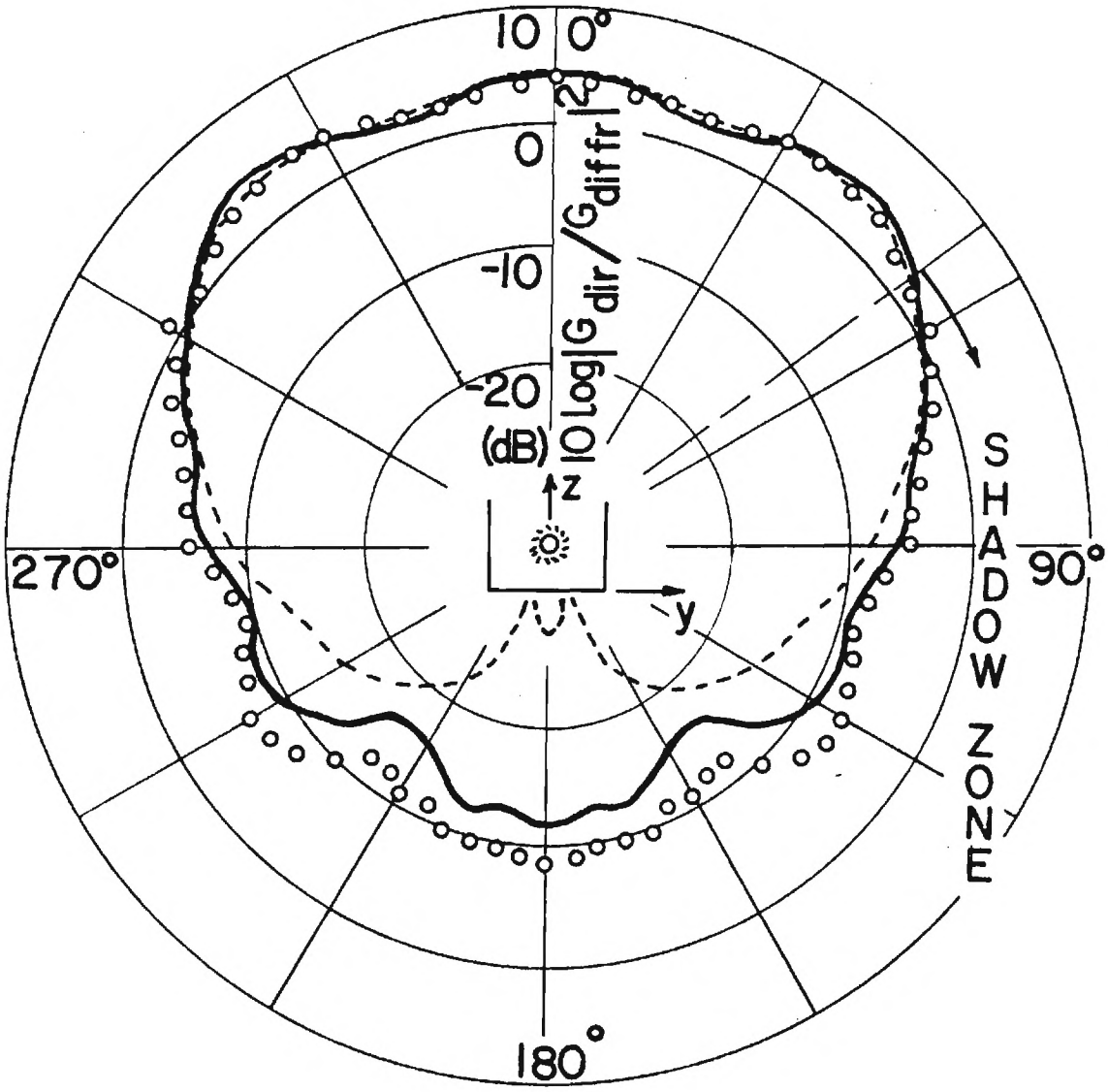

Figure 6-12. Diffraction Effects by a Box-Like Barrier in the y-z Plane. Frequency 2500 Hz; 0.8 m from the Center of the Barrier

——Application of Present Prediction Scheme
---Application of Furue et al. Prediction Scheme [40]
o Experimental Result of Furue et al. [40]

CHAPTER VII

DISCUSSION OF SOUND RADIATION PREDICTION SCHEMES

Critique of the CHIEF Algorithm

Several well-developed theories and numerical techniques dealing with integral solutions of radiation problems are used extensively in the analysis of underwater sound propagation. These techniques are also applicable, at least in theory, for predicting the sound radiation from electric transformers resting on ground. With this idea in mind, one of the improved methods based on Combined Helmholtz Integral Equation Formulation (CHIEF) algorithm developed by Schenck [19] was initially used as a possible transformer noise prediction scheme. Eight points, each at the center of an octant of the modified tank, were considered as the strategic interior points in over-determining the system of algebric equations to obtain a good correlation between the theory and the experiment. Unfortunately, the theoretically predicted sound pressure levels based on the method CHIEF with one interior point per octant did not compare well [42] with the results obtained from the conducted experiments (Table 7-1). This method cannot be relied upon to give consistently good results as Schenck does not give any procedure to satisfy the indispensable requirements, the selection of the optimum number of interior

Table 7-1. Measured and Predicted (CHIEF) Sound Power Level

Distance from the center of the tank in m		θ in degree							
		0	45	90	135	180	225	270	315
6.1	Measured SPL	57.3	53.3	57.0	56.6	57.4	49.9	49.5	51.0
	Predicted SPL as per CHIEF	50.6	51.0	59.3	61.0	47.3	52.3	62.3	62.3
12.2	Measured SPL	49.6	47.1	51.9	50.8	50.8	45.8	48.8	48.9
	Predicted SPL as per CHIEF	49.1	47.2	52.2	53.0	45.9	50.4	55.5	53.0
24.4	Measured SPL	42.5	42.7	45.9	45.0	45.8	36.2	41.3	45.1
	Predicted SPL as per CHIEF	27.3	36.4	50.1	52.1	40.8	42.6	54.0	52.8

points and their locations, for this approach. However, this difficulty has been overcome by Jones [23] where he gives a definite method for the number of side conditions that must be imposed to obtain consistently good results for a given value of frequency. Besides, the requirement that the mesh spacing has to be sufficiently small to assume constant surface acceleration in each area element of the vibrating surface could neither be satisfied during the tests performed in the General Electric's test field site, nor be handled because of the large computing time and means needed for its implementation (i.e., solving overdetermined system of algebric equations).

Sensitivity of Far-Field Predictions to the Size of Data Mesh

Due to the limitations of the applicability of the CHIEF algorithm, it was next attempted to develop a better model of transformer surface vibrations in order to make accurate far-field predictions. It is envisioned that given node lines, or, at least approximate node lines, one can represent the tank wall vibration by an acceleration amplitude function which vanishes on node lines and has undetermined amplitudes at the center of node cells. Figure 7-1 shows the vibration distribution of a typical transformer surface due to the excitation of underwater speakers. The regions containing the positive signs in the figure vibrate in the

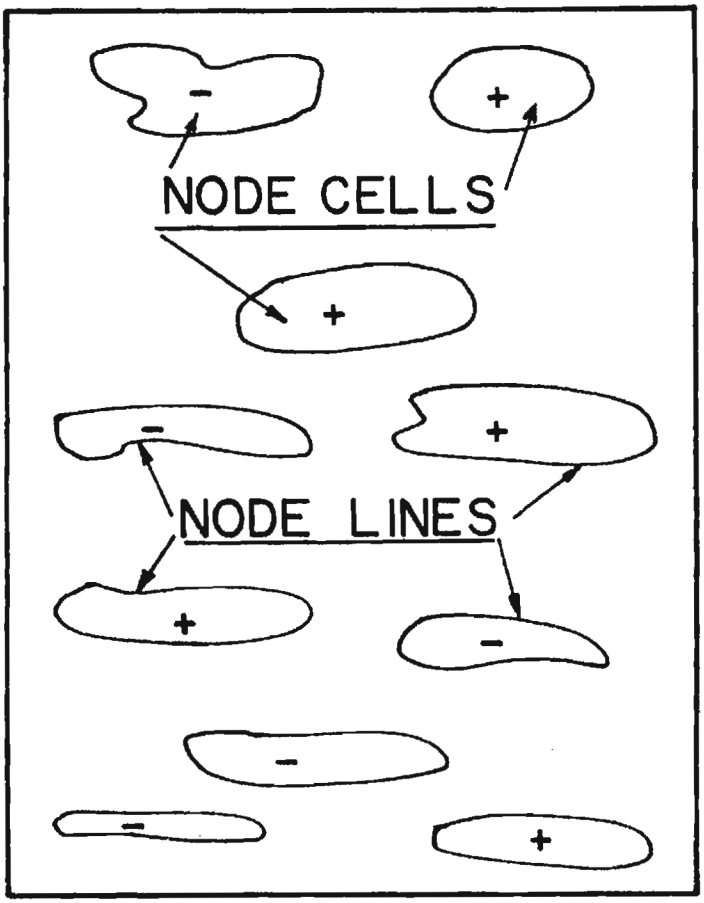

Figure 7-1. Sketch of Vibration Distribution of a Typical Surface

opposite sense as that of the regions containing the negative signs with reference to the mean position of the tank surface. The idea of developing an analytic function to represent the tank vibration did not come true because the node lines could not be determined from the available phase informations of the limited surface acceleration data.

Attempts were also made to improve the existing model of the vibrating tank by acquiring more near-field informations, i.e., surface acceleration data, at regions of sparse observations and in between gaps of the existing data. In addition to several existing linear interpolation schemes available in the handbook [37], two other techniques (12 point formula and 24 point formula) were developed to generate more surface acceleration data. The developments were based on the equally spaced data points and the method of undetermined coefficients. Let the expression

$$a_n(0,0) = a_n(x,y) - (k_1x + k_2y + k_3x^2 + k_4xy + k_5y^2)$$

or, conveniently,

$$a_n(x,y) = a_n(0,0) + k_1x + k_2y + k_3x^2 + k_4xy + k_5y^2 \quad (7.1)$$

relates the interpolated data with each of the given surface acceleration data at the corresponding data points (Fig. 7-2). The parameters k_1, k_2, k_3, k_4 and k_5 are the constants needed

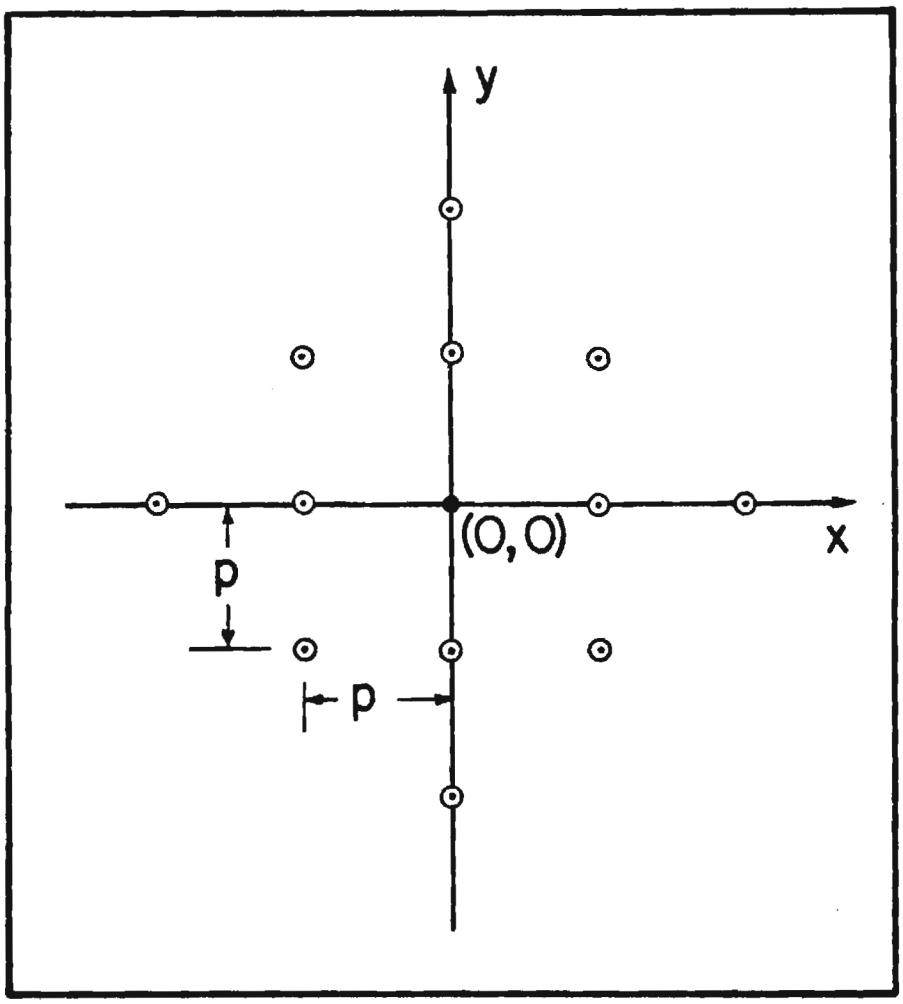

Figure 7-2. Sketch of Acceleration Data Points for 12 Point Formula Interpolation Scheme

for the best fit of the curve in order to relate $a_n(0,0)$ with $a_n(x,y)$. The circled dots in Fig. 7-2 designate the coordinates of the given data points whereas the dot represents the location of the point where the surface acceleration needs to be interpolated. Substituting the coordinates of each of the data points in the above equation and then performing some simple arithmatic, one gets

$$a_n(p,0) + a_n(-p,0) + a_n(0,-p) + a_n(0,p) = 4a_n(0,0) + 2(k_3+k_5) \tag{7.2a}$$

$$a_n(2p,0) + a_n(-2p,0) + a_n(0,-2p) + a_n(0,2p) = 4a_n(0,0) + 8(k_3+k_5) \tag{7.2b}$$

$$a_n(p,p) + a_n(-p,-p) + a_n(p,-p) + a_n(-p,p) = 4a_n(0,0) + 4(k_3+k_5) \tag{7.2c}$$

where p is the spacing between two consecutive data points. Let the three successive left hand sides of equation (7.2a) through (7.2c) be denoted by α_1, β_1 and γ_1. Then one should have

$$2\alpha_1+\beta_1-3\gamma_1 = 0 \tag{7.3}$$

and $a_n(0,0)$ can be calculated from

$$a_n(0,0) = \frac{\gamma_1}{2} - \frac{\beta_1}{4} + \mu(2\alpha_1+\beta_1-3\gamma_1) \qquad (7.4)$$

where μ is arbitrary. One would like to choose μ such that were there any error in the given data at the circled dots the error in the interpolated data $a_n(0,0)$ would be a minimum. In order to obtain this, one expresses the error $(\delta a_n(0,0))$ in the interpolated data as

$$<|\delta a_n(0,0)|^2> = [\partial a_n(0,0)/\partial\alpha_1]^2<|\delta\alpha_1|^2>$$

$$+ [\partial a_n(0,0)/\partial\beta_1]^2<|\delta\beta_1|^2> + [\partial a_n(0,0)/\partial\gamma_1]^2<|\delta\gamma_1|^2> \qquad (7.5)$$

and sets

$$\partial<|\delta a_n(0,0)|^2>/\partial\mu = 0$$

with the assumption that one possibly make errors $(\delta\alpha_1\delta\beta_1,\delta\gamma_1)$ in the same range while measuring surface accelerations, i.e.,

$$<|\delta\alpha_1|^2> \simeq <|\delta\beta_1|^2> \simeq <|\delta\gamma_1|^2>.$$

The derivation sketched above, equation (7.2) through (7.5), leads to the result $\mu = \frac{1}{8}$ and the best formula for $a_n(0,0)$ is

$$a_n(0,0) = \frac{1}{4}\,[a_n(p,0) + a_n(-p,0) + a_n(0,-p) + a_n(0,p)]$$

$$- \frac{1}{8}\,[a_n(2p,0) + a_n(-2p,0) + a_n(0,-2p) + a_n(0,2p)]$$

$$+ \frac{1}{8}\,[a_n(p,p) + a_n(-p,-p) + a_n(p,-p) + a_n(-p,p)]. \qquad (7.6)$$

The general formula for the interpolated data at (x,y) can be expressed as

$$a_n(x,y) = \frac{1}{4}\,[a_n(x+p,y) + a_n(x-p,y) + a_n(x,y-p) + a_n(x,y+p)$$

$$- \frac{1}{8}\,[a_n(x+2p,y) + a_n(x-2p,y) + a_n(x,y-2p) + a_n(x,y+2p)$$

$$+ \frac{1}{8}\,[a_n(x+p,y+p) + a_n(x-p,y-p) + a_n(x+p,y-p) + a_n(x-p,y+p)]. \qquad (7.7)$$

Accordingly, the general formula for the 24 point method (Fig. 7-3) is given by

$$a_n(x,y) = \frac{1}{228}\,[82\{a_n(x+p,y) + a_n(x,y+p) + a_n(x-p,y) + a_n(x,y-p)\}$$

$$+ 32\{a_n(x+2p,y) + a_n(x,y+2p) + a_n(x-2p,y) + a_n(x,y-2p)\}$$

$$- 8\{a_n(x+p,y+p) + a_n(x-p,y+p) + a_n(x-p,y-p) + a_n(x+p,y-p)\}$$

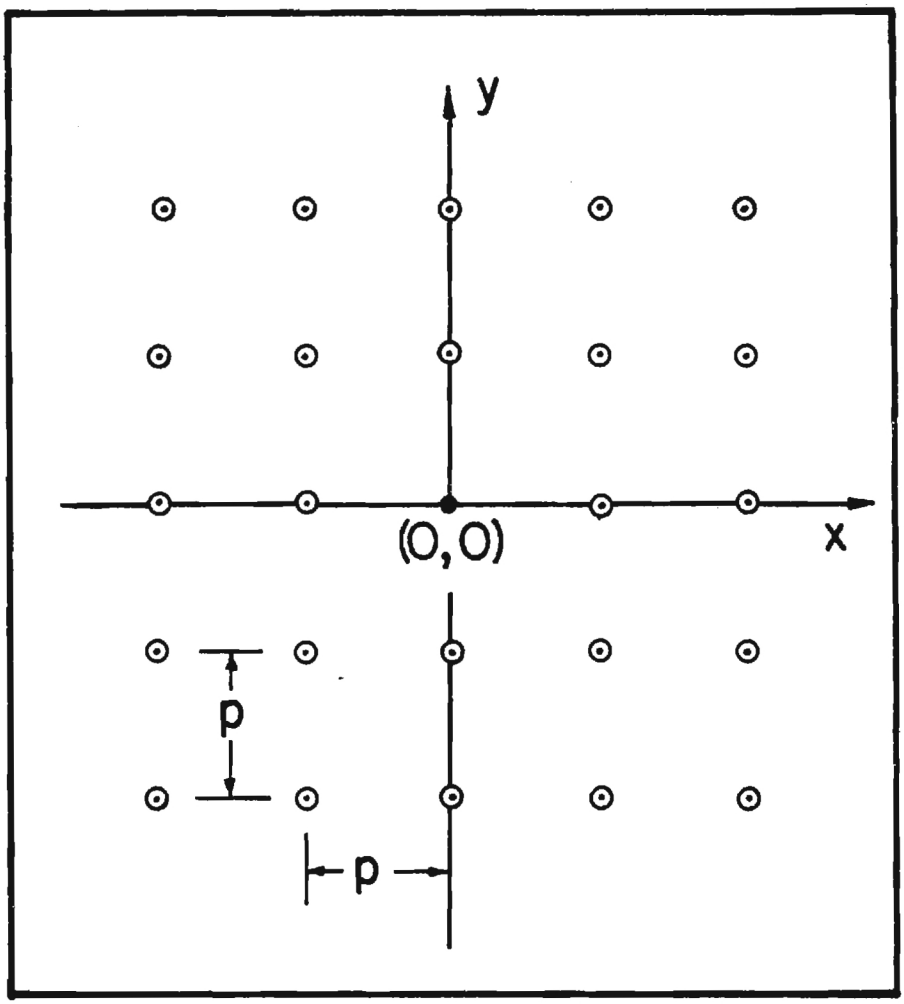

Figure 7-3. Sketch of Acceleration Data Points for 24 Point Formula Interpolation Scheme

$$- 33\{a_n(x+2p,y+p) + a_n(x+p,y+2p) + a_n(x-p,y+2p) + a_n(x-2p,y+p)$$

$$+ a_n(x-2p,y-p) + a_n(x-p,y+2p) + a_n(x+p,y-2p) + a_n(x+2p,y-p)\}$$

$$+ 17\{a_n(x+2p,y+2p) + a_n(x-2p+y+2p) + a_n(x-2p,y-2p)$$

$$+ an(x+2p,y-2p)\}] \; . \qquad (7.8)$$

The interpolation scheme was first applied to a point for which the surface acceleration was known. An error analysis was then carried out to compare the interpolated value with the known data. The relative error for the computed data is given by

$$E_{R_j} = \frac{[<|\Delta a_{n_j}|^2>dS_{o_j}^2]^{1/2}}{|\sum_{j=1}^{N} a_{n_j} \, dS_{o_j}|} \qquad (7.9)$$

which gives information about the acceleration distribution over the surface and hence about the applicability of the interpolation scheme. Here a_{n_j} is the measured acceleration at j, Δa_{n_j} is the acceleration error at point j, and dS_{o_j} is the surface area of the element j. The computation of the error analysis for different data points, shown in Table 7.2, indicates that the error is too large, i.e., the surface acceleration distribution is very scattered to use any

Table 7-2. Error Estimate of Typical Interpolation Data Based on 12 Point Formula and 24 Point Formula

Measured a_{n_j}	Estimated a_{n_j} for 12 Pt. Formula	Δa_{n_j} for 12 Pt. Formula	Estimated a_{n_j} for 24 Pt. Formula	Δa_{n_j} for 24 Pt. Formula	E_R for 12 Pt. Formula	E_R for 24 Pt. Formula
-1.68 + i .31	.82 - i .27	2.50 - i .59	2.14 - i .64	3.82 - i .95	1.5	2.3
- .25 - i .41	.77 - i .06	1.03 + i .35	-1.39 + i .59	-1.14 + i 1.00	2.2	3.1
2.28 + i .02	-.36 - i .01	2.64 - i .03	.45 - i .02	-1.83 - i .04	1.1	0.8
- .01 - i 1.65	-.02 + i .94	- .01 + i 2.59	.23 + i .27	.24 + i 1.90	1.6	1.2
- .37 + i .02	-.01 + i .05	.37 + i .03	.28 - i .61	.65 - i .63	0.9	2.4
3.15 + i 0.00	.03 - i .08	-3.12 + i .08	- .82 i .01	-3.97 + i .01	1.0	1.3

interpolation scheme. The interpolation scheme appears to be highly sensitive to small errors due to the finite grid size as well as the acceleration phase and thus it is apparently not possible to smooth the acceleration data by taking more data points.

Other Far-Field Radiation Prediction Schemes

It was felt necessary at this point to check the validity of the experimental data. Sound pressure levels were calculated at radial distances of 6.1 m, 12.2 m and 24.4 m and at 90° angular spacing (in the counterclockwise sense) from the center of the tank and at 0.91 m above the ground. The zero degree (0°) location was facing the side of the tank containing the main drain valve. The noise source is assumed to be the sum of several simple sources with the fact that the listener is affected only by the direct waves which illuminate the listener location. The acoustic pressure produced at the listener is the sum of the pressures that would be produced by an equivalent assembly of simple sources. The expression of the acoustic pressure at the listener is given by

$$p = \frac{\rho_o}{2\pi} \sum_{j=1}^{N} a_{n_j} \frac{e^{ikR_j}}{R_j} dS_{o_j} \qquad (7.10)$$

where

$$R_j = [R_c^2 + \xi_j^2]^{1/2} \tag{7.11}$$

is the distance from the area element on the tank wall to the listener (Fig. 7-4). For large distances from the source p to the listener Q as compared with the size of the area element, one may approximate R_j by

$$R_j = R_c + \frac{\xi_j^2}{2R_c} . \tag{7.12}$$

Since at large distances from the source, the amplitude of the pressure produced by any one of the surface elements differs very slightly from that of the other element, the distance R_j in the denominator of equation (7.10) can be approximated by using $R_j = R_c$. The relative phase of the pressures at the listener, by any two sources, depends on the difference in distance of the two elements and is practically independent of R_c. One can therefore replace R_j by $R_c + \frac{\xi_j^2}{2R_c}$ in the exponential in equation (7.10) to incorporate the phase effect. Finally, equation (7.10) can be expressed as

$$p = \frac{\rho_o}{2\pi R_c} \sum_{j=1}^{N} e^{ik\frac{\xi_j^2}{2R_c}} a_{n_j} \, dS_{o_j} . \tag{7.13}$$

The sound pressure level prediction as per this simple model has been found comparable with the measured sound level

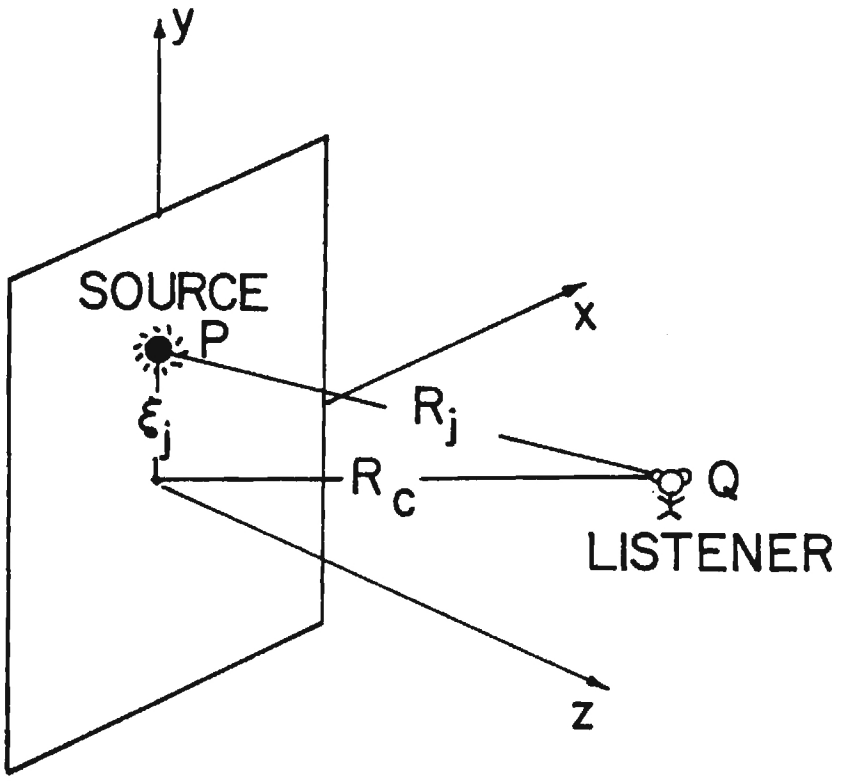

Figure 7-4. Coordinate System Used in Deriving the Radiation Pattern of a Rectangular Element

(see Table 7-3) except when the listener is facing the right of front side of the tank. The predicted sound pressure level for this case is very low than the measured value. This suggests that the direct wave contribution is even though important, but not quite enough by itself for the prediction scheme. It is possible that contributions from other sources which are not visible by the listener may be quite significant depending on the nature of surface vibration and source-listener configuration.

In the course of pursuing further with this critical evaluation of the prediction method, an analysis was made based on the uniform phase and relative phase source strength for the sources on the right of front side and the left of front side. The source strength for each face was computed as the sum of the source strengths due to individual simple sources. In fact, the ratio of the relative phase source strength $\left| \sum_{j=1}^{N} a_{n_j} dS_{o_j} \right|$ to the uniform phase source strength $\sum_{j=1}^{N} |a_{n_j}| dS_{o_j}$ is compared between the right of front side and the left of front side and the results are displayed in Table 7-4. One expects to find fair agreement between the results of the right of front side and the left of front side because the tank walls and the underwater speaker locations has been considered to be symmetric with respect to the center plane of the tank. However, the results in Table 7-4 indicate although the uniform phase source strength of the right of front side is comparable with that of the left of

Table 7-3. Measured and Predicted (Direct) Sound Pressure Level

Distance from the center of the tank in m		θ in degrees			
		0	90	180	270
6.1	Measured SPL	57.3	57.0	57.4	49.5
	Predicted SPL	57.8	31.7	54.8	51.7
12.2	Measured SPL	49.6	51.9	50.8	48.8
	Predicted SPL	52.1	19.8	48.7	48.7
24.4	Measured SPL	42.5	45.9	45.8	41.3
	Predicted SPL	44.6	20.3	42.6	43.4

Table 7-4. Ratio of Relative Phase Source Strength $\left| \sum_{j=1}^{N} a_{n_j} \, dS_{o_j} \right|$ to Uniform Phase Source Strength $\sum_{j=1}^{N} |a_{n_j}| \, dS_{o_j}$

	Right of Front Side (Side 2)	Left of Front Side (Side 4)
$\left| \sum_{j=1}^{N} a_{n_j} \, dS_{o_j} \right|$	0.0257	0.2786
$\sum_{j=1}^{N} |a_{n_j}| \, dS_{o_j}$	0.936	0.924
$\dfrac{\left| \sum_{j=1}^{N} a_{n_j} \, dS_{o_j} \right|}{\sum_{j=1}^{N} |a_{n_j}|}$	0.0274	0.301

front side, the relative phase source strength and hence their ratios do not agree with each other. The source strength ratio for the right of front side is about one-tenth than that of the left of front side. This indicates that the surface pressure at the right of front side is not primarily in phase with the surface normal velocity for that side. This results large cancellation in the Helmnoltz integral equation and hence large numerical errors in the far-field prediction.

Diffraction waves were considered next in the computation of the far-field sound prediction at certain ideal points. Unlike the theoretical analysis developed in Chapter II, on the approximation to the Green's function, any further analysis will not be provided because of the enormity of the presentations that would be required. Instead, attention will be given to some specific aspects (considering lowest order approximation to the Green's function) that may affect the sound levels. If the given source-listener configuration is such that,

(a) the sound is diffracted around more than one edge of the tank (listener is at region I, source is at side 3 in Fig. 7-5), (i.e., the listener cannot see any of the two vertical edges of the plane containing the source), the contribution to the pressure at the listener location is zero, i.e.,

$$G(\bar{r},\bar{r}_o) = 0 \qquad (7.14)$$

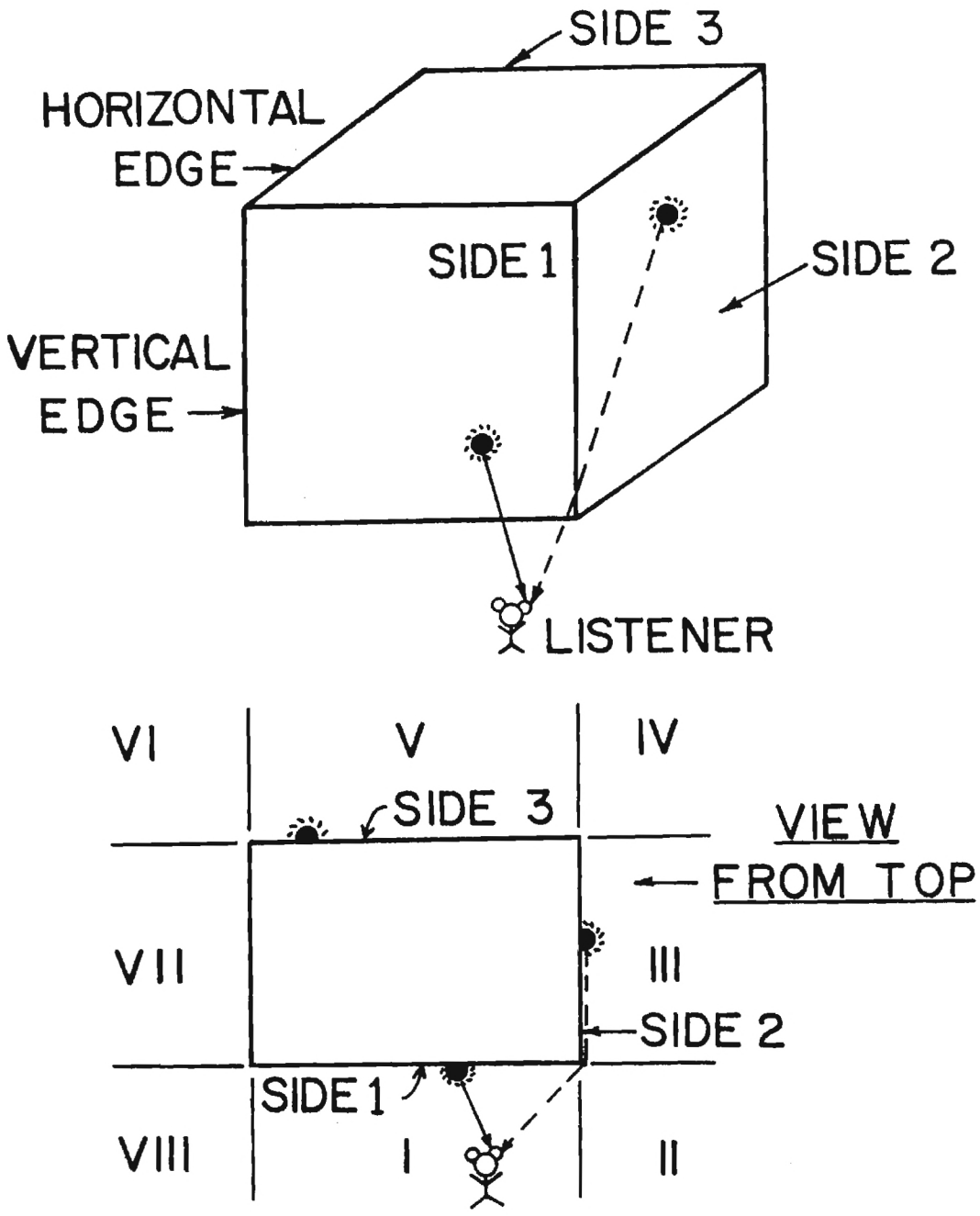

Figure 7-5. Schematic Diagram of Sources on the Rectangular Box and the Divided Region Outside the Right-Angled Box

(b) the listener can see (listener is at region I, source is at side 2 in Fig. 7-5) only one vertical edge of the plane containing the source, but not the other, the approximate Green's function can be expressed as

$$G(\bar{r},\bar{r}_o) = \frac{e^{ikL}}{L} \frac{e^{i\pi/4}}{\sqrt{2}} \frac{2}{\pi X} \tag{7.15}$$

(c) the listener can always see one vertical edge of the plane containing the source and perhaps also the other vertical edge (listener is at the boundary of region I and II, source is at side 2 in Fig. 7-5), i.e., the listener is in the extension of the plane containing the source, the approximate Green's function is

$$G(\bar{r},\bar{r}_o) = \frac{e^{ikL}}{L} \tag{7.16}$$

(d) the listener can see the source (listener is at region I, source is at side 1 in Fig. 7-5), only the direct wave contributions are included for the far field predictions. The approximate Green's function in this case is given by

$$G(\bar{r},\bar{r}_o) = \frac{2e^{ikR}}{R} \tag{7.17}$$

where R is the net distance from the source to the listener.

Given the source-listener configuration as in Fig. 7-6, the acoustic pressure at the listener is given by equation (4.1) as

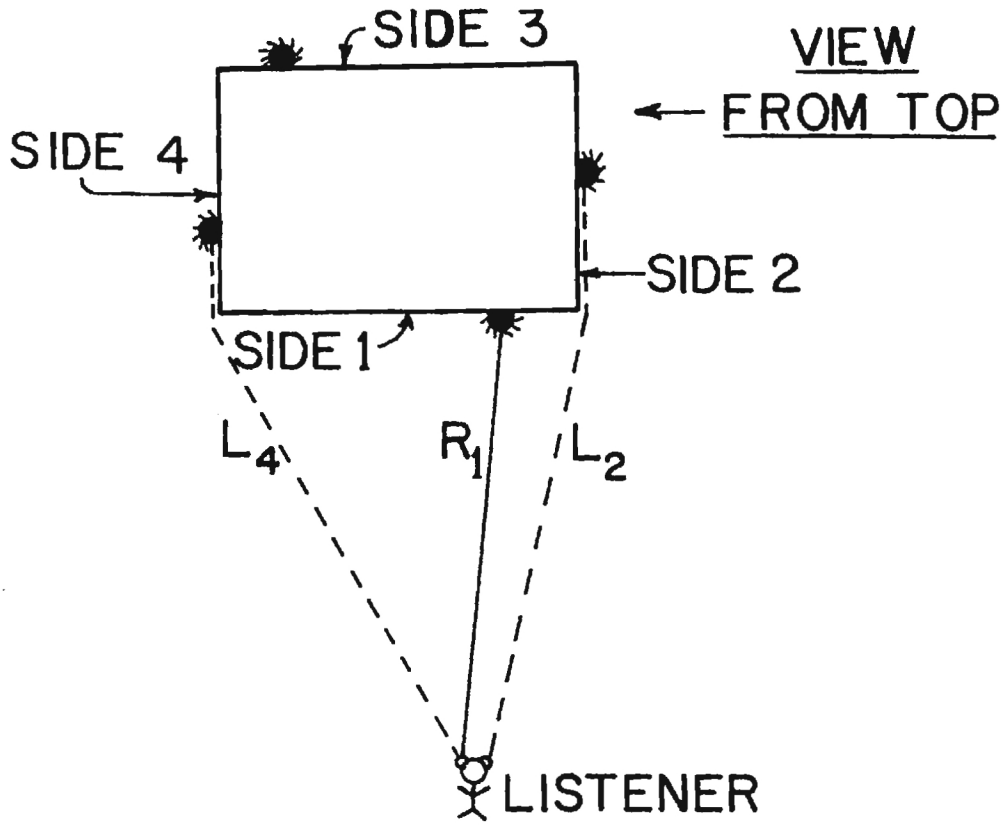

Figure 7-6. Schematic Diagram of Source-Listener-Right-Angled Wedge Configuration

$$p(\bar{r}) = \frac{\rho_o}{4\pi} \sum_{j=1}^{N} a_{n_j} \left(\sum_{\ell=1}^{M_j} G_{j\ell}(\bar{r},\bar{r}_o) \right) dS_{o_j} \qquad (7.18)$$

where $G_{j\ell}$ for the source in side 1 is $2\frac{e^{ikR_1}}{R_1}$, and for the sources at sides 2 and 4 is $\frac{e^{ikL_2}}{L_2}$ and $\frac{e^{ikL_4}}{L_4}$, respectively. The Green's function is zero, i.e., $G(\bar{r},\bar{r}_o) = 0$ when the source is on side 3. If the listener can see two sides of the box, (Fig. 7-7), the Green's function for the sources on these two sides are, respectively, $\frac{e^{ikR_1}}{R_1}$ and $\frac{e^{ikR_2}}{R_2}$. Green's function for the sources on the other sides can be considered to be negligible.

The sound pressure level thus obtained agrees closely with the measured sound pressure level (Table 7-5). These results may also be compared with that of the CHIEF prediction (Table 7-1) which are in general much higher than the measured sound pressure level. The fact that even the lowest order approximation to the Green's function compares reasonably well with the measured sound pressure level, indicates the justification of the application of the improved Green's function approximation as the transformer noise prediction scheme.

Effect of Finite Impedance of Ground

Finite acoustic impedance of ground [43,44], used in general to account for surfaces not necessarily rigid, is considered here to find the effect on the sound radiation

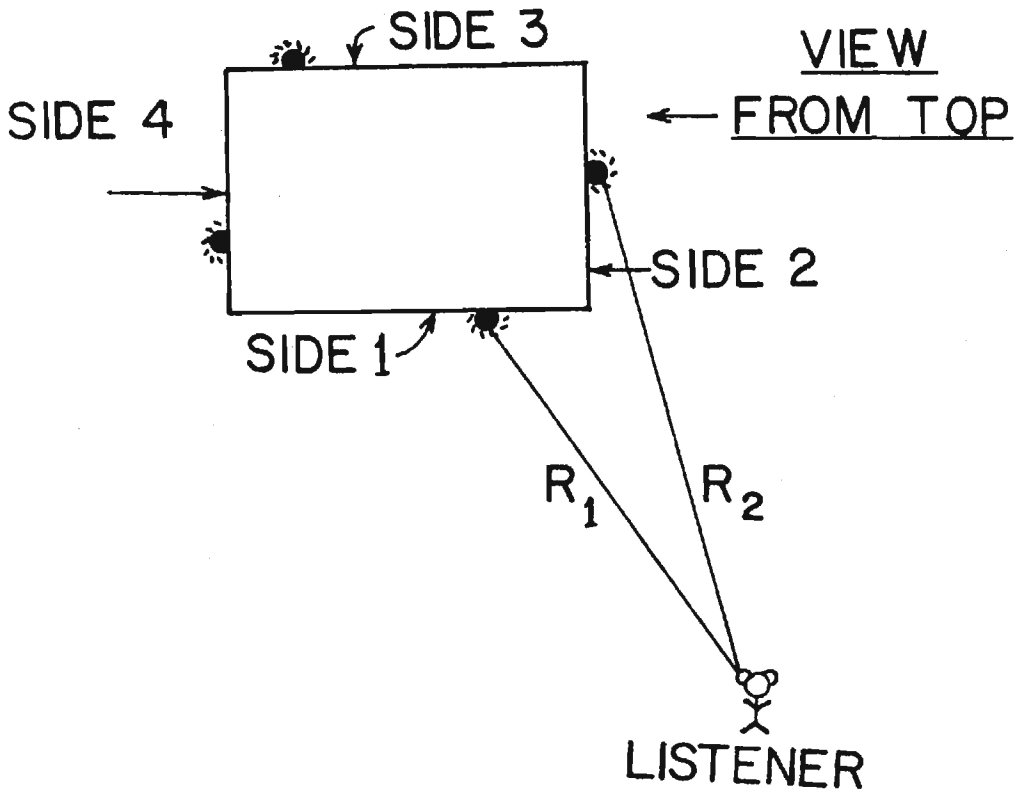

Figure 7-7. Schematic Diagram of Source-Listener-Right-Angled Wedge Configuration

Table 7-5. Measured and Predicted (Approximate Green's Function) Sound Pressure Level

Distance from the center of the tank in meters		θ in degrees							
		0	45	90	135	180	225	270	315
6.1	Measured SPL	57.3	53.3	57.0	56.6	57.4	49.9	49.5	51.0
	Approx. Green's fnc.	58.4	52.4	53.9	56.5	55.8	56.2	54.1	50.5
12.2	Measured SPL	49.6	47.1	51.9	50.8	50.8	45.8	48.8	48.9
	Approx. Green's fnc.	52.6	45.1	50.4	50.4	49.5	52.0	51.5	48.4
24.4	Measured SPL	42.5	42.7	45.9	45.0	45.8	36.2	41.3	45.1
	Approx. Green's fnc.	46.3	38.9	44.8	44.3	43.3	46.1	46.1	43.2

from a rectangular box-like structure resting on ground. The acoustic impedance which is expressed as the ratio of the pressure at the surface to the normal velocity of the surface depends on the nature of the surface material, on the frequency of the wave and its angle of incidence. In many cases, the various parts of the surfaces are not strongly coupled together and the motion normal to such a surface may be considered to be dependent only on the acoustic pressure incident on that portion. In this case, the motion of one part of the surface is independent of the motion of any other part and the surface is known as a locally reacting one. Although various theoretical models of sound propagation near the ground are available in the literature, the sound propagation over a grass covered hard ground can be adequately predicted by considering the ground as a locally reacting one [44,45]. This model will be used here to modify the direct as well as the diffracted wave contribution to the Green's function to predict the sound levels in the far field.

The finite acoustic impedance of ground, treated by introducing a plane wave pressure amplitude reflection coefficient R_p [34], is given by

$$R_p = \frac{\sin\psi - Z_1/Z_2}{\sin\psi + Z_1/Z_2} \tag{7.19}$$

such that the strength of the image sources are modified in order to modify all the possible waves which are reflected from the ground surface. Here ψ is the grazing angle (Fig. 7-8), Z_1 is the characteristic impedance of air given by $\rho_o c$, and Z_2 is the specific impedance of the ground surface.

The modified Green's function for the pressure amplitude at the listener Q due to a source at P can now be written as

$$G_{mod} = G(\bar{r}_a, \bar{r}_{o_a}) + R_p G(\bar{r}_i, \bar{r}_{o_i}) \tag{7.20}$$

where $G(\bar{r}_a, \bar{r}_{o_a})$ and $G(\bar{r}_i, \bar{r}_{o_i})$ represents contribution to the Green's function from the actual source and its image, respectively. The reflection coefficient R_p depends on the grazing angle of the direct and the diffracted waves coming from the image source. The direct wave contribution to the modified Green's function can be written as

$$G_{dir}|_{mod} = \left(\frac{e^{ikR_a}}{R_a} + R_{p_{dir}} \frac{e^{ikR_i}}{R_i} \right) \tag{7.21}$$

Here R_a represents the net distance from the original source to the listener while R_i represents the distance from the image source to the listener. The expression for the modified Green's function due to the waves diffracted by the edges is given by

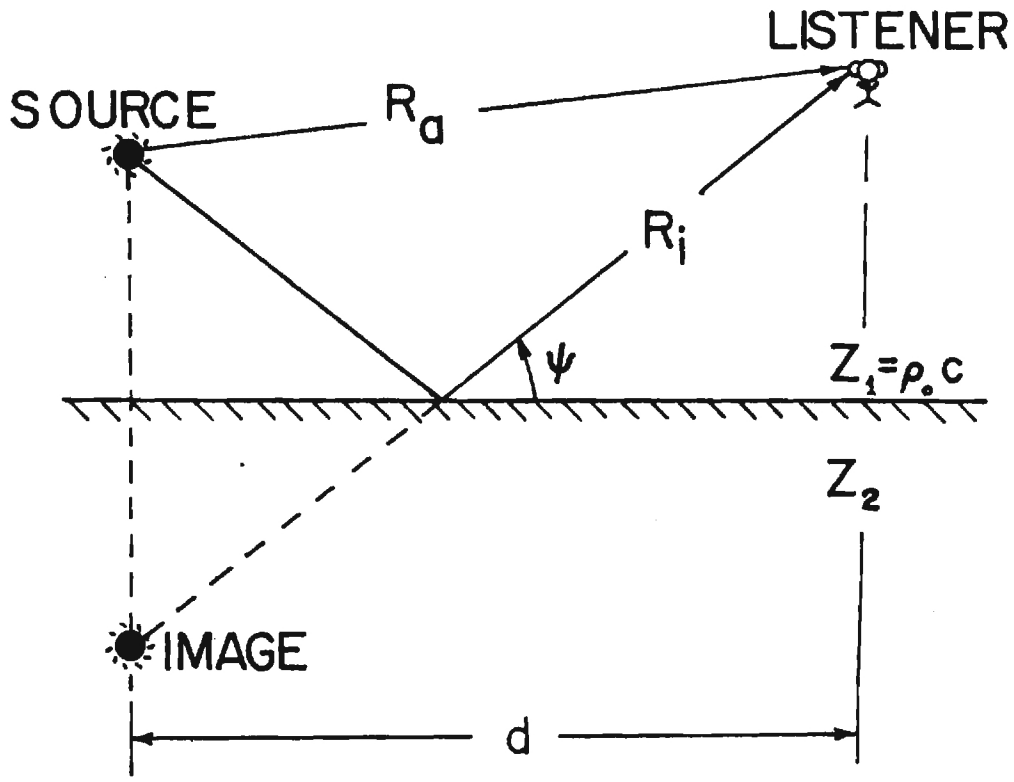

Figure 7-8. Sketch of Reflection of Sound Wave from Flat Ground with Impedance Z_2

$$G_{diffr}\Big|_{mod} = \frac{e^{i\pi/4}}{\sqrt{2}} \left[\frac{e^{ikL_a}}{L_a} \left\{ A_D(X_{+a}) + A_D(X_{-a}) \right\} \right.$$

$$\left. + R_{p_{diffr}} \frac{e^{ikL_i}}{L_i} \left\{ A_D(X_{+i}) + A_D(X_{-i}) \right\} \right] \quad (7.22)$$

where the subscript "a" refers to the actual source and the subscript "i" refers to the image source. Therefore, the consideration of the finite acoustic impedance of the ground surface modifies the sound pressure level as

$$L_p\Big|_{mod} = 10 \log_{10} \frac{\langle p^2_{mod}(\bar{r}) \rangle}{(p^2_{ref})} \quad (7.23)$$

where

$$p_{mod}(\bar{r}) = \frac{\rho_o}{4\pi} \left[\iint_{S_{o_a}} \left\{ G_{mod}(\bar{r}_a, \bar{r}_{o_a}) a_n(\bar{r}_{o_a}) \right\} dS_{o_a} \right.$$

$$\left. + \iint_{S_{o_i}} \left\{ G_{mod}(\bar{r}_i, \bar{r}_{o_i}) a_n(\bar{r}_{o_i}) \right\} dS_{o_i} \right] \quad (7.24)$$

and

$$G_{mod} = G_{dir}\Big|_{mod} + G_{diffr}\Big|_{mod} . \quad (7.25)$$

This leads to an expression for the difference of the modified sound pressure level and the sound pressure level with the rigid plane assumption as

$$L_p\Big|_{mod} - L_p = \frac{|p_{mod}|^2}{|p|^2} = \frac{\left(\sum_a \sum_i G(r_a, r_{o_a}) a_n(r_{o_a}) ds_{o_a}\right)^2}{\left(\sum_i G(\bar{r}, \bar{r}_{o_i}) a_n(\bar{r}_{o_i}) ds_{o_i}\right)^2}. \qquad (7.26)$$

For some grazing angle ψ, the term $\sin\psi$ in equation (7.19) may be so small compared to the fixed parameter Z_1/Z_2 that the reflection coefficient R_p is effectively equal to -1. This signifies a cancellation of incident and reflected waves near grazing incidence and hence the propagation of plane wave is not applicable any more. A ground wave term, the effect of which decreases with the increase of grazing incidence, is usually included in equation (7.20) in addition to the existing terms to incorporate the effect of small grazing angles [44,45]. This is needed to match the boundary condition, in particular, the variation of the curvature of the wavefronts with distance along the boundary.

The comparison of the effect of finite impedance of ground for a given source-listener location (Fig. 7-9) is illustrated in Fig. 7-10. A point source, excited at a pure-tone frequency of 265 Hz, is located on the upper right section of the front side (0.16 m to the left of the right hand vertical edge and 1.10 m above the ground) of a 1.3 m

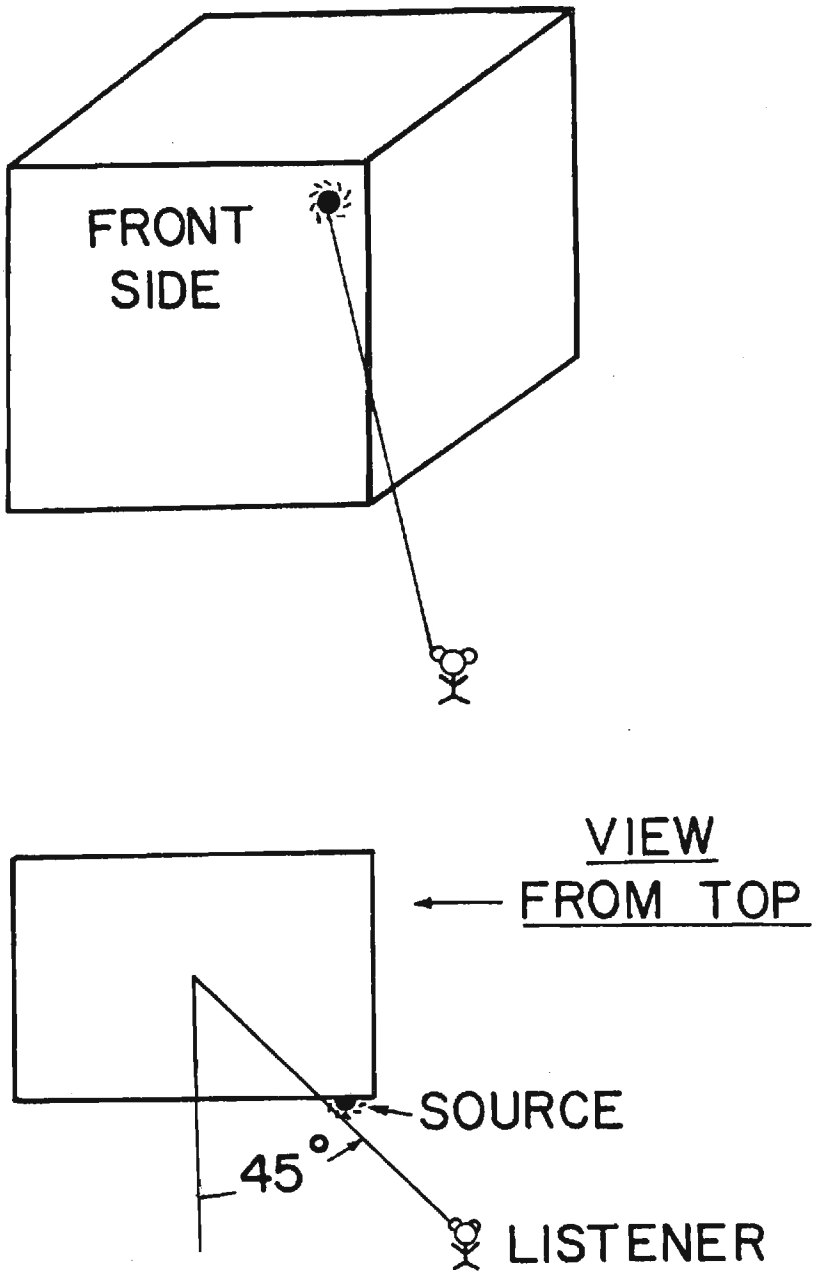

Figure 7-9. Sketch of Source-Listener-Edge Configuration

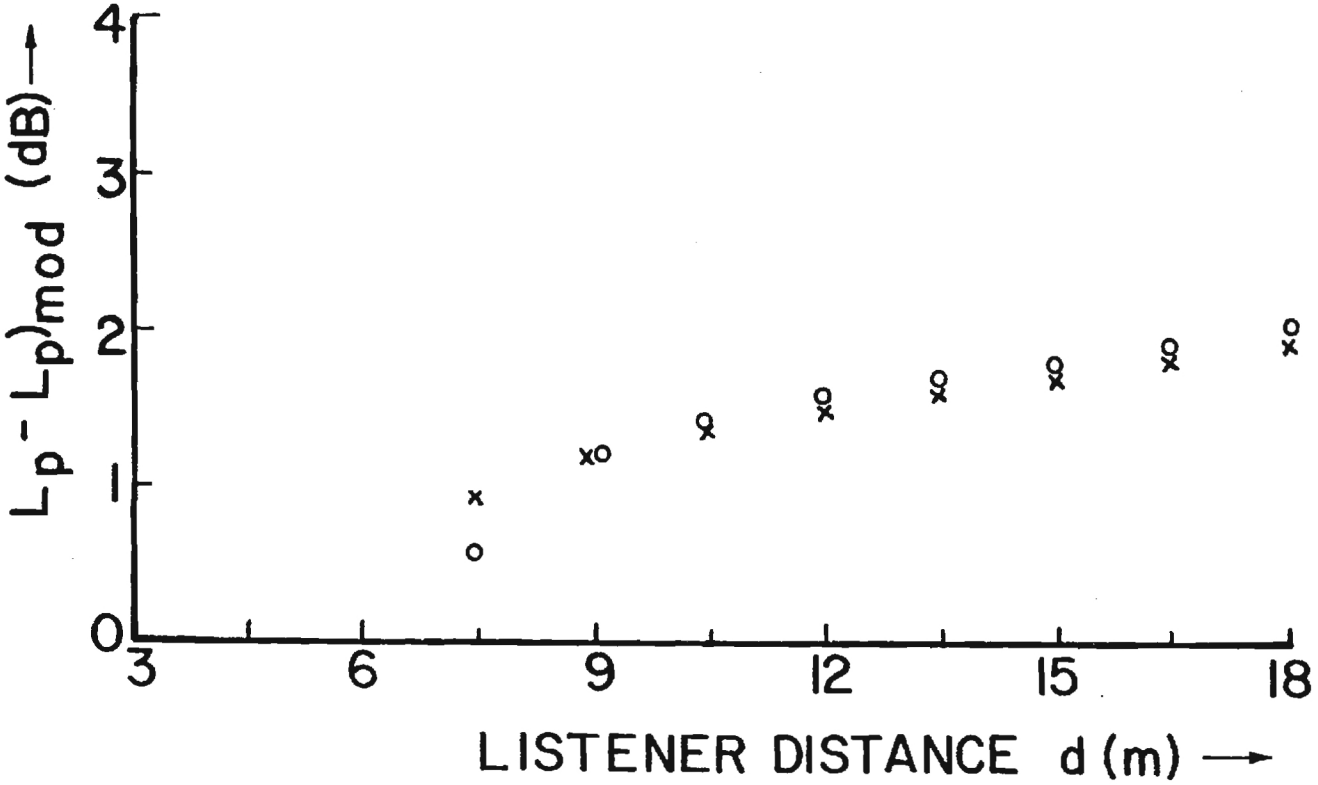

Figure 7-10. Effect of Finite Impedance of Ground on Listener Distance and Height
x 0.91 m above the Ground
o 1.22 m above the Ground

by 0.76 m by 1.52 m size parallelopiped standing on the grass covered ground. The listener is facing the source at an angle of 45° with a vertical plane passing through the center of the tank and normal to the side containing the source (Fig. 7-9). The value of the specific acoustic impedance of ground which is 12.5 + i 14.3 at 265 Hz frequency is obtained from a paper by Embleton et al. [44]. One direct wave as well as four diffracted waves (two from vertical edges and two from horizontal edges) contribute to the sound pressure level received by the listener. The variations of the sound pressure level with the rigid plane assumption and the modified sound pressure level, given by equation (7.26), is plotted in Fig. 7-10 as a function of the distance from the source to the listener and for two different listener heights—one at 0.91 m above the ground (denoted by X in Fig. 7-10) and the other at 1.22 m above the ground (denoted by o in Fig. 7-10).

Effect of Double Edge Diffraction

Diffraction is usually attributed to the fact that the wavelength is not zero. The accuracy of the geometrical theory of diffraction increases as the wavelength becomes much smaller than the obstacle. The application of the geometrical theory of diffraction gives quite accurate results even for wavelengths comparable to or higher than the obstacle size provided proper terms are included. The Fresnel function argument Y, in equation (3.35), which increases with the

decrease in wavelength can, at points, become adequate enough to predict the far field sound levels within reasonable accuracy even without considering double-edge diffraction contributions.

The limit on the wavelength which can be readily determined from equation (3.25) in order to neglect the Green's function contribution for the single-edge diffraction compared to the direct wave can also be shown to be applicable to the case of double-edge diffraction compared to the single-edge diffraction simply by replacing r_o by r_s. This is based on the fact that the Green's function contribution from the singly diffracted wave is of minor importance (within ±.5 dB) compared to the direct wave for the argument of the Fresnel functions being greater than 2, i.e.,

$$|X(\theta)| > 2.$$

The requirement for $|X(\theta)|$ to be greater than 2 is

$$\frac{r_s}{\lambda} > \left(\frac{4}{3\sqrt{6}}\right)^2,$$

i.e.,

$$\lambda < r_s \left(\frac{3\sqrt{6}}{4}\right)^2$$

where r_o in equation (3.25) has been replaced by r_s. For such values of λ, the double edge diffraction is negligible compared to the single-edge diffraction. It is to be noted

that the doubly diffracted rays can also be neglected compared to the singly diffracted rays if r_s is large enough to satisfy the above criterion for a given λ.

At higher wavelengths, i.e., at low frequencies, the effect of multi-edge diffraction may be meaningful at certain listener positions depending on the location of the source and the geometrical configuration of the vibrating structure. In typical applications of sound diffraction, one may generally expect that the double edge diffraction is significant only near the boundaries operating the illuminated and the shadow regions. This is justifiable from the fact that the omission of double and multi-edge diffraction contributions in the numerical calculations give rise to small but noticeable discontinuities in the Green's function at the edge of the shadow zone. Further significance of the effect of double-edge diffraction can be made clear through an example.

A rectangular thin box-like structure (0.62 m x 0.14 m x 0.15 m), shown in Fig. 5-5, has been considered for this illustration. The front surface of this structure is divided into several elements. Each of these elements is assumed to vibrate uniformly in phase with unit acceleration at first at a pure tone frequency of 250 Hz and then at 2500 Hz. That the discontinuities at the boundaries separating the shadow zones from the illuminated zones at low frequency are due to the omission of the multi-edge diffraction terms are distinct from Fig. 7-11. The consideration of the double-edge

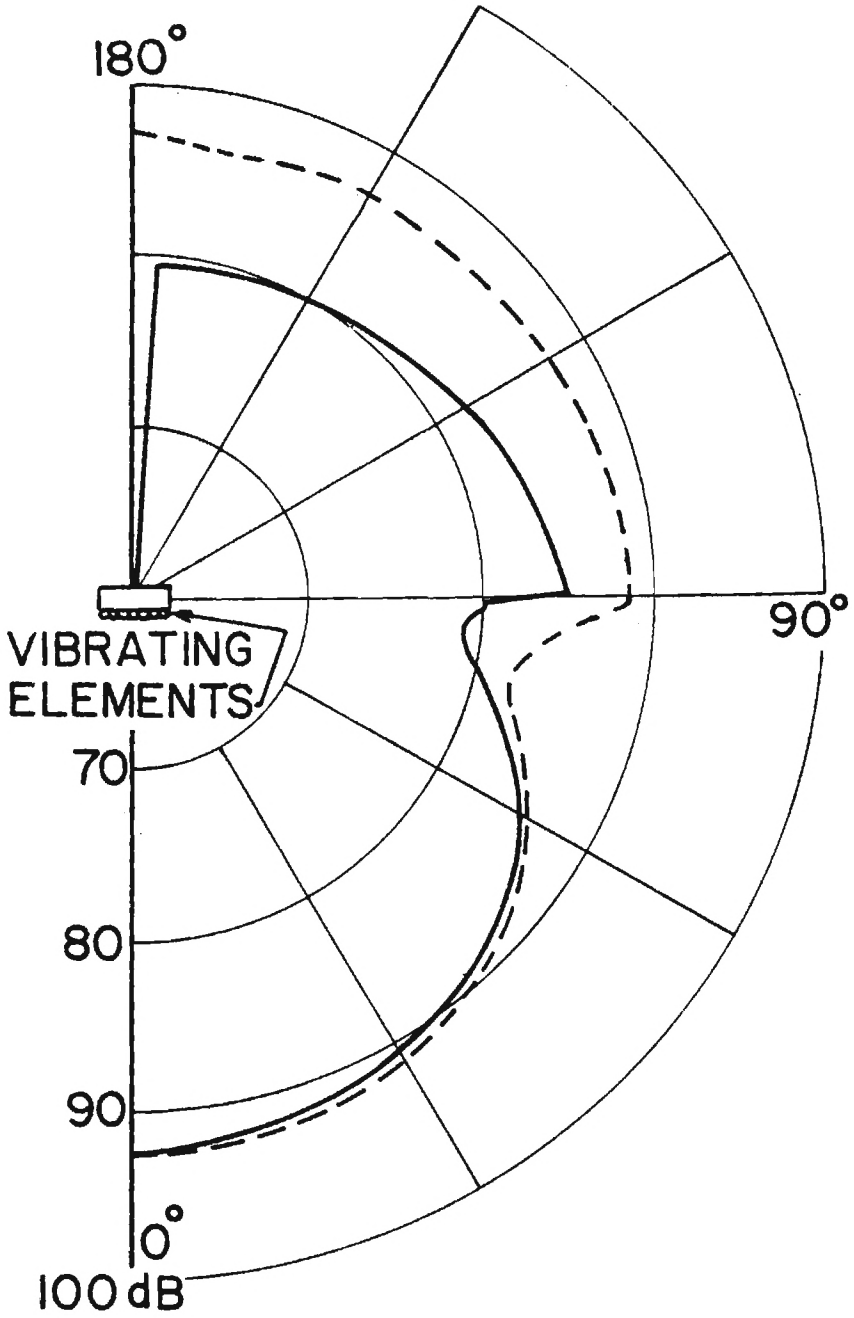

Figure 7-11. Comparison of the Effect of Single and Double-Edge Diffraction. Frequency 250 Hz; 5.5 m from the Center of the Array of Vibrating Elements

diffraction terms give a smooth curve in the transition region where the shadow zone separates from the illuminated zone. It is to be noted that the omission of the double-edge diffraction terms in this case result in zero sound level just behind the box-like structure. Figure 7-12 describes the sound pressure levels for 2500 Hz vibrational frequency. The double-edge diffraction contribution to the Green's function is negligible here (Fig. 7-12) (as the wavelength is much smaller than the obstacle) except at the shadow zone. One may also note that there is no discontinuous behavior of the curve when only the single-edge diffraction is considered.

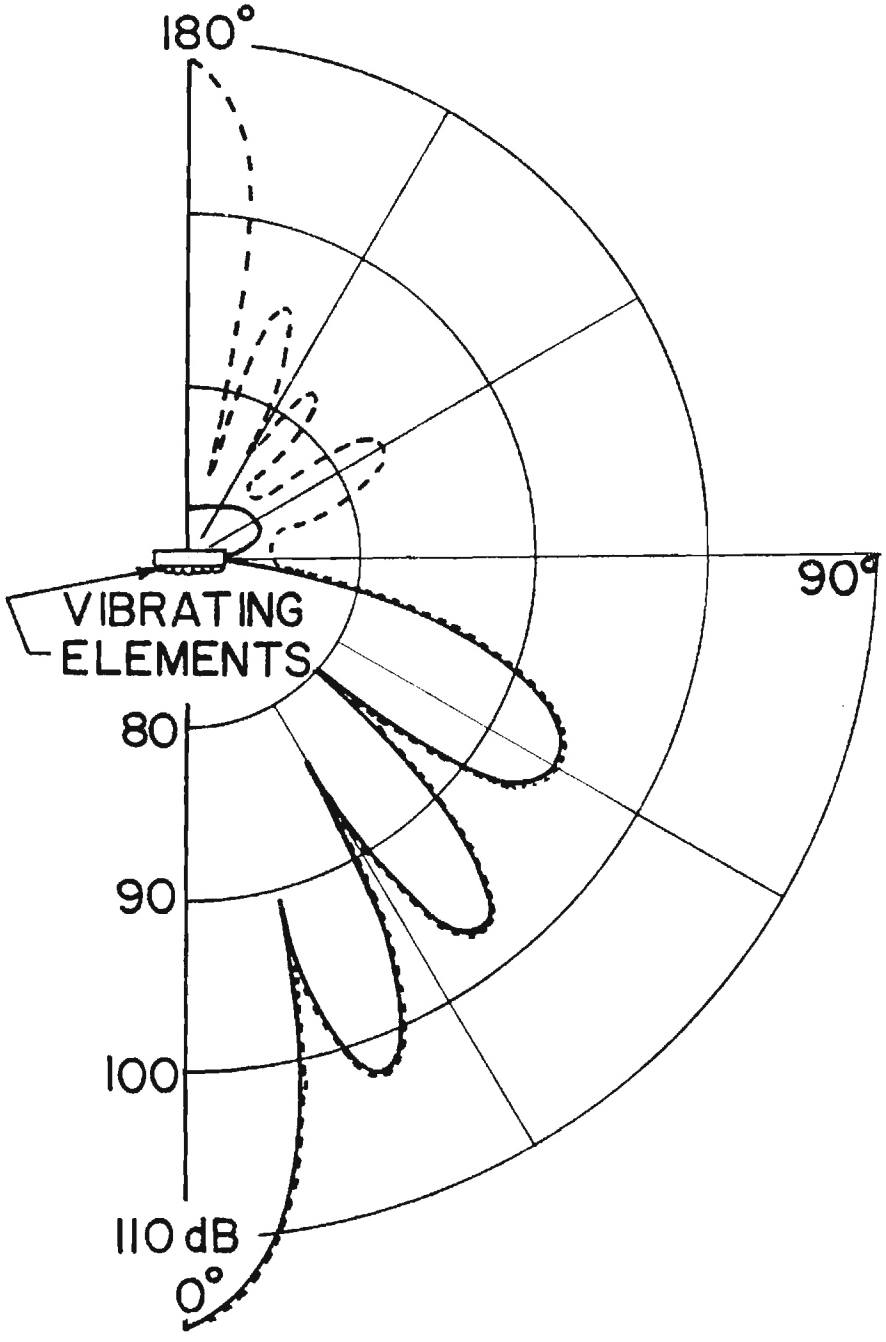

Figure 7-12. Comparison of the Effect of Single and Double-Edge Diffraction. Frequency 2500 Hz; 5.5 m from the Center of the Array of Vibrating Elements.

CHAPTER VIII

CONCLUDING REMARKS

A far-field prediction scheme of sound radiated by typical electric transformers has been described in the dissertation. The transformer is considered as a smooth rectangular box-like structure and the ground on which the transformer rests is idealized as a perfectly rigid plane. An adequate approximation to the Green's function has been fabricated for the entire far-field predictions by using techniques related to the geometrical theory of diffraction. The diffracted waves are derived from the uniformly valid asymptotic expressions for diffraction of point source generated waves by a semi-infinite right-angled rigid wedge. Several applications of this technique which is well suited for numerical computations has been discussed. The far-field predictions thus obtained may be used to estimate the directional variation of the A-weighted sound level which is often a measure in annoyance ratings.

Although the analysis of sound propagation is based on the assumption of perfect rigidity of the ground, in the actual case, irrespective of how hard the ground is, it has some finite acoustic impedance. This gives rise to the finite probability of partial sound reflection from the ground. Also, emphasis has been given mainly on the single edge

diffraction and not much on double-edge diffraction except while comparing the present theoretical analysis with some available experimental data. These facts do not nullify the justification of the broad range applicability of the present analysis but perhaps need some judgement in the interpolation of any quantitative prediction. In particular, it is not difficult to incorporate the effects of either the acoustic impedance of ground, the double-edge diffraction or even the absorbing or partial transmission properties of the vibrating surfaces except the complexity of bookkeeping in the numerical calculations. Considerations of the effects of finite impedance of ground and double-edge diffraction should nonetheless enable one to determine the limits on the sound levels recorded at various listener locations for given source positions and geometry of the vibrating structure.

The idealization that the propagating medium be homogenous and quiescent may not be realistic and so the sound propagation will be effected by surface meterology and topography. The variation of temperature and average speed of wind with height over a large flat area and the associated turbulence may refract sound which is not accounted in the above technique. Thus there may be significant variation of sound pressure level between the measured values and the estimates based on the above scheme.

There are several extensions of the work described here that may be carried out. One important extension would

be to include the effects of cooling fans and to develop techniques for predicting noise levels at multiple transformer sites. Another extension would be to include the effects of barriers, near by buildings and terrain irregularities in the far-field prediction scheme.

Other work which can be contemplated is the development of scaled down modeling to predict noise levels near substations. It may be possible for example to develop sound sources of smaller dimensions which have essentially the same directivity at a correspondingly scaled-up frequency as do actual transformers. If so, perhaps one can make scaled down models of substations, surrounding buildings and terrain and use these in predicting noise levels for future installations. Acoustic modeling of outdoor sound propagation being a standard tool in transportation system planning at present, one has some confidence that it may eventually prove useful in transformer substation or power generator site planning.